

# Morphology and Mechanical Properties of Electrospun Polymeric Fibers and Their Nonwoven Fabrics

by Chia-Ling Pai

Bachelor of Science and Master of Science in Chemical Engineering  
National Taiwan University, Taipei, Taiwan  
(June 2003 and June 2005)

SUBMITTED TO THE DEPARTMENT OF CHEMICAL ENGINEERING IN  
PARTIAL FULFILLMENT OF THE REQUIREMENTS FOR THE DEGREE OF

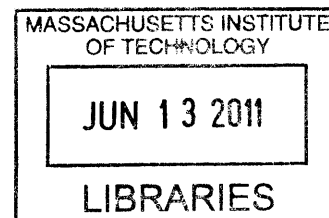
DOCTOR OF PHILOSOPHY IN CHEMICAL ENGINEERING

AT THE

MASSACHUSETTS INSTITUTE OF TECHNOLOGY  
(May 2011)

[June 2011]

© Massachusetts Institute of Technology, 2011. All rights reserved.



**ARCHIVES**

Signature of Author: \_\_\_\_\_

Chia-Ling Pai  
Department of Chemical Engineering  
May 2011

Certified by: \_\_\_\_\_

Gregory C. Rutledge  
Lamot du Pont Professor of Chemical Engineering  
Thesis Advisor

Certified by: \_\_\_\_\_

Mary C. Boyce  
Gail E. Kendall Professor of Mechanical Engineering  
Thesis Advisor

Accepted by: \_\_\_\_\_

William M. Deen  
Carbon P. Dubbs Professor of Chemical Engineering  
Chairman, Committee for Graduate Students

# **Morphology and Mechanical Properties of Electrospun Polymeric Fibers and Their Nonwoven Fabrics**

by

Chia-Ling Pai

Submitted to the Department of Chemical Engineering on April 29, 2011  
in partial fulfillment of the requirements for the degree of  
Doctor of Philosophy in Chemical Engineering

## **Abstract**

Electrospinning is a straight forward method to produce fibers with diameter on the order of a few tens of nanometers to the size approaching commercial fibers (on the order of 10  $\mu\text{m}$  or larger). Recently, the length scale effect on physical properties has attracted great attention because of the potential to produce new materials with unique behavior. In general, the behavior of commercial fibers can be investigated by traditional experiments, and that of nanofibers can be studied by molecular dynamics simulation or Monte Carlo technique. However, the transition of their properties from the bulk to the nanoscale materials is not well understood. Electrospinning provides us a bridge to understand the properties of fibers transiting from the behavior of the bulk material to that of the nanofibers. Among these areas, I am interested in the possible remarkable changes in mechanical properties that may occur in electrospun fibers due to the size effect, where the comprehensive understanding is still lacking. My research objectives are to understand mechanical properties of electrospun polymeric fibers as a function of their size, structure and morphology.

The first part of my research is to study internal structures and external topographies of electrospun fibers, and to understand their effect on mechanical properties. Amorphous polystyrene (PS) and semicrystalline polyacrylonitrile (PAN) were dissolved in a high boiling point solvent, dimethylformamide (DMF), for electrospinning. When electrospun in a high-humidity environment, the interior of these fibers was found to be highly porous rather than consolidated, despite the smooth and nonporous appearance of the fiber surfaces. The formation of interior porosity is attributed to the miscibility of water, a nonsolvent for the polymers in solution, with DMF. The resulting morphology is a consequence of the relatively rapid diffusion of water into the jet, leading to a liquid-liquid phase separation that precedes solidification due to evaporation of DMF from the jet. When electrospun in a low humidity environment, the fibers exhibit a wrinkled morphology that can be explained by a buckling instability. Understanding which structures and morphology form under a given set of conditions is achieved through the comparison of three characteristic times: the drying time, the buckling time and the phase separation time. The structures and morphology have important

consequences for the properties of the fibers such as their mechanical strength and stiffness.

Secondly, we studied the size effects of single electrospun fibers on their stiffness and strength. The Young's modulus and yield strength of individual electrospun fibers of amorphous poly(trimethyl hexamethylene terephthalamide) (PA 6(3)T) have been obtained in uniaxial extension. The Young's modulus is found to exhibit values in excess of the isotropic bulk value, and to increase with decreasing fiber diameter for fibers with diameter less than roughly 500 nm. The yield stress is also found to increase with decreasing fiber diameter. These trends are shown to correlate with increasing molecular level orientation within the fibers with decreasing fiber diameter. Using Ward's aggregate model, the correlation between molecular orientation and fiber modulus can be explained, and reasonable determinations of the elastic constants of the molecular unit are obtained.

Finally, we identified a relation of stiffness between single electrospun fibers and their nonwoven fabrics. This is of interest because adequate mechanical integrity of nonwoven fabrics is generally a prerequisite for their practical usage. The Young's modulus of electrospun PA 6(3)T nonwoven fabrics were investigated as a function of the diameter of fibers that constitute the fabric. Two quantitative microstructure-based models that relate the Young's modulus of these fabrics to that of the fibers are considered, one assuming straight fibers and the other allowing for sinuous fibers. This study is particularly important for meshes comprising fibers because of our recent discovery of an enhanced size effect on their Young's modulus as well as the tendency towards a curved fiber topology between fiber junctions. The governing factors that affect the mechanical properties of nonwoven mats are the fiber network, fiber curvature, intrinsic fiber properties, and fiber-fiber junctions. Especially for small fibers, both the intrinsic fiber properties and fiber curvature dominate the mechanical behavior of their nonwoven fabrics.

This thesis helps us to understand the mechanism behind the enhanced mechanical behavior of small fibers, and to identify determining parameters that can be used to tailor their mechanical performance.

Thesis Supervisor: Gregory C. Rutledge

Title: Lamot du Pont Professor of Chemical Engineering

Thesis Supervisor: Mary C. Boyce

Title: Gail E. Kendall Professor of Mechanical Engineering

## **Acknowledgements**

Studying abroad is an adventure, especially when the talent of language learning is not in my genes. However, the opportunity to expose myself, a person raised in the countryside in Taiwan, to the global experience and vision broadening overbears the obstacle of using English as a second language. If I can trace back and plot my feeling towards the almost six years of my prime time (according to the dramatic decrease of my collagen levels) in the Ph.D. study, it will look like the stock chart in the late century, full of unexpected bull and bear periods, but luckily the overall trend is up.

I learned a lot these years at MIT and become a better scientist/engineer, which leads me to be truly thankful to my advisors, Prof. Rutledge and Prof. Boyce, who both have a charming smile and are supportive. Prof. Rutledge is always there when I need his guidance in research. He is the one I found who devoted himself the most to enjoying the research with enthusiasm. Prof. Boyce is very creative and looks at the world from a fascinating angle. She can turn something disappointing into something novel and interesting. My thesis work would not have been possible without their insightful advice and encouragement through my entire study. I would like to express my gratitude to my thesis committee members, Prof. Gleason and Prof. Van Vliet, who provided me with additional useful viewpoints and made me aware of some key issues in my projects. I also thank Iris Chang, Marlisha McDaniels, Alina Haverty, Katie Lewis, Linda Mousseau, Gwen Wilcox, and Tony Pulsone for being the bridge to coordinate things among the department, professors, and me.

Jian Yu is the person who helped me the most and taught me many things about electrospinning at the beginning of my research when I first joined the group. He is nice and generous to share his knowledge with me. Also, I would like to thank Joe Lowery, Minglin Ma, Pradipto Bhattacharjee, Liang Chen, Matthew Mannarino, Yuxi Zhang, and Simon Choong in Rutledge group for the discussion of general electrospinning issues; Peng Yi and Sezen Buell for their attitude towards Ph.D. life; Steven Kooi, Cheng-Yen Wen, Yeo-Wan Chiang, and William DiNatale for their assistance in the experiments at Institute for Soldier Nanotechnologies (ISN); and

Lifeng Wang and Meredith Silberstein in the Boyce group for their expertise in the construction of micromechanical models. It is hard to list everyone who has ever helped me in every aspect in this acknowledgements. For all of this, I would like to give special thanks to members of Rutledge group and Boyce group, who accompanied me through these years.

I am lucky to have met many great people here. Thanks to Long-Hua Lee, Ling Chao, Hsien-Chung, Kay, Jen, Chih-Jen and Michelle, and Po-Yen for uniting a warm Taiwanese group in Chemical Engineering; 9Bmers (Chin-Wu, Yang, and Taiwei), Chao-Chi, Chia-Wei, Cheng-Wei, and Shih Wei for exploring the world together when I first arrived in Boston; I-Fan and Mohan, Aone and Shwu Jen, Lisa, Mike and Yuko, Chih-Chao, Chiao, Carl, and Claire for the meaningful and inspiring conversation we had in the salon and parties; Wei-Chuan, Vivian, Chia-Ying, and Andrew for the fun time in ROCSA. Special thanks to Stella, Chien-Cheng, Huang-Wei, and Moment for being lifelong friends; Chia-lin for introducing me many delicious food, Joe and Linda for helping me grow up as a person; Michael, Hank, and Ellen for adding light to my critical time and pouring joy into the perplexing period of my life, and especially thanks to Tsung-Yao for the effort on inducing my spirit of competition to finish the thesis on time.

Last but not least, I thank my family for their support during my endless pursuit of knowledge. They give me selfless love and care in my life, and support the choices I have made. Every year after I visit home, I feel energetic again because of my wellness circle. My departed grandfather always told me to go as far as I could in the learning road of knowledge pursuit. This thesis is dedicated to my lovely family overseas in Taiwan – my Mom, Dad, and Brothers. I hope my departed grandfather and grandmother can be proud of me.

## Table of Contents

<b>Abstract</b> .....	1
<b>Acknowledgements</b> .....	3
<b>Table of Contents</b> .....	5
<b>List of Figures</b> .....	7
<b>List of Tables</b> .....	10
<b>Chapter 1 Introduction</b> .....	11
1.1 Motivation.....	11
1.2 Background.....	12
1.2.1 Electrospinning.....	12
1.2.2 Applications.....	14
1.3 Thesis Overview.....	14
1.4 References.....	16
<b>Chapter 2 Experimental Methods</b> .....	17
2.1 Materials .....	17
2.2 Sample Preparation.....	17
2.3 Characterization.....	19
2.3.1 Morphological and Structural Characterization.....	19
2.3.2 Mechanical Characterization.....	22
2.3.3 Thermal Characterization.....	24
2.3.4 Characterization for Phase Separation.....	25
2.3.5 Mat Properties.....	25
2.3.6 Computational Aid.....	25
2.4 References.....	27
<b>Chapter 3 Morphology of Porous and Wrinkled Electrospun Fibers</b> .....	29
3.1 Introduction.....	29
3.2 Results and Discussion.....	30
3.2.1 Observations of Exterior Fiber Structure Before and After Annealing...	30
3.2.2 Mechanical Property Evaluation.....	33
3.2.3 Observation of Interior Fiber Structure.....	34
3.2.4 Rationalization of Interior and Exterior Structure in terms of Models...	35
3.2.5 Fiber Morphology Evolution.....	43
3.2.6 Other Polymer System: PAN/DMF.....	48
3.2.7 Explanation of Mechanical Behavior of Fibers with Voids.....	52
3.3 Concluding Remarks.....	57
3.4 References.....	58
<b>Chapter 4 Wrinkled Topographies of Electrospun Fibers</b> .....	63
4.1 Introduction.....	63
4.2 Results and Discussion.....	63
4.2.1 Experimental Observation of Wrinkled Topographies.....	63
4.2.2 Mechanism of Wrinkle Fibers.....	65

4.2.3 Analytical Solution for Critical Wave Number and Wavelength.....	66
4.2.4 Finite Element Analysis for Critical Wave Number and Wavelength.	68
4.2.5 Rationalization of Experimental Results.....	71
4.3 Concluding Remarks.....	72
4.4 References.....	72
<b>Chapter 5 Mechanical Properties of Individual Electrospun Polymer Fibers and Their Variation with Fiber Diameter.....</b>	<b>74</b>
5.1 Introduction.....	74
5.2 Different Techniques for Mechanical Measurement of Single Fibers.....	75
5.3 Results and Discussion.....	82
5.4 Concluding Remarks.....	91
5.5 References.....	92
<b>Chapter 6 Microstructural Modeling of the Elastic Modulus of Electrospun Nonwoven Fiber Meshes.....</b>	<b>96</b>
6.1 Introduction.....	96
6.2 Theoretical Section.....	97
6.2.1. Nonwoven Fabric Model for Straight Fibers.....	97
6.2.2. Nonwoven Fabric Model for Sinuous Fibers.....	101
6.3 Results and Discussion.....	103
6.4 Concluding Remarks.....	109
6.5 References.....	110
<b>Chapter 7 Conclusions and Recommendation.....</b>	<b>112</b>
7.1 Conclusions.....	112
7.2 Recommendation for Future Work.....	113
7.2.1 Porous Fibers.....	113
7.2.2 Wrinkled Fibers.....	114
7.2.3 Nanofibers.....	114
<b>Appendix I Modified Equations for Mercury Porosimetry.....</b>	<b>116</b>
<b>Appendix II Matlab Codes for Spinodal and Binodal Curves of Ternary Phase Separation.....</b>	<b>118</b>
<b>Appendix III Matlab Codes for Mass Transfer Paths.....</b>	<b>121</b>
<b>Appendix IV Matlab Codes for the Calculation of Orientation and Curvature Distribution of Nonwoven Fabrics Using Image Analysis.....</b>	<b>125</b>
<b>Appendix V Determination of Diffusion and Mass Transfer Coefficients.....</b>	<b>128</b>

## List of Figures

Figure 1-1	Electrospinning setup (modified from [1] and courtesy of Rutledge group.....	13
Figure 1-2	Possible structures and morphology of electrospun fibers.....	13
Figure 1-3	Overview of objectives.....	15
Figure 2-1	The illustration of molecular orientation of PA 6(3)T.....	21
Figure 2-2	The nonwoven fabric tested by a Zwick mechanical tester with marked dots on it. (a) before deformation, and (b) after deformation. The insert images are SEM images of nonwoven fabrics.....	23
Figure 2-3	Tensile test configuration: (a) the paper template (shown in gray) for gripping the fiber with fiber spanning the cut-out region, and (b) the setup for tensile testing of a single fiber with the paper template (shown in white) secured in test position and then cut, readying the fiber for testing. Note that the fiber diameter is artificially enlarged in the images in order to be seen.....	24
Figure 2-4	Coplan's construction for the determination of yield point [10].....	24
Figure 3-1	SEM images of fibers electrospun from a 30 wt% PS/DMF solution at 29% relative humidity: (a) as-spun fibers and (b) annealed fibers (scale bar: 5 $\mu\text{m}$ ).....	31
Figure 3-2	SEM images of (a) as-spun fibers and (b) annealed fibers electrospun from a 30 wt% PS/DMF solution under different relative humidity. The insert images are cross-sectional TEM images.....	32
Figure 3-3	Engineering stress-strain curves for single fibers electrospun from a 30 wt% PS/DMF solution at 29% relative humidity. Each datum is averaged over 15 fibers, and error bars correspond to one standard deviation.....	34
Figure 3-4	(a) The cross-sectional TEM image of as-spun fibers electrospun from a 30 wt% PS/DMF solution at 29% relative humidity and (b) those fibers followed by annealing at 65°C under vacuum for a day (scale bar: 500 nm).....	35
Figure 3-5	(a) Ternary phase diagram for the three component system, and (b) the enlarged version of red window in (a). Experimental data: (red star symbol: before observed cloud point, and blue star symbol: after observed cloud point). Theoretical binodal (solid gray curve) and spinodal (dotted curve). Theoretical mass transfer paths for 30 wt% PS/DMF solutions ( $\blacksquare$ : 10%, $\bullet$ : 20%, $\blacktriangle$ : 30%, $\blacktriangledown$ : 40%, and $\blacklozenge$ : 50% relative humidity). Each data point represents an interval of 0.05 second.....	39
Figure 3-6	Geometry for the mass transfer calculation.....	40
Figure 3-7	Proposed fiber cross sections for morphology evolution. Two groups: one without phase separation, from (a) through (d); and the other with phase separation, from (e) through (h).....	44
Figure 3-8	The competition among the phase separation, the solvent evaporation, and a buckling instability.....	47
Figure 3-9	SEM images of as-spun fibers electrospun from a 10 wt% PS/DMF solution under (a) 35% and (b) 24% relative humidity, and annealed ones from (c) 35% and (d) 24% relative humidity (scale bar: 5 $\mu\text{m}$ ). The insert images are cross-sectional TEM images.....	48
Figure 3-10	SEM images of randomly distributed as-spun nonwoven fabrics and aligned as-spun mats electrospun from 9-14 wt% PAN/DMF solution.....	49
Figure 3-11	Cross-sectional TEM images of as-spun fibers electrospun from a 14 wt% PAN/DMF solution under (a) 46% and (b) 31% relative humidity (scale bar: 500 nm), and annealed ones from (c) 46% and (d) 31% relative humidity (scale bar: 500 nm).....	50



Figure 3-12	The cross-sectional TEM image of as-spun fibers electrospun from (a) a 9% PAN/DMF and (b) a 11 wt% PAN/DMF solution under 31% relative humidity (scale bar: 500 nm).....	51
Figure 3-13	Other polymer systems producing porous fibers electrospun from DMF: poly(methyl methacrylate) (PMMA) and cellulose acetate (CA).....	51
Figure 3-14	Comparison between different theoretical models (line) and experimental data from 30 wt% PS/DMF solutions (■: 43%, ●: 37%, ▲: 29%, ▼: 24% relative humidity. Solid symbols: void volume fraction calculated from the shrinkage of fiber diameter, and open symbols: from analysis of TEM image).....	54
Figure 3-15	(a) Two-dimensional WAXD pattern, (b) WAXD diffractogram, (c) WAXD azimuthal scan, (d) polarized FTIR spectrum of electrospun PAN fibers, and (e) the enlarged version of the blue window in (d).....	56
Figure 4-1	Surface morphology of polymer fibers electrospun from (a) a 30 wt% PS/THF solution; (b) a 14 wt% PAN/DMF solution; (c) a 30 wt% PS/DMF solution; and (d) a 15 wt% PS in a mixed solvent of DMF and THF. Inset fibers outlined in white for emphasis.....	64
Figure 4-2	The interplay between core and shell energy contributions of the fiber is analogous to the classic problem of buckling of a beam on an elastic foundation (courtesy of Lifeng Wang).....	66
Figure 4-3	The illustration of properties and geometry of the core and shell.....	67
Figure 4-4	Dependence of critical wave number on $a/t$ for different $E_c/E_s$ . The lines are the Hermann and Forrestal analytical results of Equation (4-2) determined herein; the symbols are numerical results.....	68
Figure 4-5	Map of numerical results for wrinkled cross-section as a function of $E_c/E_s$ and $a/t$ , shown for each pair of $E_c/E_s$ and $a/t$ values indicated by the axis labels.....	69
Figure 4-6	(a) Dependence of $\lambda_{crit} / t$ on $E_c/E_s$ for different $a/t$ (solid line is the theory solution according to Equation (4-3); filled symbols correspond to lowest mode cases where $k_{crit} = 2$ and $\lambda_{crit} = \pi a$ ). (b) Surface patterns for different radius fibers with the same thickness $t$ at $E_c/E_s = 10^{-3}$ and $E_c/E_s = 10^{-2}$ , showing wavelength ( $\lambda_{crit} = 41t$ and $19t$ respectively) to be independent of fiber radius.....	70
Figure 5-1	Important Parameters in Oliver and Pharr's model [16].....	77
Figure 5-2	The force-deformation curves of nanoindentation measured by AFM and their derived modulus of the fiber.....	80
Figure 5-3	Four indent marks on a Nomex fiber.....	81
Figure 5-4	AFM images show that (a) epoxy diffused along the fiber; (b) the fiber can not sustain itself and failed on the trench; (c) the fiber was damaged during the image scanning; and (d) a fibers was carefully placed and secured with epoxy.	81
Figure 5-5	SEM images of individual PA 6(3)T fibers with different average diameters. Images (a) through (e) were taken under 10,000x magnification (scale bar = 1 $\mu\text{m}$ ), while images (f) through (l) were taken under 6000x magnification (scale bar = 2 $\mu\text{m}$ ).....	83
Figure 5-6	Cross-sectional images of the PA 6(3)T fibers cut under liquid nitrogen to confirm the nonporous and consolidated structures. SEM images were taken under 6,000x magnification (scale bar = 2 $\mu\text{m}$ ).....	84
Figure 5-7	Representative stress-strain curves of individual fibers. The figure on the right hand side accentuates the small engineering strain of the figure on the left hand side.....	84
Figure 5-8	Dependence of (a) Young's modulus and (b) yield stress on fiber diameter. Filled diamonds represent experimental data for individual fibers deformed in uniaxial	87

extension; open circles represent values obtained from molecular orientation measurements using Ward's aggregate model [41]; solid lines represent experimental values for bulk films; dashed lines represent one standard deviation(c) The moving average on Figure 5-8(a).....

Figure 5-9	(a) Polarized FTIR of representing PA 6(3)T single fiber with different diameters. Solid lines represent $A_{\perp}$ , and dotted lines represent $A_{\parallel}$ . (b) The overall molecular orientation versus the fiber diameter.....	89
Figure 5-10	Distribution of fiber orientation within aligned bundles of fibers used for molecular orientation determination. (a) ~ (c) SEM images of fiber bundles with different average fiber diameter. Images were taken under 1000x magnification (scale bar = 10 $\mu\text{m}$ ). (d) ~ (f) The distribution of fiber orientation within bundles corresponding to SEM images (a) ~ (c), respectively, determined by image analysis.....	90
Figure 6-1	Schematic of a 4-fiber model with square region ( $2a \times 2b$ ) representing the RVE before deformation and the rectangular region ( $2\lambda_1 a \times 2\lambda_2 b$ ) representing the RVE after deformation.....	98
Figure 6-2	(left) Schematic of a curving fiber with a radius of curvature $R_1$ , and a straight fiber with infinite curvature and fiber length $2L$ , under the same loading force $P$ ; (right) cross-section of a fiber with diameter $d$ , and arbitrary $t = \sin x \cdot d/2$ .....	101
Figure 6-3	Representative SEM images of PA 6(3)T nonwoven fabrics with different diameters (scale bar = 5 $\mu\text{m}$ ).....	104
Figure 6-4	Schematic illustration of the radius of curvature ( $R_1$ ), the distance between the adjacent junctions ( $2L$ ), and the diameter of fibers ( $d$ ).....	106
Figure 6-5	Dependence of (a) Young's modulus of nonwoven fabrics on fiber diameter, and (b) Young's modulus of single fibers on fiber diameter. Filled diamonds represent experimental data in uniaxial extension; open circles represent values obtained from molecular orientation measurements using Ward's aggregate model [4]. Filled triangles represent derived Young's modulus of the single fiber from mat data assuming straight fibers, and open triangles represent that assuming sinuous fibers.....	108
Figure 6-6	The logarithmic relation of (a) radius of the curvature and fiber diameter; (b) distance between adjacent junctions and fiber diameter.....	109

## List of Tables

Table 2-1	Parameters in Equation (2-2).....	22
Table 3-1	Diameters of PS Single Fibers.....	32
Table 3-2	Parameters Used to Construct the Ternary Phase Diagram.....	40
Table 3-3	Parameters Used in Mass Transfer Calculation.....	42
Table 3-4	Comparison for Different Time Scale.....	46
Table 3-5	Mechanical properties of as-spun and annealed PAN fibers.....	56
Table 5-1	Mechanical properties of a single electrospun fiber by the tensile test.....	76
Table 5-2	Mechanical properties of a single electrospun fiber by nanoindentation.....	77
Table 5-3	Mechanical properties of a single electrospun fiber by AFM bending test.....	78
Table 5-4	Mechanical properties of a single electrospun fiber by resonance test.....	78
Table 5-5	Preliminary results by UTM T150 universal tensile testing system.....	79
Table 5-6	Processing parameters of electrospinning and resulting fiber diameter.....	83
Table 5-7	Data for Ward's Aggregate Model.....	89
Table 6-1	Data for the modified model for fibers with curvature and the results.....	105

# Chapter 1 Introduction

## 1.1 Motivation

Electrospinning is a technique [1] used to produce polymeric nonwoven fabrics comprising small fibers with diameters that average from a few tens of nanometers to microns. Electrospun nonwoven fabrics can be used in a variety of applications [2,3], such as reinforcements in composites, filtration, tissue engineering, fuel cell membranes, catalytic systems, and sensors. Recently, a length scale effect on physical properties of materials has attracted great attention because of the potential to produce new materials with unique behavior. These physical properties include mechanical, electrical, thermal, and optical properties. Among these areas, we are interested in the possible remarkable changes in mechanical properties that may occur in electrospun nanofibers due to a size effect. Because the mechanical properties of a material are essential to its utility in all applications, we desire to understand whether smaller fibers are stiffer or stronger, as well as whether the nonwoven fabrics they compose exhibit enhanced properties. However, comprehensive understanding is still lacking.

The first step of my research is a fundamental study on the mechanical properties of a single fiber with different diameters, ranging from commercial fibers with diameters of tens of microns down to nanofibers with diameters as small as tens of nanometers produced by electrospinning. The study on commercial fibers is intended to validate our measurement methods applied to nanofibers, including my use of new experimental instruments such as the Nano Bionix® universal tensile testing system. I focus my research first on high performance materials, such as Kevlar, Nomex, and PAN-derived carbon fibers. Because these materials cannot be electrospun into fibers over a wide range of average fiber diameter, it is difficult to explore the size effect on mechanical properties by studying individual fibers of these materials. Therefore, an amorphous polyamide is chosen as an alternative. During the process of investigating the size effect on mechanical properties of these electrospun fibers, we discovered that the structures and morphology of fibers can

be tailored by varying the conditions of the electrospinning process, which in turn affect the fiber properties and are important to their mechanical properties. As a result, the goal of my research is to understand the mechanical properties of electrospun polymeric fibers as a function of their diameter, internal structures, and external topographies.

The objectives of my research are as follows:

- (1) Investigation on internal structures and external topographies of electrospun fibers in terms of the competition among the phase separation, solvent evaporation, and buckling instability, in order to understand the effects of these parameters on mechanical properties.
- (2) Assessment of the accuracy and feasibility of different experimental techniques for the measurement of the mechanical properties of a single fiber.
- (3) Assessment of the size effects of electrospun single fibers on their stiffness and strength, in an effort to understand if there exists an emergent behavior of the nanoscale material that differs from that of the macroscopic bulk material, and what the possible explanation and mechanisms for such phenomena are.
- (4) Construction of micromechanical models to relate the stiffness of single electrospun fibers and that of their nonwoven fabrics quantitatively in terms of the fiber network, fiber curvature, intrinsic fiber properties, and fiber-fiber junction, so that the mechanical performance of the nonwoven fabrics can be optimized according to these parameters.

## **1.2 Background**

### **1.2.1 Electrospinning**

The basic principle of electrospinning [3-8] is that an electrified jet forms when the free surface of a highly elastic polymer solution is charged to a high voltage in the presence of an electric field. The jet undergoes continuous stretching as it accelerates downfield toward the collector, thinning further at a very high strain rate ( $\sim 1000/s$ ) upon the onset of the whipping instability, as shown in Figure 1-1. The interconnected network of fibers results in a material with high specific surface area ( $\sim 100 \text{ m}^2/\text{g}$ ) and high porosity ( $\sim 90\%$ ). These electrospun fibers have many

possible structures and morphology, as shown in Figure 1-2, such as flat ribbons, beads-on-string, and pores on the surface. Compared to metallic fibers, polymeric fibers often have higher specific strength and modulus because of the low density of organic materials. They can be then easily modified to improve properties, e.g., by modifying the fiber surface using chemical or physical vapor deposition. In addition to the simplest structure of a monolithic fiber, it is feasible to prepare secondary structures such as a core/shell fiber structure and also nanofibers with hollow interiors or with porous structures by using a co-axial (two-fluid) electrospinning [7].

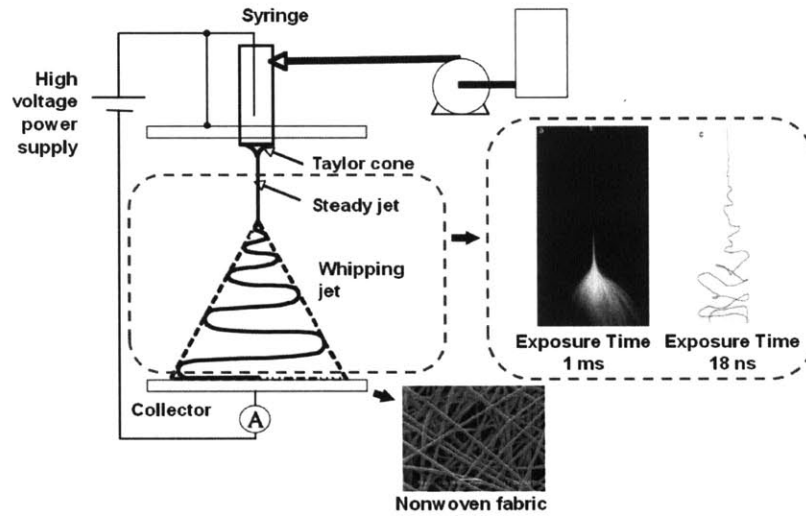


Figure 1-1. Electrospinning setup (modified from [1] and courtesy of Rutledge group).

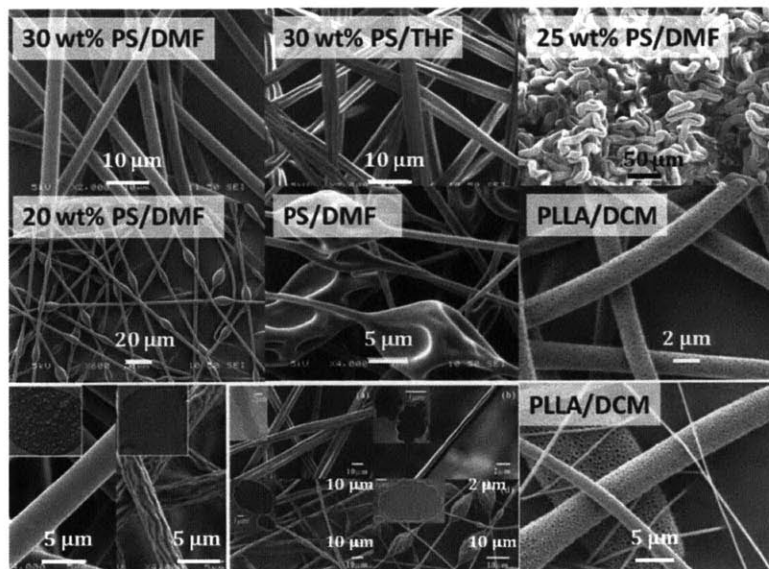


Figure 1-2. Possible structures and morphology of electrospun fibers.

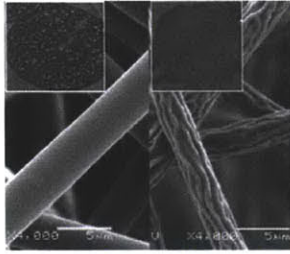
### **1.2.2 Applications**

Electrospun fibers can be used in many applications, summarized in Ref. [9]. They can be classified into tissue engineering scaffolds, filtration media, industrial applications (electronic/optical), nanosensors, military protection clothing, cosmetic skin masks, and life science applications. Companies such as Donaldson and Finetex have been using electrospun fibers in their products, such as for air and liquid filtration. Among all these applications, mechanical integrity is the key to their practical usage, where our fundamental and systematic study focuses.

The advantages of electrospun fibers is that they can be made very easily and have higher specific surface area than commercial fibers, which make them a better choice for highly surface-related applications. However, some disadvantages exist for electrospun fibers. For example, low productivity is an issue that needed to be solved for massive production in industry. Many efforts have been done to improve mass production in several organizations, such as Elmarco s.r.o. (Czech Republic), Hills Inc. (USA), Kato Tech Co., Ltd. (Japan), Fulence (Japan), MECC Co., Ltd (Japan), Donaldson Co., Inc. (USA), Finetex Technology (USA), Hirose Paper MFG (Japan), Japan Vilene (Japan), and Public Organization NEDO (Japan) [10].

### **1.3 Thesis Overview**

This thesis contains seven chapters. Chapter 1 covers my motivation for this research, a brief introduction to the electrospinning, and an overview about this thesis. Chapter 2 describes the experimental methods, including the materials used in this study, the sample preparation, and different instruments and techniques to characterize properties of these fibers. Contents starting from Chapter 3 to the end of Chapter 6 are the main story of this thesis: to investigate the mechanical properties of electrospun fibers as a function of their structures, morphology, and size, as shown in Figure 1-3.



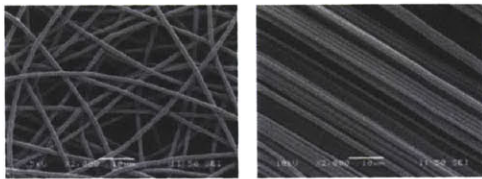
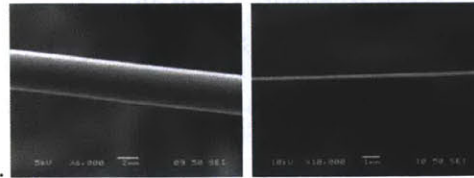
➤ **Mechanical properties of electrospun fibers as a function of their size, structures, and morphology.**

**A. Study internal structures and external morphology of electrospun fibers, and their effect to mechanical properties.**  
 Competition between phase separation, solvent evaporation, and a bulking instability.

**B. Size effects of single electrospun fibers on stiffness and strength.**

Better than bulk material?

Possible explanation? Crystallinity, molecular orientation, confined structures, surface energy, ...



**C. Relation of stiffness and strength between single electrospun fibers and their nonwoven.**

Fiber network (random, aligned), fiber curvature, fiber properties, fiber-fiber junction (friction, bonding),...

Figure 1-3. Overview of objectives.

In Chapter 3, we begin to understand which structures and morphology form under a given set of conditions through the comparison of three characteristic times: the drying time, the buckling time and the phase separation time. These structures and morphology have important consequences for the mechanical properties of the fibers. In Chapter 4, the critical wave number and wavelength of wrinkled surface topographies of electrospun fibers observed in experiments are analytically and numerically analyzed in terms of important physical parameters of fibers. In Chapter 5, we study the size effects of single electrospun fibers on their stiffness and strength. In Chapter 6, two quantitative microstructure-based models that relate the Young's modulus of the fabrics to that of the fibers are considered, one assuming straight fibers and the other allowing for sinuous fibers. Finally, in Chapter 7, we summarize our work and contribution, and provide future direction for continued work in this field.



## 1.4 References

- [1] Shin YM, Hohman MM, Brenner MP, Rutledge GC. "Electrospinning: A whipping fluid jet generates submicron polymer fibers", *Appl. Phys. Lett.* 2001; 78(8): 1149-51.
- [2] Huang ZM, Zhang YZ, Kotaki M, Ramakrishna S. "A review on polymer nanofibers by electrospinning and their applications in nanocomposites", *Compos. Sci. Technol.* 2003; 63: 2223-53.
- [3] Li D, Xia Y. "Electrospinning of Nanofibers: Reinventing the Wheel?", *Adv. Mater.* 2004; 16(14): 1151-70.
- [4] Hohman MM, Shin M, Rutledge GC, Brenner MP. "Electrospinning and electrically forced liquid jets: I. Stability theory", *Phys. Fluids* 2001; 13(8): 2201.
- [5] Hohman MM, Shin M, Rutledge GC, Brenner MP. "Electrospinning and electrically forced liquid jets: II. Applications", *Phys. Fluids* 2001; 13(8): 2221-2236.
- [6] Fridrikh SV, Yu JH, Brenner MP, Rutledge GC. "Controlling the fiber diameter during electrospinning", *Phys. Rev. Lett.* 2003; 90: 144502.
- [7] Yu JH, Fridrikh SV, Rutledge GC. "Production of submicrometer diameter fibers by two-fluid electrospinning", *Adv. Mater.* 2004; 16: 1562.
- [8] Yu JH, Fridrikh SV, Rutledge GC. "The role of elasticity in the formation of electrospun fibers", *Polymer* 2006; 47: 4789.
- [9] Burger C, Hsiao BS, Chu B. "Nanofibers materials and their applications", *Annu. Rev. Mater. Res.* 2006; 36: 333-368.
- [10] Teo WE, Inai R, Ramakrishna S. "Technological advances in electrospinning of nanofibers", *Sci. Technol. Adv. Mater.* 2011; 12: 013002.

## Chapter 2 Experimental Methods

### 2.1 Materials

Atactic polystyrene (PS,  $M_w = 280$  kg/mol,  $T_g = 100^\circ\text{C}$ ), poly(L-Lactide) (PLLA, inherent viscosity  $\sim 4.0$  dl/g), polyacrylonitrile (PAN,  $M_w = 150$  kg/mol), cellulose acetate (CA,  $M_n = 50$  kg/mol), poly(ethylene oxide) (PEO,  $M_v = 2\text{M}$  kg/mol), formic acid (FA, ACS reagent, 96%), tetrahydrofuran (THF, CHROMASOLV<sup>®</sup> Plus, for HPLC,  $\geq 99.9\%$ ), chloroform (CHROMASOLV<sup>®</sup> Plus, for HPLC,  $\geq 99.9\%$ ), dimethylformamide (DMF, ACS reagent,  $>99.8\%$ ), N,N-Dimethylacetamide (DMAc, CHROMASOLV<sup>®</sup> Plus, for HPLC,  $\geq 99.9\%$ ), 1,1,1,3,3,3-Hexafluoro-2-propanol (HFIP), dichloromethane (DCM), lithium chloride (LiCl) were purchased from Sigma Aldrich, Inc. Atactic PS ( $M_w = 2000$  kg/mol), polycarbonate (PC,  $M_w = 60$  kg/mol), poly(methyl methacrylate) (PMMA,  $M_w = 540$  kg/mol), Poly(hexamethylene adipamide) (PA 6/6 or Nylon 6/6,  $T_g = 45^\circ\text{C}$ ), poly(trimethyl hexamethylene terephthalamide) (PA 6(3)T or Nylon 6(3)T,  $M_v = 15$  kg/mol,  $\rho = 1.12$  g/cm<sup>3</sup>,  $T_g = 140^\circ\text{C}$ ) were purchased from Scientific Polymer Product, Inc. Kevlar 29<sup>®</sup> and Nomex<sup>®</sup> bundles were kindly provided by DuPont, Wilmington DE. Polypropylene (PP) was provided as a standard for the U9815A UTM T150 universal tensile testing system by Agilent Technologies, Santa Clara CA. All materials were used without further purification.

### 2.2 Sample Preparation

A 30 wt% solution of PS ( $M_w = 280$  kg/mol) and 10 wt% solution of PS ( $M_w = 2000$  kg/mol) were dissolved in DMF under gentle stirring for at least 24 hours at  $50^\circ\text{C}$ . PAN was dissolved in DMF to form 9 wt%, 10 wt%, 11 wt%, 12 wt%, 13 wt% and 14 wt% solutions under gentle stirring for several hours at  $60^\circ\text{C}$ . CA (0.9 g) and PEO (0.015 g) were dissolved together in DMF (14.1 g) at  $55^\circ\text{C}$  to form a solution with 6 wt% CA and 0.1 wt% PEO. PC was dissolved in chloroform to form a 15 wt% solution at  $50^\circ\text{C}$ . Nomex and LiCl were dissolved together in DMAc under sonication to form a solution with 20 to 25 wt% Nomex and 5 wt% LiCl. All solutions were cooled down to room temperature before electrospinning. PA 6(3)T was dissolved

in DMF to form 30 wt% and 36 wt% solutions, and in a mixture of DMF:FA with the weight ratio of 99:1 to form 22 wt%, 28 wt%, and 30 wt% solutions. PLLA was dissolved in DCM to form a 5 wt% solution. Nylon 6/6 was dissolved in HFIP to form 8 wt% and 10 wt% solutions. PMMA can be dissolved in DMF, DMAc, and THF to form 10 wt% to 15 wt% solutions. Solutions of PA 6(3)T, PLLA, Nylon 6/6, and PMMA were prepared at room temperature. In order to provide a uniform electric field and to eliminate corona discharges, the parallel-plate electrospinning setup described by Shin et al. [1], was used in our experiments. The flow rate ( $Q$ ), plate-to-plate distance ( $D$ ), and voltage ( $V$ ), respectively, were: 0.01 ml/min, 34 cm, and 30 kV for the 30 wt% PS solution, and 0.01 ml/min, 34 cm, and 24 kV for the 10 wt% PS solution. The flow rate, plate-to-plate distance, and voltage, respectively, were: 0.002 to 0.05 ml/min, 33 to 53.5 cm, 30 to 40 kV, varied for the PA 6(3)T solutions; 0.01 to 0.07 ml/min, 35 cm, 28 to 36.5 kV for the PLLA solution; 0.01 to 0.03 ml/min, 30 to 38 cm, 26 to 35 kV for the PAN solutions; 0.05 ml/min, 35 cm, 28 kV for the CA/PEO solution; 0.02 to 0.05 ml/min, 35 cm, 25 to 28 kV for the Nylon 6/6 solution; 0.005 to 0.1 ml/min, 34 to 55 cm, 10 to 38 kV for the PMMA solutions; 0.01 to 0.08 ml/min, 34 cm, 35 kV for the PC solution; and 0.0001 to 0.002 ml/min, 30 cm, 25 to 38 kV for the Nomex solution. For the electrospinning of the Nomex solution, because we added salt (LiCl) in the solution, the electrified jet was highly conductive and the fibers had to be collected by a rotating drum. The applied electric field is  $E_{\infty} = V/D$ . The electric current ( $I$ ) carried by the jet was obtained by measuring the voltage drop across a 1.0 M resistor between the collector plate and ground with a digital multimeter (Fluke 85 III) and converting to electric current using Ohm's law [2].

In each case, we generally collected randomly oriented nonwoven meshes on a grounded aluminum foil, as well as several single fibers on paper templates. A "Y" shaped copper wire was used to harvest individual fibers from the electrospinning process, and these were transferred to paper templates for subsequent mechanical evaluation. In addition, for later characterization, bundles of aligned fibers were collected by using two parallel conductive strips to orient the charged fibers with the electric field lines so that they span the gap between the conductive strips [3].

The weight of each bundle is about 1 mg, and the volume of the bundle is about 5 mm in width, 10  $\mu\text{m}$  in thickness, and 2 cm in length. Before characterization, some of the samples of single electrospun polymer fibers (with length held fixed when annealed) and of polymer mats were annealed at  $\sim 10^\circ\text{C}$  above  $T_g$  for 2 hours. The annealing protocol is sufficiently close to the glass transition temperature of the polymer and of short duration so that the integrity of the fibers was not compromised. After the heat treatment, all samples were slowly cooled back to room temperature before subsequent analysis. To make thin films for measuring the properties of the bulk material, we can either use polymer pellets to fuse under the hot press at sufficiently high temperature for certain time (e.g.  $260^\circ\text{C}$  and 4 hr for PA 6(3)T) and cooled back to room temperature, or use polymer solution to cast the film.

## **2.3 Characterization**

### **2.3.1 Morphological and Structural Characterization**

Scanning electron microscopy (SEM) (JEOL-6060SEM, JEOL Ltd., Japan) was used with an acceleration voltage of 5 to 10 kV and 10 to 15 mm working distance for morphological characterization and determination of fiber diameter. Fiber samples were sputter-coated with a 3-4 nm layer of gold using a Desk II cold sputter/etch unit (Denton Vacuum LLC, Moorestown NJ). The orientation and curvature distribution of fibers within bundles or randomly distributed nonwoven fabrics can be determined by image analysis of properly taken SEM images. Transmission electron microscopy (TEM) (JEOL JEM200CX TEM, JEOL Ltd., Japan) was used for the observation of interior structures. Fibers were embedded in Eponate 12 resin (Ted Pella, Inc. Redding CA) and cured at  $60^\circ\text{C}$  for 16-24 h. The cross-linked resin was cut into 60 nm slices using a microtome (EM UC6, Leica, Germany) with a diamond blade (DiATOME) and then deposited onto a 300 mesh Cu grid for examination by TEM. Atomic force microscopy (AFM) (Nanoscope V with Dimension 3100 D31005-1, Veeco, Plainview NY) was used for high spatial resolution imaging of surfaces (image mode: x- or y-direction resolution is 2-10 nm, and z-direction resolution is 0.1 nm ) and also for high sensitivity force (indentation and pulling)

experiments (force mode: the force can be 200 pN or less). Wide-angle X-ray diffraction (WAXD) (ASSY 610-004378, Molecular Metrology, USA) was used to measure the degree of crystallinity and the molecular orientation of semi-crystalline polymers. We used bundles of aligned fibers for the WAXD measurement. The data were analyzed by POLAR (Stony Brook Technology, Version 2.7.0, USA), a software for the small-angle X-ray scattering (SAXS) and WAXD image processing.

A Nicolet Nexus Fourier transform infrared (FT-IR) spectrometer with a polarizer (Thermo Fisher Scientific, Waltham MA) was used to measure polarized infrared spectra in the transmission mode and recorded at a resolution of 2 cm<sup>-1</sup> in the range of wavenumber from 1000 to 4000 cm<sup>-1</sup>. We used bundles of aligned fibers for the FT-IR measurement, characterized by their average fiber diameter, not just a single fiber, due to limitations in sensitivity of the instrument. According to Ref. [4] and [5], the sample thickness should be from 5 to 15 μm for transmission testing in FTIR. If the thickness of the sample is too thin, the high transmittance will cause bad resolution because of the low absorbance. Polarized FTIR was used to determine the molecular orientation within the bundle. The dichroic ratio  $D = A_{||}/A_{\perp}$ , where  $A_{||}$  and  $A_{\perp}$  are the absorbances measured with the incident beam polarized parallel and perpendicular to the fiber bundle axis, respectively. The imperfect alignment of fibers in bundles contributes some inaccuracy to the determination of the dichroic ratio for individual fibers. In order to minimize this effect,  $A_{||}$  was measured at three different angles of the incident beam (-10°, 0°, 10°); similarly,  $A_{\perp}$  was also measured at three angles (80°, 90°, 100°). The dichroic ratio for the fiber bundle was taken to be the maximum value calculated from the three sets of angles. The overall molecular orientation [6],  $f_2$ , and the angle between the molecular axis and the fiber bundle axis,  $\Omega$ , are shown in Figure 2-1 using PA 6(3)T as an example and can be calculated as:

$$f_2 = \left[ 3 \langle \cos^2 \Omega \rangle - 1 \right]^{1/2} = \frac{(D-1)/(D+2)}{(2 \cot^2 \alpha - 1)/(2 \cot^2 \alpha + 2)} \quad (2-1)$$

where  $\alpha$  is selected to be the angle between the molecular axis and the transition moment of a functional group (e.g. the amide carbonyl group (C=O) for PA 6(3)T).  $f_2$

$f_2 = 1$  represents perfect uniaxial alignment of molecules along the fiber axis,  $f_2 = 0$  represents random orientation, and  $f_2 = -1/2$  represents molecular alignment perpendicular to the fiber axis.  $\alpha$  can be estimated using the Gaussian® 03 program [7] or found in the literature. For example, we use the Gaussian® 03 program to estimate  $\alpha$  for PA (3)T. First, the geometry optimization of a single chain of PA 6(3)T, represented by a single repeat unit of the chain and periodic boundary conditions in the molecular axis direction, was performed to locate the conformational minima on the potential energy surface by using the density functional theory at the B3LYP level and 6-31G basis set, from which we found  $\alpha = 76^\circ$ .

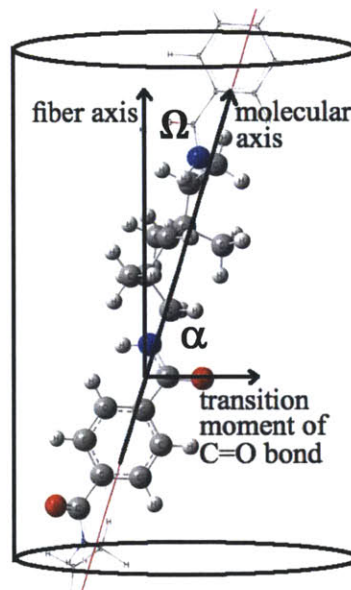


Figure 2-1. The illustration of molecular orientation of PA 6(3)T.

To understand the fringing effect to my samples in FTIR, originating from the constructive and destructive interference of the IR beam from these surfaces of the sample, two references were given by Prof. Gleason [8-9]. First, the FTIR spectrum is reviewed to see whether obvious fringes in the sample are observed. Also, the equation given by these two papers are used to check the fringing effect further.

$$b = \frac{N}{2n(\nu_1 - \nu_2)} \quad (2-2)$$

where  $b$  is the film thickness ( $\sim$ fiber diameter),  $N$  is the number of fringes,  $n$  is the reflective index of the sample, and  $\nu_1$  and  $\nu_2$  is the start and end point of wave number to calculate the number of fringes. In our case, the important pattern for PA 6(3)T is between the experimental data in the range of  $\nu_1 = 1585$  to  $\nu_2 = 1678 \text{ cm}^{-1}$ . We also know  $n = 1.5660$  for PA 6(3)T, and the fiber diameter we are interested is from  $b = 170 \text{ nm}$  to  $3643 \text{ nm}$ . Only  $N$  is unknown in Equation (2-2). We used Equation (2-2) to calculate  $N$ , and we found:

Table 2-1. Parameters in Equation (2-2)

d (nm)	d (cm)	N
170	1.70E-05	0.0050
288	2.88E-05	0.0084
385	3.85E-05	0.0112
407	4.07E-05	0.0119
612	6.12E-05	0.0178
850	8.50E-05	0.0248
1387	1.39E-04	0.0404
1723	1.72E-04	0.0502
2396	2.40E-04	0.0698
3643	3.64E-04	0.1061

$N$  is smaller than 1 for all our samples of PA 6(3)T, which means we cannot find the fringe in our amide carbonyl peak ( $\text{C=O}$ ) around  $1640 \text{ cm}^{-1}$ . Also, our calculated molecular orientation comes from the intensity ratio of the  $A_{\parallel}$  and  $A_{\perp}$ . Therefore, the fringing effect is more likely to be cancelled out and contributes less if it exists. The conclusion is that it is reasonable for us to believe our results of molecular orientation without considering the fringing effect.

### 2.3.2 Mechanical Characterization

A Zwick mechanical tester (Model BTC-EXMACRO.001, Roell, Germany) was used to measure the Young's moduli and yield strength of the nonwoven mat samples in uniaxial tension performed at a typical strain rate of  $10^{-3} \text{ s}^{-1}$ . The data of local axial and transverse strain can be obtained by adding dots on the nonwoven fabrics using

a black marker, as shown in Figure 2-2, and then being monitored with a Point Grey Grasshopper video extensometer to track the positions of the points during the measurement. These data are then analyzed with the Vic2d software package from Correlated Solutions to calculate the displacement of points in a pixel based coordinate system. A U9815A UTM T150 universal tensile testing system (Agilent Technologies, Santa Clara CA), which is also formerly the Nano Bionix® universal tensile testing system (MTS Systems Corp, USA), was used to measure the force versus elongation behavior of individual electrospun fibers in uniaxial tension at a strain rate of  $10^{-3} \text{ s}^{-1}$  and gauge length of 15 mm. Once the paper template was mounted on the machine, the edges of the cut-out region of the template, as indicated by the black dotted line in Figure 2-3(a), were cut to attain the freestanding single fiber for testing. The schematic stress-strain curve for single fibers is shown in Figure 2-4, from which we determine the Young's modulus, tensile strength and elongation to break of individual electrospun fibers. The Young's modulus is determined by linear regression of the stress-strain data in the range of strain from the origin to a strain about 0.02. The yield point is determined by Coplan's construction, as shown in Figure 2-4, also known as the "tangents technique" [10].

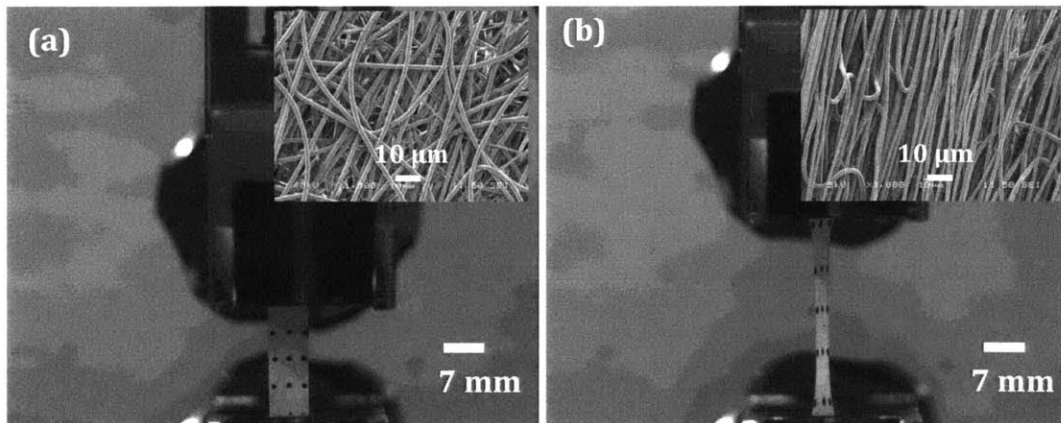


Figure 2-2. The nonwoven fabrics (a) before deformation and (b) after deformation tested by a Zwick mechanical tester with marked dots on it. The insert images are SEM images of these nonwoven fabrics.



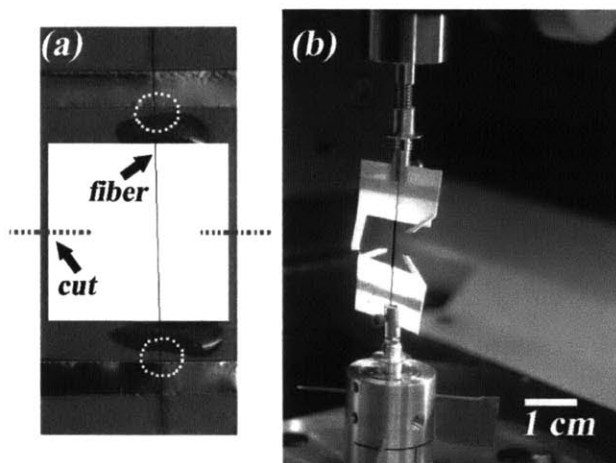


Figure 2-3. Tensile test configuration: (a) the paper template (shown in gray) for gripping the fiber with fiber spanning the cut-out region, and (b) the setup for tensile testing of a single fiber with the paper template (shown in white) secured in test position and then cut, readying the fiber for testing. Note that the fiber diameter is artificially enlarged in the images in order to be seen.

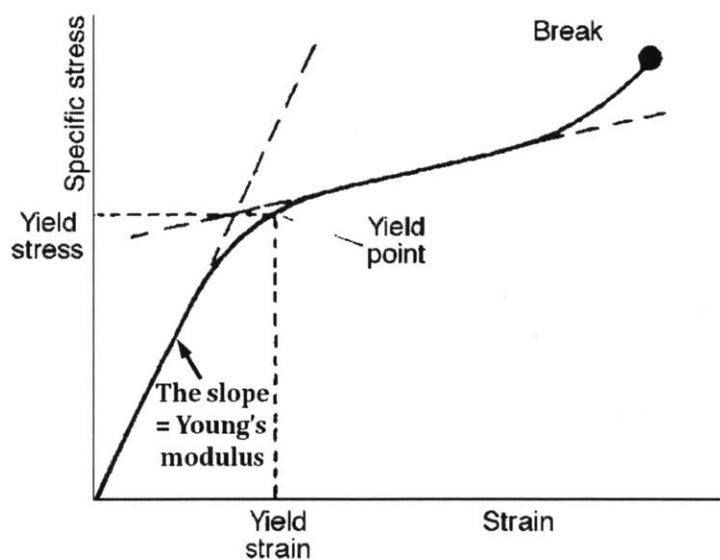


Figure 2-4. Coplan's construction for the determination of yield point [10].

### 2.3.3 Thermal Characterization

A thermogravimetric analyzer (TGA) (Q50, TA instruments, USA) can be used to determine the content of residual solvent left in the electrospun fibers. A

Differential Scanning Calorimeter (DSC) (Q1000 [090001.901, TA instruments, USA] was used to determine the  $T_g$  and  $T_m$  of the polymer.

#### **2.3.4 Characterization for Phase Separation**

The cloud point is determined by slowly adding nonsolvent into the polymer/solvent solution until the solution turns turbid. Different concentrations of polymer solutions (for example, 5, 10, 15, 20, 25 and 30 wt%) should be prepared and tested. Note that sometimes local turbidity happens immediately at the interface of the titrated nonsolvent and the polymer/solvent solution; further stirring of the solution for several minutes to a few hours is needed in order to achieve the bulk equilibrium condition. The amount of nonsolvent is continuously increased and the solution stirred until the transition from a transparent solution to a turbid solution can be observed at equilibrium. The transition could be apparent and determined by the naked eye without the aid of a spectrophotometer.

#### **2.3.5 Mat properties**

An Autopore IV 9500 mercury penetrometer (Micromeritics, Norcross, GA) was used to measure the porosity of nonwoven fabrics. The default equation used by this machine to calculate the porosity is not working well. We modify it and propose a new equation for the porosity. The equations and the example are listed in Appendix I. An adjustable Measuring Force Digimatic Micrometer (Model CLM1 .6"QM, Mitutoyo, Japan) was used to measure the thickness of nonwoven fabrics at force equal to 0.5 N (or pressure equal to 0.177 MPa). Using a normal micrometer to measure thickness usually over-compresses the sample and underestimates the thickness, and thus overestimates the Young's modulus. Therefore, it is necessary to report the thickness of nonwoven fabrics at constant applied pressure during the measurement.

#### **2.3.6 Computational Aid**

Scion image processing software (National Institutes of Health, USA) and AnalySIS image processing software (Soft Imaging System Corp., USA) were used to

analyze the fiber diameter. For example, after the tensile testing, the undeformed section of fiber between the copper tape and the epoxy glue, illustrated by dotted white circles in Figure 2-3(a), is sputter coated with a thin layer of gold for imaging by SEM, to determine the undeformed fiber diameter. For each SEM image of a single fiber, measurements were taken at five different positions along the fiber to ascertain the uniformity of the fiber. Sections from both ends of each fiber from the white circles in Figure 2-3 were imaged and analyzed; any test in which the ends differed in diameter by more than 10% was discarded. We assume that the average fiber diameter measured in this way from several fibers (at least ten fibers) collected in a single electrospinning experiment is representative of the distribution of fiber diameters in the randomly oriented nonwoven fabrics of the same experiment. We can also measure the fiber diameters directly from the SEM of these nonwoven fabrics.

Void volume fraction inside the fibers can be analyzed with the help of Scion image processing software. The void volume fraction was determined by two methods, from the shrinkage of fiber diameter during annealing and from analysis of TEM images before and after annealing. In the first method, the void volume fraction  $f$ , was evaluated as  $f = 1 - (d_{annealed}^2 / d_{as-spun}^2)$  where  $d_{as-spun}$  is the average diameter of the as-spun fibers and  $d_{annealed}$  is the average diameter of the fibers after annealing. This method assumes that the annealed fibers are nonporous, which can be confirmed by TEM. In the second method for determining void volume fraction, Scion image processing software is used to set the threshold that can distinguish an image into objects of interest and background on the basis of gray level for the cross-sectional TEM image, and then the area of voids within the fiber can be analyzed. We determine the diameter for each void and the total void volume fraction within the fiber by performing area fraction measurements and comparing the total cross-section of voids to that of the fiber. If the voids are sectioned randomly, this void area fraction measurement should provide a reasonable estimate of the true void volume fraction. The accuracy of the void volume fraction from the shrinkage of fiber diameter depends significantly on the standard

deviation of fiber diameters. Smaller standard deviation of fiber diameters, which means more uniform fiber diameters, permits a more precise estimation of void volume fraction. Even variations of  $\pm 5\%$  in the average of fiber diameter can lead to almost 10% difference in the porosity estimation. As for the TEM image analysis, voids smaller than a certain size compared to the fiber diameter will be easily overlooked due to the resolution and quality of the TEM images. The void volume fraction from TEM images might represent a lower limit of porosity if the grayscale threshold of contrast between the matrix and the void is properly executed. Therefore, both of these analyses yield at best only an approximate estimation of the actual porosity of the fibers.

Nonlinear finite element analysis (FEA) using the ABAQUS/STANDARD [11] was used to study buckling patterns numerically and conducted by my collaborator Lifeng Wang, a post doc in the Boyce Group. The mesh density was varied to ensure that the solutions obtained for the buckling wave number and wavelength were sufficiently converged.

We use Matlab (R2008a and R2010b, The Mathworks Inc.) to calculate the spinodal and binodal curves for ternary phase diagrams and their mass transfer paths (representative codes are given in Appendix II and Appendix III), and to calculate the orientation and curvature distribution of nonwoven fabrics using image analysis (representative codes and the example are given in Appendix IV, which need further improvement).

## 2.4 References

- [1] Hohman MM, Shin M, Rutledge GC, Brenner MP. "Electrospinning and electrically forced liquid jets: II. Applications", *Phys. Fluids* 2001; 13(8): 2221-2236.
- [2] Yu JH, Fridrikh SV, Rutledge GC. "The role of elasticity in the formation of electrospun fibers", *Polymer* 2006; 47: 4789-4797.
- [3] Li D, Wang Y, Xia Y. "Electrospinning of polymeric and ceramic nanofibers as uniaxially aligned arrays", *Nano Lett.* 2003; 3(8) : 1167-1171.
- [4] Yu W, Xiong L. "Effect of Various Morphology and Testing Conditions on Fiber Infrared Spectrum", *Journal of Applied Polymer Science* 2005; 96: 1003-1010.

- [5] Continuum User's Guide. Nicolet Instrument Corporation: Madison 1999: 1-6.
- [6] Wang M, Yu JH, Kaplan DL, Rutledge GC. "Production of submicron diameter silk fibers under benign processing conditions by two-fluid electrospinning", *Macromolecules* 2006; 39(3): 1102-1107.
- [7] Frisch MJ, Trucks GW, Schlegel HB, Scuseria GE, Robb MA, Cheeseman JR, et al. Gaussian Inc.: Pittsburgh, PA; 2003.
- [8] PIKE Technologies Application Note - 0502 "Calculating the Thickness of Free-Standing Films by FTIR".
- [9] Pistorius AMA, DeGrip WJ. "Deconvolution as a tool to remove fringes from an FT-IR spectrum", *Vibrational Spectroscopy* 2004; 36: 89-95.
- [10] Ward, I.M. Mechanical properties of solid polymers, 2nd ed. Wiley, New York, 1983.
- [11] ABAQUS/STANDARD Version 6.6 Users' Manual, ABAQUS Inc., Providence, RI, 2006.

## **Chapter 3 Morphology of Porous and Wrinkled Electrospun Fibers**

### **3.1 Introduction**

It is necessary to understand the process-structure-property relationships of electrospun polymer fibers in order to study the size effects on their mechanical properties accurately, because different morphologies and structures of the fiber resulting from varied processing parameters of electrospinning have a significant effect on their properties. Before a comprehensive understanding of the size effect of mechanical properties can be achieved, processing must be controlled in order to eliminate morphological variations that may accompany efforts to produce fibers with different diameters, and the reproducible formation of the desired structures confirmed.

It is well known [1] that under certain conditions fibers produced by wet or dry spinning techniques can exhibit some porosity. For example, fibers produced by dry spinning typically have a larger internal volume fraction of porosity than those produced by melt spinning. The reason is that melt spinning does not involve a dramatic change in the volume fraction of polymer, while in dry spinning the effect of solvent-polymer interaction and rate of solvent removal need to be considered.

Porous surface morphologies [2-6] have been observed in fibers electrospun from solution in a low boiling point solvent; this surface porosity can be varied by controlling the relative humidity (RH) of the environment and the molecular weight of the polymer [2]. Kyu and coworkers [7-9] studied the temporal evolution of the fiber morphology theoretically, in the framework of the Cahn-Hilliard phase field approach and the Flory-Huggins free energy of mixing. Their work captures the basic features by which the fiber morphology in a polymer-solvent system undergoing solvent evaporation depends on the competition between the dynamics of phase separation and the rate of solvent evaporation. Their simulations predicted morphologies that ranged from smooth hollow fibers to fibers with a smooth surface and porous core, to fibers with porous morphologies both at the fiber surface and in the core [9]. The process variables that affect the final fiber

morphologies include: initial polymer concentration, the rate of solvent evaporation relative to that of phase separation, and temperature. As the polymer concentration of the jet falls into the unstable two-phase region, a slower rate of solvent evaporation relative to that of phase separation, together with a low temperature, promote the formation of a porous morphology within the fibers.

Experimental confirmation of electrospun fibers exhibiting a smooth fiber surface and porous interior has not been reported, because such morphologies are easy to overlook by conventional SEM analysis of the fibers, yet will dramatically affect any attempt to rationalize fiber properties. They may be more prevalent than is commonly thought. For these reasons, it is important to understand the conditions under which such morphologies may arise, and how they may be recognized. We studied electrospun fibers formed from solutions of amorphous atactic polystyrene (PS), as well as polyacrylonitrile (PAN), poly(methyl methacrylate) (PMMA), and Cellulose Acetate (CA), dissolved in a commonly used solvent, dimethylformamide (DMF). Remarkably, we found that fibers with a smooth surface and porous interiors, rather than a homogeneous consolidated solid structure, are readily obtained when the system is electrospun in a very humid environment.

## **3.2 Results and Discussion**

### **3.2.1 Observations of Exterior Fiber Structure Before and After Annealing**

A 30 wt% solution of PS ( $M_w = 280$  kg/mol) dissolved in DMF was electrospun in air at 29% relative humidity and room temperature. As shown in Figure 3-1(a), the as-spun PS fibers have a smooth surface and cylindrical shape. The SEM image shows that the average fiber diameter is  $3.52 \pm 0.2$   $\mu\text{m}$ . After annealing, the morphology shown in Figure 3-1(b) is qualitatively similar to that of the as-spun fibers, but the average fiber diameter is  $2.46 \pm 0.2$   $\mu\text{m}$ , significantly smaller than for the as-spun fibers.

Relative humidity in the environment during fiber spinning affects not only the occurrence of a liquid-liquid phase separation into polymer-rich and polymer-poor regions [2-6] but also the rate of solidification of polymer from either the single

phase or polymer-rich regions [11]. The solidification rate of PS fibers electrospun from DMF is faster at high relative humidity because the water absorbing from the air into the jet acts as a nonsolvent for PS. SEM images of as-spun fibers electrospun from 30 wt% PS/DMF solutions under relative humidity ranging from 11 to 43% are shown in Figure 3-2(a). The fibers electrospun at greater than 24% relative humidity have smooth surfaces. Below 24% relative humidity, the smooth surface is replaced by a wrinkled surface, and the fiber diameter tends to be smaller. Table 3-1 lists the average diameters for as-spun fibers obtained at different relative humidities. Below 15% relative humidity, solidification is delayed and the jet undergoes further thinning, and eventually capillary instability sets in, resulting in the beads-on-string fiber morphology; both beads and strings exhibit a wrinkled or collapsed surface morphology. The fiber diameter for beads-on-string structures is hard to estimate, particularly for the fiber obtained at 15% relative humidity, near the transition from uniform wrinkled fibers to beads-on-string structures. The average diameter listed in Table 3-1 merely shows the diameter for strings, not including the beads.

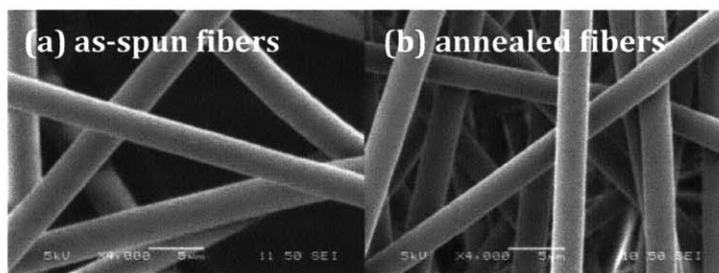


Figure 3-1. SEM images of fibers electrospun from a 30 wt% PS/DMF solution at 29% relative humidity: (a) as-spun fibers and (b) annealed fibers (scale bar: 5  $\mu\text{m}$ ).

Figure 3-2(b) shows SEM images of the same PS fibers as Figure 3-2(a), electrospun from 30 wt% PS/DMF solutions under relative humidity ranging from 11 to 43%, after annealing. It shows the alleviation of the wrinkled surface and the shrinkage of fiber diameters when compared with as-spun fibers. This phenomenon indicates that the elimination of wrinkles might be a surface effect.



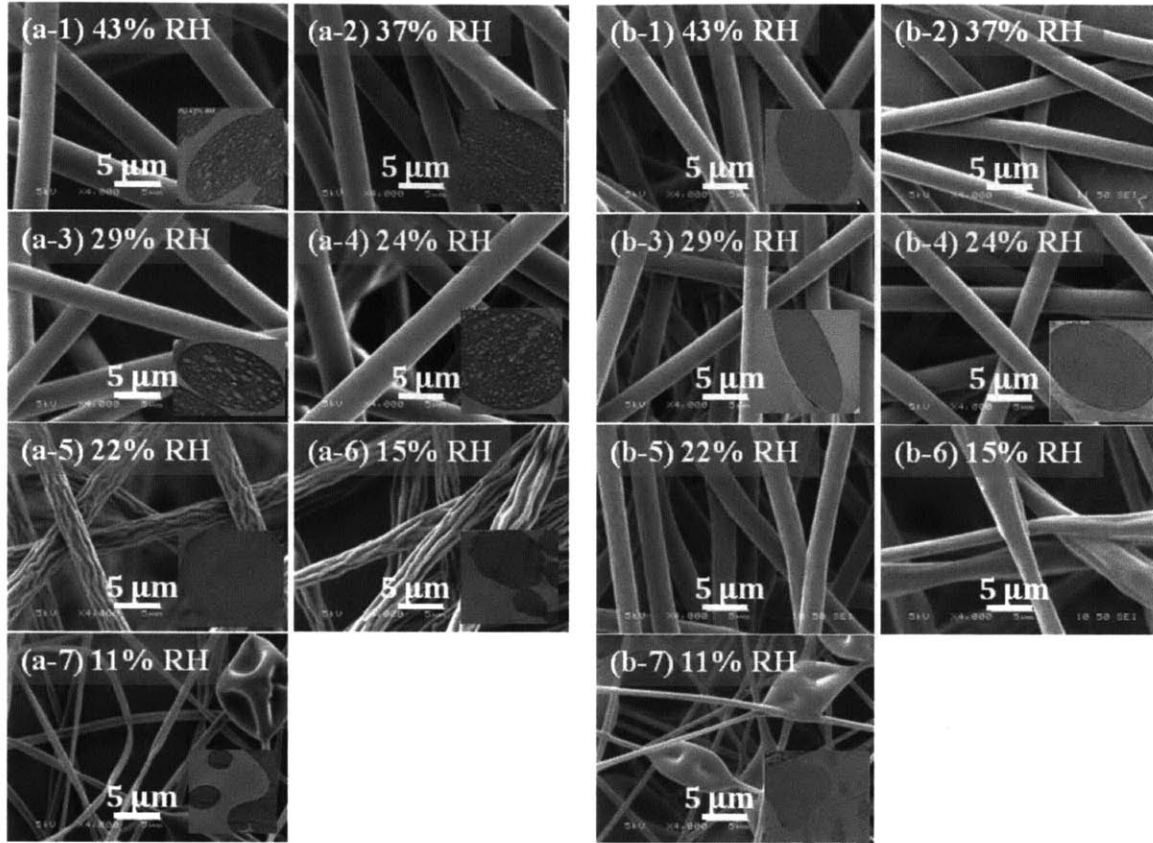


Figure 3-2. SEM images of (a) as-spun fibers and (b) annealed fibers electrospun from a 30 wt% PS/DMF solution under different relative humidity. The insert images are cross-sectional TEM images.

Table 3-1. Diameters of PS Single Fibers

wt%	RH (%)	Diameter of as-spun fibers ( $\mu\text{m}$ )	Diameter of annealed fibers ( $\mu\text{m}$ )	void volume fraction (from the shrinkage of fiber diameter)	void volume fraction (from analysis of TEM)
30	43	3.93 ( $\pm 0.42$ )	2.77 ( $\pm 0.41$ )	0.504	0.293
	37	3.57 ( $\pm 0.32$ )	2.54 ( $\pm 0.29$ )	0.494	0.282
	29	3.52 ( $\pm 0.22$ )	2.46 ( $\pm 0.20$ )	0.512	0.313
	24	4.09 ( $\pm 0.30$ )	2.99 ( $\pm 0.12$ )	0.463	0.286
	22	2.96 <sup>(a)</sup>	2.80 <sup>(a)</sup>	-	-
	15	2.51 <sup>(a)(b)</sup>	1.80 <sup>(a)(b)</sup>	-	-
	11	0.90 ( $\pm 0.08$ ) <sup>(a)(b)</sup>	0.94 ( $\pm 0.19$ ) <sup>(a)(b)</sup>	-	-
10	35	2.06 ( $\pm 0.54$ ) <sup>(a)</sup>	1.69 ( $\pm 0.25$ ) <sup>(a)</sup>	0.328	0.211
	24	1.17 ( $\pm 0.19$ ) <sup>(a)</sup>	1.08 ( $\pm 0.17$ ) <sup>(a)</sup>	0.147	0.111

The parenthesis corresponds to one standard deviation. <sup>(a)</sup> Fibers with wrinkled surface. <sup>(b)</sup> Fibers exhibit beads-on-string morphology.

The origin of wrinkles is likely due to buckling of a cylindrical polymer shell under compressive hoop stresses, arising from removal of solvent from the core of the jet, and/or a lateral contraction effect from the axial tensile stresses, arising from the continuous stretching of the jet. Annealing permits the fibers to reduce their surface energy by smoothing out the wrinkles and, as shown later, also influences the internal morphology.

### **3.2.2 Mechanical Property Evaluation**

Figure 3-3 shows the engineering stress-strain curves for single PS fibers obtained under uniaxial tension. Each curve is averaged over fifteen fibers. Both as-spun and annealed single PS fibers exhibited brittle failure around 2% elongation. However, the average modulus and ultimate tensile strength were observed to be higher for the annealed fibers. The average modulus and ultimate tensile strength are 1.24 GPa and 17 MPa for as-spun fibers, and 3.57 GPa and 49 MPa for annealed fibers. For purposes of comparison, a cast PS film of thickness 74.4 ( $\pm 4.2$ )  $\mu\text{m}$  exhibited average modulus and ultimate tensile strength of 3.63 GPa and 43 MPa after annealing. Literature values for Young's modulus and ultimate tensile strength for bulk PS are around 3.0 to 3.6 GPa and 40 to 60 MPa, respectively [12-13]. Thus, both the annealed fibers and the film exhibit mechanical properties comparable to bulk PS. One possible speculation for the inferior mechanical performance of as-spun single fibers is that some residual solvent was retained in the as-spun fibers, due to the high boiling point (153°C) of DMF. However, thermogravimetric analysis results (not shown) indicated less than 5 % weight loss around the boiling point of DMF, for electrospun mats stored at room temperature for 24 hours prior to the testing. Such a low level of residual DMF would not account for the poorer mechanical properties of the as-spun fibers. An alternative explanation is that the fibers differ in their internal morphologies; this possibility is confirmed by cross-sectional TEM images and examined in the next section.

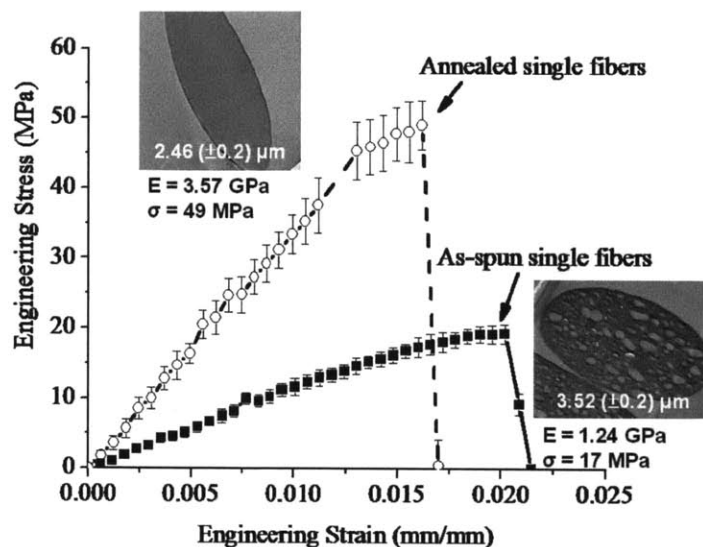


Figure 3-3. Engineering stress-strain curves for single fibers electrospun from a 30 wt% PS/DMF solution at 29% relative humidity. Each datum is averaged over 15 fibers, and error bars correspond to one standard deviation.

### 3.2.3 Observation of Interior Fiber Structure

Figure 3-4(a) shows a cross-sectional TEM image of as-spun PS fibers. The TEM image clearly reveals the presence of large voids within the interior of the fiber. The void volume fraction obtained from image analysis is about 30%; the voids range in diameter from 10 to 300 nm. Analysis of images of numerous fibers indicates that whereas the void volume fraction is relatively constant, the void sizes can vary dramatically from fiber to fiber. Voids of diameters as large as 700 nm were observed in fibers of diameter 3.52  $\mu\text{m}$ . The presence of voids would lower the elastic modulus and strength of the fiber and would serve as points of stress concentration during tensile testing. By contrast, no obviously visible voids are observed in the annealed PS fibers. Note that annealing fibers at a temperature above  $T_g$  resulted in a smooth surface and a consolidated interior; in contrast, annealing fibers at 65°C under vacuum for 24 hours does not eliminate the interior porous structure, as shown in Figure 3-4(b). Therefore, careful annealing of the fibers at a temperature just slightly above the glass transition temperature seems to be an effective way to achieve interior solid structure.

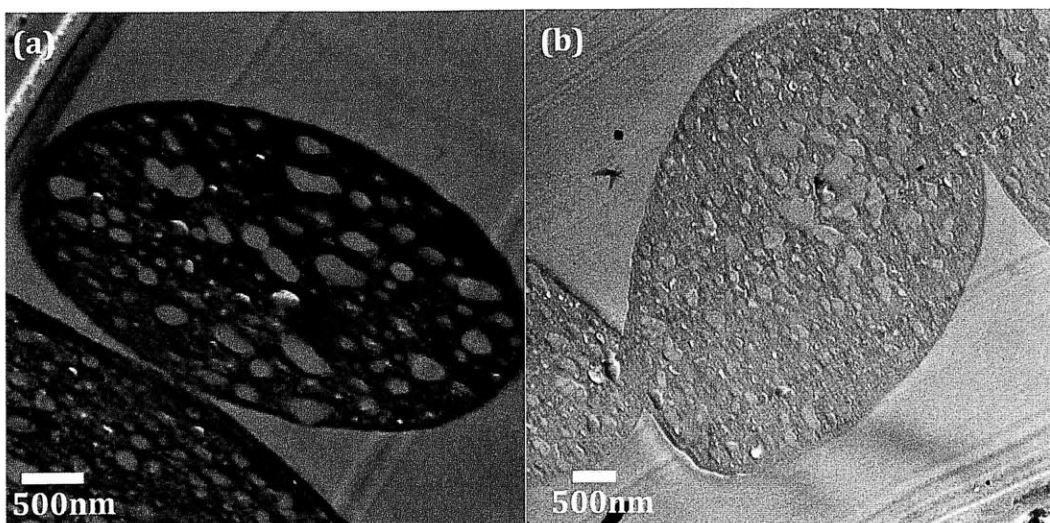


Figure 3-4. (a) The cross-sectional TEM image of as-spun fibers electrospun from a 30 wt% PS/DMF solution at 29% relative humidity and (b) those fibers followed by annealing at 65°C under vacuum for a day (scale bar: 500 nm).

### 3.2.4 Rationalization of Interior and Exterior Structure in terms of Models

The formation of surface pores has been attributed on different occasions to phase separation [2-6] and to “breath figures” resulting from water condensation on the surface of the liquid jet [2-3, 14-16]. Rabolt and coworkers demonstrated that porous surface features on fibers electrospun from low boiling point solvent can be varied by controlling the relative humidity of the surrounding air and the molecular weight of the polymer [2-3]. The dependence of pore size on polymer molecular weight suggests that phase separation is the governing mechanism in this case. A liquid-liquid phase separation occurs via spinodal decomposition and/or nucleation and growth. The polymer-rich phase solidifies and the solvent-rich phase leads ultimately to the formation of pores. During electrospinning, the most relevant phase separation processes are thermally induced phase separation (TIPS), attributed to the rapid evaporation of solvent that lowers the temperature on the fiber surface, and vapor induced phase separation (VIPS) associated with water vapor in the surrounding air that acts as the nonsolvent. In our PS/DMF system, most fibers electrospun from the high boiling point DMF were without surface pores. This finding indicates that TIPS and breath figures are not contributing

mechanisms in our case because the evaporation of DMF is slow compared to a low boiling solvent such as tetrahydrofuran (THF); it is unlikely that one can decrease the temperature on the fiber surface to a value low enough either to bring about TIPS or to condense water. In the PS/DMF system, VIPS may be responsible for the production of porous structures within the fibers. Given the miscibility of water with DMF, the water from the humid environment may be absorbed into the jet and play a role as nonsolvent for PS; VIPS then precedes solidification due to the slow evaporation rate of DMF. To understand this behavior, one needs to consider a ternary composition of H<sub>2</sub>O/DMF/PS in the jet. A ternary phase diagram for H<sub>2</sub>O/DMF/PS was constructed in this study based on the Flory-Huggins theory [17]. The mass transfer of the three components during the fiber formation was then calculated for representative operating conditions, and the resulting mass transfer paths were superposed onto the ternary phase diagram [18-20].

For a ternary mixture, the Gibbs free energy of mixing can be expressed as:

$$\frac{\Delta G_M}{RT} = n_1 \ln \varphi_1 + n_2 \ln \varphi_2 + n_3 \ln \varphi_3 + g_{12}(u_2)n_1\varphi_2 + g_{13}(\varphi_3)n_1\varphi_3 + g_{23}(\varphi_3)n_2\varphi_3 \quad (3-1)$$

Subscripts 1, 2, 3 refer to nonsolvent (H<sub>2</sub>O), solvent (DMF), and polymer (PS).  $R$  is the gas constant and  $T$  is the absolute temperature;  $n_i$  and  $\varphi_i$  are the number of moles and the volume fraction of component  $i$ ;  $g_{ij}$  is the concentration-dependent interaction parameter between component  $i$  and  $j$ .  $g_{12}$  is expressed as a function of  $u_2$ , where  $u_2 = \varphi_2 / (\varphi_1 + \varphi_2)$ , and  $g_{13}$  and  $g_{23}$  are both functions of  $\varphi_3$ .

The chemical potential of component  $i$  is given by  $\mu_i$ , and  $\Delta \mu_i$  is the chemical potential difference between component  $i$  and its pure liquid state at the same temperature [17], where  $\frac{\Delta \mu_i}{RT} = \left( \frac{\partial(\Delta G_M / RT)}{\partial n_i} \right)_{n_{j \neq i}}$ . The chemical potential difference

for each component can be expressed as:

$$\begin{aligned} \frac{\Delta \mu_1}{RT} = & \ln \varphi_1 + 1 - \varphi_1 - \frac{v_1}{v_2} \varphi_2 - \frac{v_1}{v_3} \varphi_3 + (g_{12}\varphi_2 + g_{13}\varphi_3)(\varphi_2 + \varphi_3) \\ & - g_{23} \frac{v_1}{v_2} \varphi_2 \varphi_3 - (1 - u_2)u_2\varphi_2 \left( \frac{dg_{12}}{du_2} \right) - \varphi_1\varphi_3^2 \left( \frac{dg_{13}}{d\varphi_3} \right) - \frac{v_1}{v_2} \varphi_2\varphi_3^2 \left( \frac{dg_{23}}{d\varphi_3} \right) \end{aligned} \quad (3-2)$$

$$\begin{aligned} \frac{\Delta\mu_2}{RT} = & \ln \varphi_2 + 1 - \varphi_2 - \frac{v_2}{v_1} \varphi_1 - \frac{v_2}{v_3} \varphi_3 + \left( g_{12} \frac{v_2}{v_1} \varphi_1 + g_{23} \varphi_3 \right) (\varphi_1 + \varphi_3) \\ & - g_{13} \frac{v_2}{v_1} \varphi_1 \varphi_3 + (1 - u_2) u_2 \frac{v_2}{v_1} \varphi_1 \left( \frac{dg_{12}}{du_2} \right) - \frac{v_2}{v_1} \varphi_1 \varphi_3^2 \left( \frac{dg_{13}}{d\varphi_3} \right) - \varphi_2 \varphi_3^2 \left( \frac{dg_{23}}{d\varphi_3} \right) \end{aligned} \quad (3-3)$$

$$\begin{aligned} \frac{\Delta\mu_3}{RT} = & \ln \varphi_3 + 1 - \varphi_3 - \frac{v_3}{v_1} \varphi_1 - \frac{v_3}{v_2} \varphi_2 + \left( g_{13} \frac{v_3}{v_1} \varphi_1 + g_{23} \frac{v_3}{v_2} \varphi_2 \right) (\varphi_1 + \varphi_2) \\ & - g_{12} \frac{v_3}{v_1} \varphi_1 \varphi_2 + \left[ \frac{v_3}{v_1} \varphi_1 \left( \frac{dg_{13}}{d\varphi_3} \right) + \frac{v_3}{v_2} \varphi_2 \left( \frac{dg_{23}}{d\varphi_3} \right) \right] \varphi_3 (\varphi_1 + \varphi_2) \end{aligned} \quad (3-4)$$

The binodal curve can be calculated from the equality of the chemical potential between the polymer-rich (A) and polymer-lean (B) phases.

$$\Delta\mu_{i,A} = \Delta\mu_{i,B} \quad (i = 1, 2, 3) \quad (3-5)$$

The spinodal curve can be calculated from the following equation [21]:

$$G_{22}G_{33} = (G_{23})^2 \quad (3-6)$$

where  $G_{ij} = \left( \frac{\partial^2 \overline{\Delta G_M}}{\partial \varphi_i \partial \varphi_j} \right)_{v_{ref}}$ ,  $\overline{\Delta G_M}$  is the Gibbs free energy of mixing per unit volume,

and  $v_{ref}$  is the molar volume of the reference component, which is component 1 in this study.

An expression for  $g_{12}$  for the water/DMF system was reported by Altena et al. [22]:

$$g_{12}(u_2) = 0.50 + 0.04u_2 + 0.8u_2^2 - 1.20u_2^3 + 0.8u_2^4 \quad (3-7)$$

Following the studies of Matsuyama et al. and Yip et al., we assumed constant values for  $g_{13}$  and  $g_{23}$  in our work [19-20]. The solvent-polymer interaction parameter  $g_{23}$  for DMF/PS can be roughly estimated by [23]:

$$g_{23} = 0.34 + \frac{v_2(\delta_2 - \delta_3)^2}{RT} \quad (3-8)$$

where  $\delta_i$  is the solubility parameter for component  $i$  ( $\delta_{DMF} = 24.8$  (MPa)<sup>1/2</sup> and  $\delta_{PS} = 22.49$  (MPa)<sup>1/2</sup>) [23-24]. The calculated value of  $g_{23} = 0.506$  is similar to the experimental data ( $g_{23} = 0.497$ ) from Wolf et al. [25]. The latter was used here. The nonsolvent-polymer interaction parameter  $g_{13}$  is generally estimated from the

swelling experiment; however, no experimental data for an H<sub>2</sub>O/PS system could be found in the literature. Therefore,  $g_{13}$  was treated as a fitting parameter in our study. It was found that the calculated binodal curve fits the cloud point curve well by setting  $g_{13} = 2.2$ , as shown in Figure 3-5. The parameters used to construct the ternary phase diagram for H<sub>2</sub>O/DMF/PS system are listed in Table 3-2.

To determine mass transfer pathways, radial diffusion within a fiber with negligible end effects was modeled; the geometry for the system is shown in Figure 3-6. The diffusion equations are:

$$\frac{\partial \varphi_1}{\partial t} = \frac{1}{r} \frac{\partial}{\partial r} \left( rD_{11} \frac{\partial \varphi_1}{\partial r} + rD_{12} \frac{V_1}{V_2} \frac{\partial \varphi_2}{\partial r} \right) \quad (3-9)$$

$$\frac{\partial \varphi_2}{\partial t} = \frac{1}{r} \frac{\partial}{\partial r} \left( rD_{21} \frac{V_2}{V_1} \frac{\partial \varphi_1}{\partial r} + rD_{22} \frac{\partial \varphi_2}{\partial r} \right) \quad (3-10)$$

where  $D_{ij}$  is the appropriate phenomenological diffusion coefficient;  $r$  is the radial direction in cylindrical coordinates;  $V_i$  is the partial specific volume of component  $i$  in the fiber. Because  $\varphi_1$  is much smaller than  $\varphi_2$ , the quasi-binary system was substituted for Equation (3-10), giving:

$$\frac{\partial \varphi_2}{\partial t} = \frac{1}{r} \frac{\partial}{\partial r} \left( rD_2 \frac{\partial \varphi_2}{\partial r} \right) \quad (3-10')$$

where  $D_2$  is the mutual diffusion coefficient of the solvent in the binary system.

Initial conditions and boundary conditions for Equations (3-9) and (3-10') are:

$$t = 0 \quad \varphi_1 = \varphi_{10}, \varphi_2 = \varphi_{20} \quad (3-11)$$

$$r = 0 \quad \frac{\partial \varphi_1}{\partial r} = \frac{\partial \varphi_2}{\partial r} = 0 \quad (3-12)$$

$$\begin{aligned} r = R(t) \quad & -D_{11} \frac{\partial \varphi_1}{\partial r} - D_{12} \frac{V_1}{V_2} \frac{\partial \varphi_2}{\partial r} = k_1 V_1 (\rho_{1g}^i - \rho_{1g}^{\text{inf}}) \\ & -D_2 \frac{\partial \varphi_2}{\partial r} = k_2 V_2 (\rho_{2g}^i - \rho_{2g}^{\text{inf}}) \end{aligned} \quad (3-13)$$

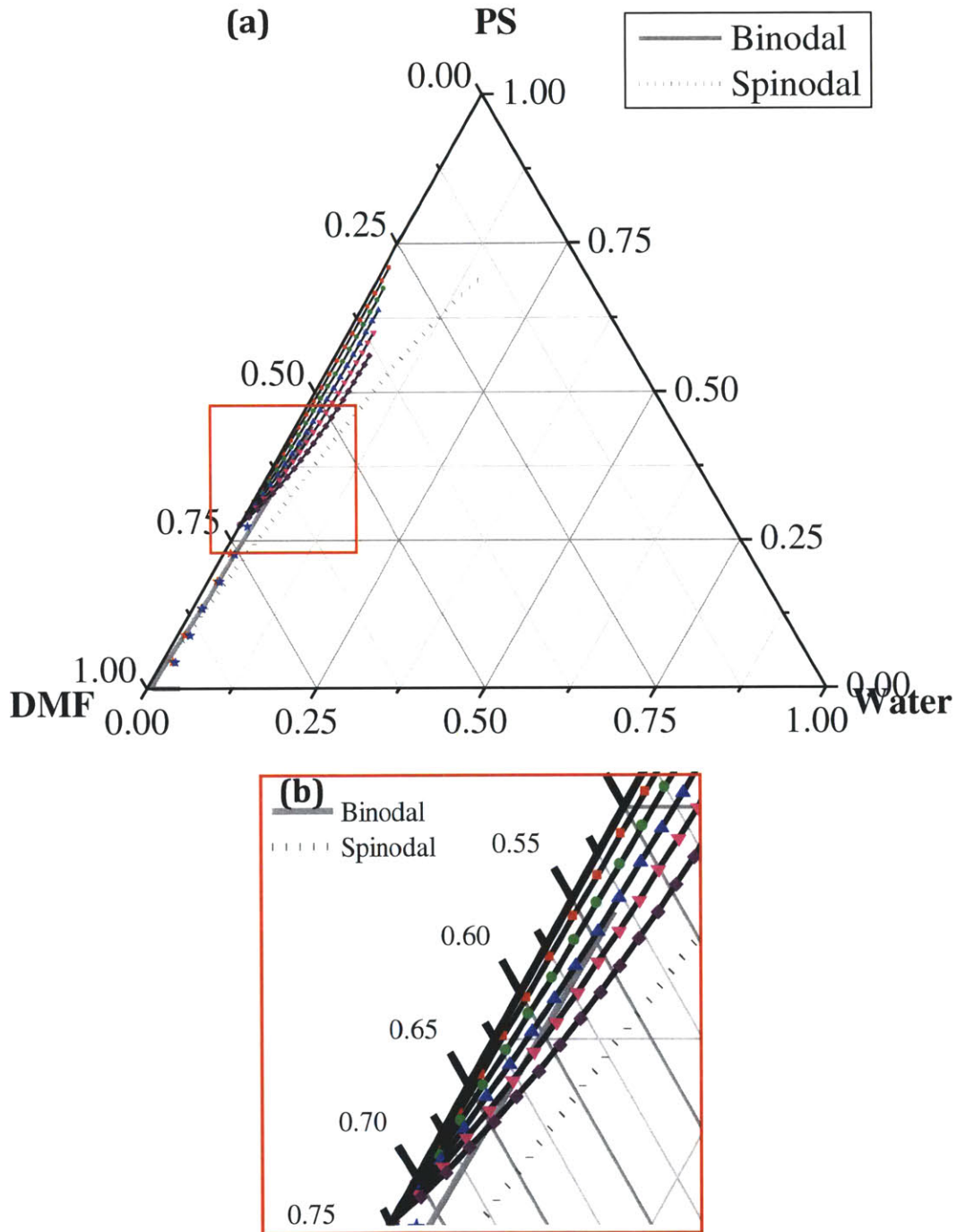


Figure 3-5. (a) Ternary phase diagram for the three component system, and (b) the enlarged region of the red window in (a). Experimental data: (red star symbol: before observed cloud point, and blue star symbol: after observed cloud point). Theoretical binodal (solid gray curve) and spinodal (dotted curve). Theoretical mass transfer paths for 30 wt% PS/DMF solutions ( $\blacksquare$ : 10%,  $\bullet$ : 20%,  $\blacktriangle$ : 30%,  $\blacktriangledown$ : 40%, and  $\blacklozenge$ : 50% relative humidity). Each data point represents an interval of 0.05 second.



Table 3-2. Parameters Used to Construct the Ternary Phase Diagram

$v_1$ (cm <sup>3</sup> /mol)	18.0
$v_2$ (cm <sup>3</sup> /mol)	77.4
$v_3$ (cm <sup>3</sup> /mol)	266667
$g_{13}$	2.2
$g_{23}$	0.497

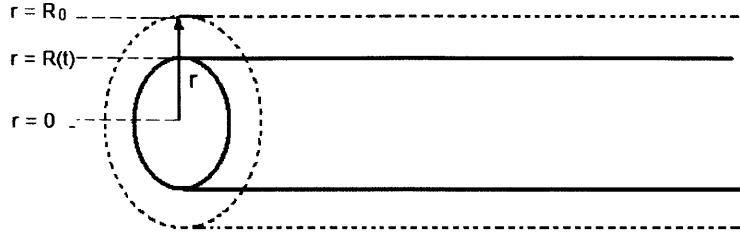


Figure 3-6. Geometry for the mass transfer calculation.

The subscript  $0$  refers to the initial condition.  $R(t)$  is the fiber radius at time  $t$ ;  $k_i$  is the gas-side mass transfer coefficient of component  $i$ ;  $\rho_{ig}$  is the mass density of component  $i$  in the gas phase. Superscripts  $i$  and  $inf$  refer to the air-fiber interface and in the bulk gas phase. Because this is a moving boundary problem,  $\eta$  was defined here to simplify the problem and facilitate the calculation by finite differences:

$$\eta = \frac{r}{R(t)} \quad (3-14)$$

Also, due to the difficulties of direct stability analysis [18], diffusion coefficients were assumed to be independent of  $\eta$ . In this form, the diffusion equations, initial conditions and boundary conditions are:

$$\left( \frac{\partial \varphi_1}{\partial t} \right)_\eta = \frac{\eta}{R(t)} \frac{dR(t)}{dt} \frac{\partial \varphi_1}{\partial \eta} + \frac{D_{11}}{\eta R(t)^2} \frac{\partial \varphi_1}{\partial \eta} + \frac{D_{12}}{\eta R(t)^2} \frac{V_1}{V_2} \frac{\partial \varphi_2}{\partial \eta} + \frac{D_{11}}{R(t)^2} \frac{\partial^2 \varphi_1}{\partial \eta^2} + \frac{D_{12}}{R(t)^2} \frac{V_1}{V_2} \frac{\partial^2 \varphi_2}{\partial \eta^2} \quad (3-15)$$

$$\left( \frac{\partial \varphi_2}{\partial t} \right)_\eta = \frac{\eta}{R(t)} \frac{dR(t)}{dt} \frac{\partial \varphi_2}{\partial \eta} + \frac{D_2}{\eta R(t)^2} \frac{\partial \varphi_2}{\partial \eta} + \frac{D_2}{R(t)^2} \frac{\partial^2 \varphi_2}{\partial \eta^2} \quad (3-16)$$

$$t = 0 \quad \varphi_1 = \varphi_{10}, \varphi_2 = \varphi_{20} \quad (3-17)$$

$$\eta = 0 \quad \frac{\partial \varphi_1}{\partial \eta} = \frac{\partial \varphi_2}{\partial \eta} = 0 \quad (3-18)$$

$$\eta = 1 \quad -D_{11} \frac{\partial \phi_1}{\partial \eta} - D_{12} \frac{V_1}{V_2} \frac{\partial \phi_2}{\partial \eta} = k_1 R(t) V_1 (\rho_{1g}^i - \rho_{1g}^{inf}) \quad (3-19)$$

$$-D_2 \frac{\partial \phi_2}{\partial \eta} = k_2 R(t) V_2 (\rho_{2g}^i - \rho_{2g}^{inf})$$

$$R(t) = \left( \frac{\pi R_0^2 \phi_{30}}{\int_0^1 2\pi \eta \phi_3 d\eta} \right)^{1/2} \quad (3-20)$$

The equations for determining the diffusion coefficients and mass transfer coefficients are listed in the Appendix V. Finite differences for one dimensional and time dependent partial differential Equations (3-15) and (3-16) were performed using Matlab (R2008a, The Mathworks Inc., USA), and the Matlab codes are listed in the Appendix II and Appendix III. All the parameters used for the mass transfer calculation are listed in Table 3-3.

Figure 3-5 shows the calculated ternary phase diagram for our system and the mass transfer paths for 30 wt% PS/DMF solutions jetted under conditions of different relative humidity. Once the water was transported into the system, phase separation occurred almost instantly (within 1 second) for high relative humidity, ranging from 30% (0.57 second) to 50% (0.18 second). It is apparent from Figure 3-5 that, at low relative humidity (10% and 20%), it was relatively hard to induce phase separation. Note that DMF is a very common solvent used to dissolve various polymers for use in electrospinning; therefore, it is perhaps not surprising that several authors have noted the sensitivity of fiber formation to the relative humidity of the surrounding air [26-27]. The possible porous structure within as-spun fibers can be the result of water vapor in the environment acting as nonsolvent. In order to obtain homogeneous solid fibers, careful consideration should be paid to the proper selection of solvent, the environmental factors, and the need of post-spinning heat treatment.

The insert TEM images in Figure 3-2(a) show cross sections of as-spun fibers electrospun from a 30 wt% PS/DMF solution at different relative humidities. Obvious porous structures within the fiber were observed for fibers electrospun from high relative humidity ranging from 24 to 43%. For as-spun fibers obtained at

low relative humidity, having wrinkled or collapsed structures, only a few, small voids were observed in Figure 3-2(a-5) through (a-7). Note that the larger cross section of the fiber in Figure 3-2(a-6) and (a-7) corresponds to the beads, and the smaller cross sections correspond to the strings.

Table 3-3. Parameters Used in Mass Transfer Calculation

$w_{10}$	$10^{-20}$	$M_1$ (g/mol)	18	$R$ (erg/mol/K)	$8.314 \times 10^7$
$w_{20}$	0.7	$M_2$ (g/mol)	73.09	$T$ (K)	300
$w_{30}$	0.3	$M_3$ (g/mol)	280000	$N_A$	$6.022 \times 10^{23}$
$\rho_1$ (g/cm <sup>3</sup> )	1.00	$K_{22}/\gamma$ (cm <sup>3</sup> /g/K)	$9.76 \times 10^{-4}$	$R_0$ (cm)	$5 \times 10^{-4}$
$\rho_2$ (g/cm <sup>3</sup> )	0.94	$K_{32}-T_{g2}$ (K)	-43.8	$\xi$ (-)	0.47
$\rho_3$ (g/cm <sup>3</sup> )	1.05	$K_{23}/\gamma$ (cm <sup>3</sup> /g/K)	$5.82 \times 10^{-4}$	$D_{20}$ (cm <sup>2</sup> /s)	$8.48 \times 10^{-4}$
$V_1$ (cm <sup>3</sup> /g)	1.00	$K_{33}-T_{g23}$ (K)	-327	$D^{12}(\phi_1=1)$ (cm <sup>2</sup> /s)	$1.12 \times 10^{-5}$
$V_2$ (cm <sup>3</sup> /g)	1.06	$P_1^0$ (atm)	0.0313	$D_{1g}$ (cm <sup>2</sup> /s)	0.267
$V_3$ (cm <sup>3</sup> /g)	0.95	$P_2^0$ (atm)	$4.79 \times 10^{-3}$	$D_{2g}$ (cm <sup>2</sup> /s)	0.023
$V_2^*$ (cm <sup>3</sup> /g)	0.926	$P_t$ (atm)	1	$\mu_g$ (g/cm/s)	$1.85 \times 10^{-4}$
$V_3^*$ (cm <sup>3</sup> /g)	0.850	$\rho_{1g}^{inf}$ (g/cm <sup>3</sup> )	Humidity <sup>(a)</sup>	$\rho_g$ (g/cm <sup>3</sup> )	$1.18 \times 10^{-3}$
$V_{1g}$ (cm <sup>3</sup> /g)	1358	$\rho_{2g}^{inf}$ (g/cm <sup>3</sup> )	$10^{-20}$	$\tau_1^d$ (-)	0.413
$V_{2g}$ (cm <sup>3</sup> /g)	335	$D_c$ (cm)	$10 \times 10^{-4}$	$\tau_2^d$ (-)	-1.65

(a)  $\rho_{1g}^{inf} = 2.715 \times 10^{-5} \times (RH) \text{ g/cm}^3$

Our calculated results for the ternary phase diagram and the mass transfer path predict the occurrence of phase separation within the fibers for different relative humidities in this experiment. The insert TEM images in Figure 3-2(b) show the elimination of interior voids within the annealed PS fibers. Both are probably driven by the thermodynamic tendency to eliminate high energy surfaces. It is interesting to observe that the void volume fraction is far less for the slightly collapsed fiber with wrinkled surface and severely collapsed fiber with ribbon-like morphology than those circular and smooth fibers. In order to understand this phenomenon, the reason why these wrinkled and collapsed fiber structures were formed should also be understood; this is discussed next.

### 3.2.5 Fiber Morphological Evolution

Khoombungse et al. [28] have reported that electrospun fibers with typical diameters larger than 1  $\mu\text{m}$  can adopt a variety of cross-sectional shapes, including flat ribbons and wrinkled surfaces. They postulated that the thin skin layer initially formed on polymer fibers as the solvent evaporates tends to collapse under atmospheric pressure. This is a well-known buckling instability [29-30]. Pauchard et al. [31-33] have also observed such a phenomenon for evaporation of solvent from a sessile drop of polymer solution. Once the buckling instability occurs, complex spatial and temporal evolutions lead to unexpected collapsed shapes of the drops, which are qualitatively similar to the collapsed electrospun fiber, in particular, the beads. The key to understanding this buckling instability is the formation of a glassy skin on the drop (or fiber) surface. In their analysis, Pauchard et al. [31] identified two characteristic times, the drying time  $t_D$  and the buckling time  $t_B$ , and give an order of magnitude description of both:

$$t_D = \frac{V_0}{S_0 W_{E0}} = \frac{R_0}{2W_{E0}} \quad (3-21)$$

$$t_B = \frac{D_2(\varphi_{pg} - \varphi_{p0})^2}{W_{E0}^2} \quad (3-22)$$

where  $V_0$  is the initial volume;  $S_0$  is the initial vapor/drop surface area;  $R_0$  is the initial radius of the fiber;  $W_{E0}$  is the initial evaporation rate;  $D_2$  is the mutual diffusion coefficient for the solvent-polymer system;  $\varphi_{pg}$  is the polymer volume fraction at the drop surface undergoing vitrification; and  $\varphi_{p0}$  is the polymer volume fraction in the core of the drop. According to Pauchard et al., if  $t_B$  is smaller than  $t_D$ , the buckling instability may be observed. The general idea of these two characteristic times,  $t_B$  and  $t_D$ , can be used here to predict the trend whether the fibers will collapse or not under certain conditions, for instance, different evaporation rates or solidification rates, polymer concentrations, or molecular weights of the polymer.

Figure 3-7 shows the proposed fiber cross sections for morphological evolution of the structures. These can be classified into two groups: one without

phase separation (in which the polymer solidifies into a surface skin layer), and the other with phase separation (within the fibers, leading to a porous network interior). For the first four morphologies in Figure 3-7(a) through (d), no phase separation occurs. For example, PS/DMF solutions electrospun at extremely low relative humidity experience little absorption of water from the vapor into the system, so that liquid-liquid phase separation from VIPS is unimportant. Another example is from the work done by Rabolt and coworkers [2-3]. In their PS/THF system, all of the fibers have a collapsed ribbon-like shape because the evaporation of THF precedes the diffusion of water from the vapor into the fiber. Therefore, only the characteristic times of  $t_B$  and the drying time  $t_D$  should be considered here. If  $t_B$  is larger than  $t_D$ , the morphology should resemble that shown in Figure 3-7(a). If  $t_B$  is smaller than  $t_D$ , the morphology should resemble that shown in Figure 3-7(d). If  $t_B$  is comparable to  $t_D$ , the morphology falls between Figure 3-7(b) and (c). The difference between (b), (c) and (d) depends on the mode number of the dominant buckling instability around the fiber circumference [30].

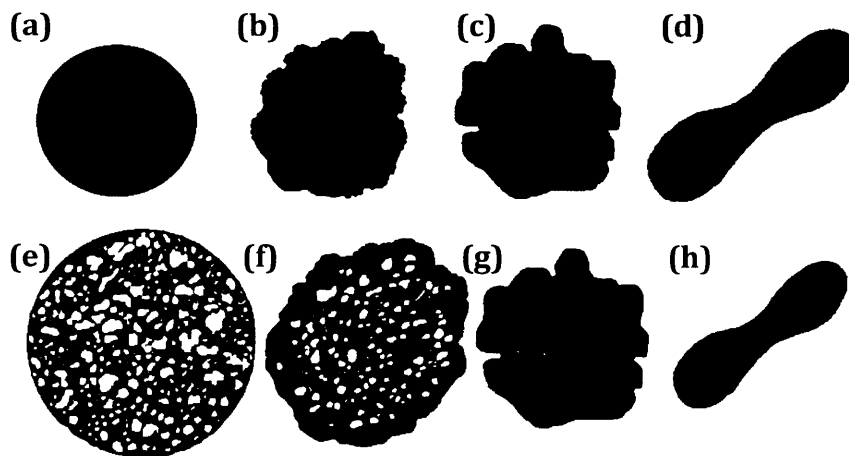


Figure 3-7. Proposed fiber cross sections for morphology evolution. Two groups: one without phase separation, from (a) through (d); and the other with phase separation, from (e) through (h).

The determination of the dominant mode number depends on the skin thickness and Young's modulus as well as the Young's modulus of the internal core and the

radius of the fiber; the skin thickness in turn depends on how much skin forms prior to buckling and is related to the ratio  $t_B/t_D$ . Many factors influence the magnitudes of  $t_B$  and  $t_D$ . Generally, larger fibers tend to collapse due to the longer drying time that accompanies the reduced surface area for evaporation of solvent; polymer solution made from higher molecular weight polymer tends to collapse due to the shorter buckling time that results from a smaller mutual diffusion coefficient; and polymer solution of larger concentration tends to collapse due to the smaller difference between the polymer concentration at the fiber surface and in the core of the fiber.

However, in our PS/DMF system, the fiber morphology evolution is closer to those shown in Figures 3-8(e) through (h). As mentioned before, water vapor acts like a nonsolvent for PS and it is miscible with DMF. Here, the phase separation rate is faster than the evaporation rate of the high boiling DMF, and it helps to alleviate the occurrence of buckling, especially when electrospinning is performed under a very humid environment. With the uptake of water from the vapor as a nonsolvent for the polymer, the thin skin formed on the fiber surface does not collapse as easily as the one without the phase separation. Therefore, besides the characteristic times for  $t_B$  and  $t_D$ , another characteristic time should be considered here, which is the characteristic time for phase separation,  $t_{PS}$ . For that reason, by controlling the nature of the operating environment, such as the relative humidity, and the fluid properties, such as polymer-solvent interaction, combined with the concentration of polymer and the molecular weight of polymer, the morphology can be manipulated between Figures 3-7(e) through (h). Note that the void volume fraction and void size differ with different levels of the collapse. The maximum void volume fraction that can be sustained inside the fiber should be a function of the material stiffness.

Table 3-4 shows rough estimates of the time for phase separation (based on the time to reach the intersection of the operating pathway and the binodal in Figure 8), the drying time (from Equation (3-21)), and the buckling time (from Equation (3-22)) in our system.  $R_0$  was roughly estimated to be 5  $\mu\text{m}$ , derived from the observed as-spun fiber diameter and the original concentration of polymer in solution. Note the value of  $\varphi_{pg}$  was unknown and had to be assumed here; the buckling time varies

significantly with changes of  $\varphi_{pg}$ . A value for  $\varphi_{pg}$  of 0.78 performs reasonably well to describe our observations, but further investigation should be done in the future.

Table 3-4. Comparison for Different Time Scale

RH (%)	$W_{E0}$ ( $\mu\text{m/s}$ )	Time for phase separation, $t_{ps}$ (s)	Drying time from Equation (3-21), $t_D$ (s)	Buckling time from Equation (3-22), $t_B$ (s)
10	3.228	N/A	0.774	0.490
20	3.016	N/A	0.829	0.561
30	2.774	0.57	0.901	0.663
40	2.510	0.28	0.996	0.810
50	2.227	0.18	1.123	1.029

\*  $D_2$  ( $2 \times 10^{-7} \text{ cm}^2/\text{s}$ ),  $W_{E0}$ , and  $t_{ps}$  were obtained from the mass transfer calculation.

The competition among the phase separation ( $t_{ps}$ ), the solvent evaporation ( $t_D$ ), and a buckling instability ( $t_B$ ) is shown in Figure 3-8. The ratio of three characteristic times was plotted as the transverse axle ( $t_D/t_B$ ), the vertical axle ( $t_{ps}/t_B$ ), and the diagonal ( $t_{ps}/t_D$ ), which separate the diagram in Figure 3-8 into four regions. Each region represents a topography and structure of the fiber and is bounded by two conditions. For example, the smooth, solid fiber can be achieved if  $t_{ps}/t_D > 1$  and  $t_D/t_B < 1$ . In our calculation listed in Table 3-4,  $t_{ps}/t_B < 1$  and  $t_{ps}/t_D < 1$  indicates the smooth appearance of fibers electrospun from high relative humidity (from 30 to 50%) because phase separation precedes buckling instability, giving rise to an interior pore network that prevents buckling. For  $t_{ps}/t_B > 1$  and  $t_{ps}/t_D > 1$ , the competition between buckling and drying dominates the resulting morphology. Under these circumstances,  $t_D/t_B > 1$  (applicable to all the cases observed in this work) indicates the formation of a wrinkled surface, consistent with the observed morphology of fibers electrospun from low relative humidity (10% and 20%), because the buckling instability precedes both phase separation and solvent drying. The time scales for the phase separation, solvent drying, and buckling instability in our system are very similar and fall between 0.18 to 1.12 seconds for these three characteristic times, as listed in Table 3-4.

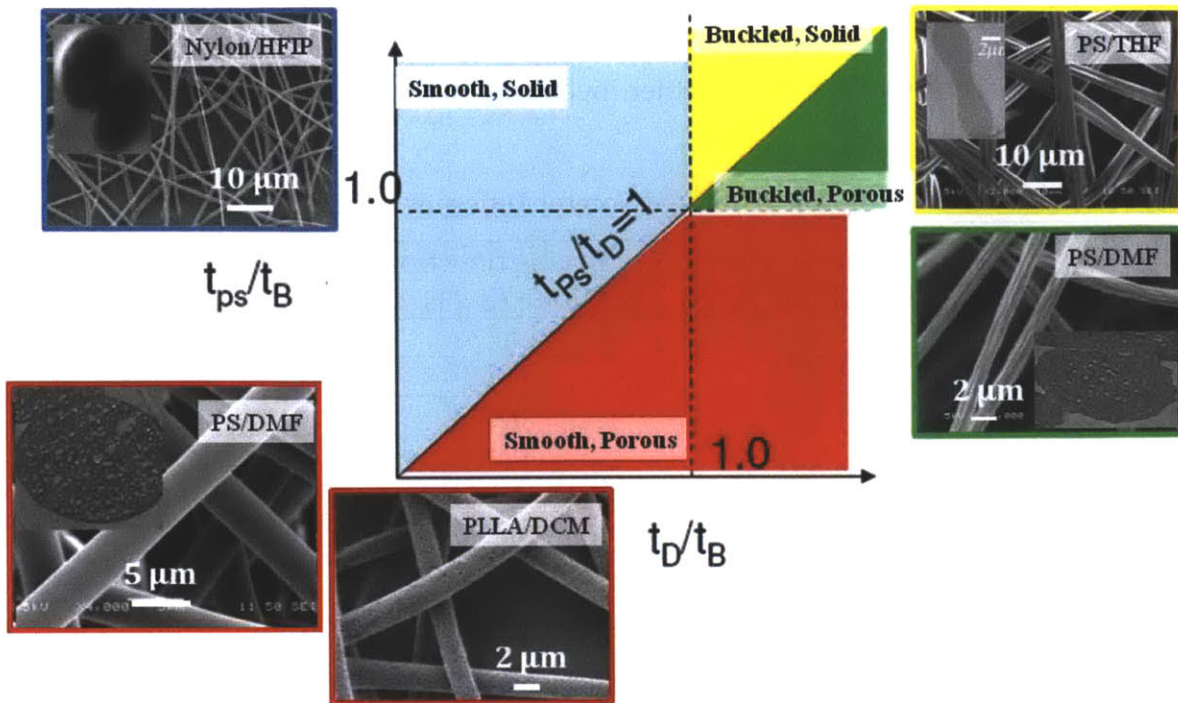


Figure 3-8. The competition among the phase separation, the solvent evaporation, and a buckling instability.

In order to demonstrate further the occurrence of buckling instability, a 10 wt% solution of higher molecular weight PS ( $M_w = 2000 \text{ kg/mol}$ ) dissolved in DMF was electrospun at room temperature and at both 35% and 24% relative humidity. SEM images in Figure 3-9 show the surface wrinkled morphology of as-spun and annealed fibers. Compared with the fibers shown in Figure 3-2 obtained at the same relative humidities, the collapsed structures are apparently obtained more readily for the fibers made from the polymer with high molecular weight. This accords with Equation (3-22). Since  $D_2$  decreases with increasing molecular weight,  $t_B$  is shorter and the buckling instability is favored. Figure 3-9 also shows TEM cross section images of as-spun and annealed fibers. Porous structures within the fiber were observed, but with less void volume fraction for the as-spun fiber due to the collapsed structures.



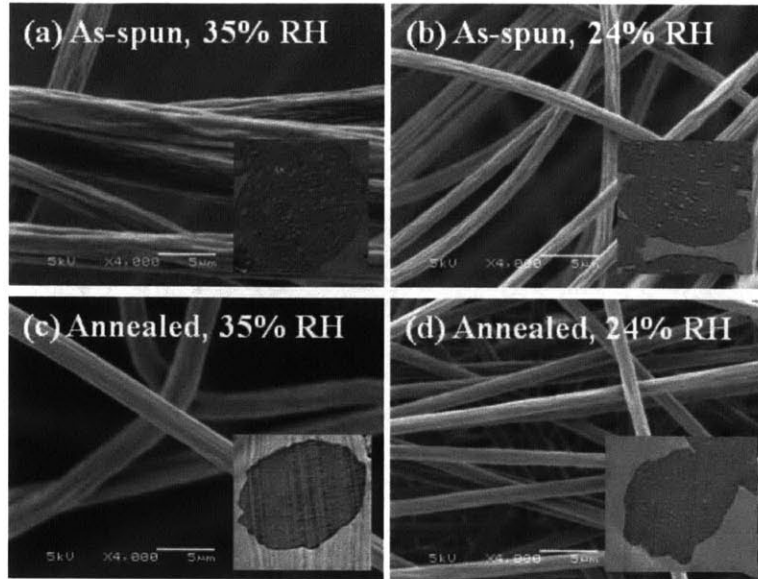


Figure 3-9. SEM images of as-spun fibers electrospun from a 10 wt% PS/DMF solution under (a) 35% and (b) 24% relative humidity, and annealed ones from (c) 35% and (d) 24% relative humidity (scale bar: 5  $\mu\text{m}$ ). The insert images are cross-sectional TEM images.

### 3.2.6 Other Polymer System: PAN/DMF.

Polyacrylonitrile (PAN,  $M_w=150$  kg/mol) is a semicrystalline polymer with a glass transition temperature around  $125^\circ\text{C}$ . It is commonly used as a precursor for making carbon fibers [34]. Electrospun PAN fibers are usually processed from DMF solutions [34-40]. We electrospun PAN fibers from solutions of 9 ~ 14 wt% polymer in DMF, as shown in Figure 3-10. The average diameter of these fibers from different polymer concentrations ranges from 0.60  $\mu\text{m}$  to 1.86  $\mu\text{m}$ . As evidence for the generality of these phenomena mentioned above, we report qualitatively similar behavior for the PAN/DMF system, especially for fibers electrospun from a 14 wt% PAN/DMF solution.

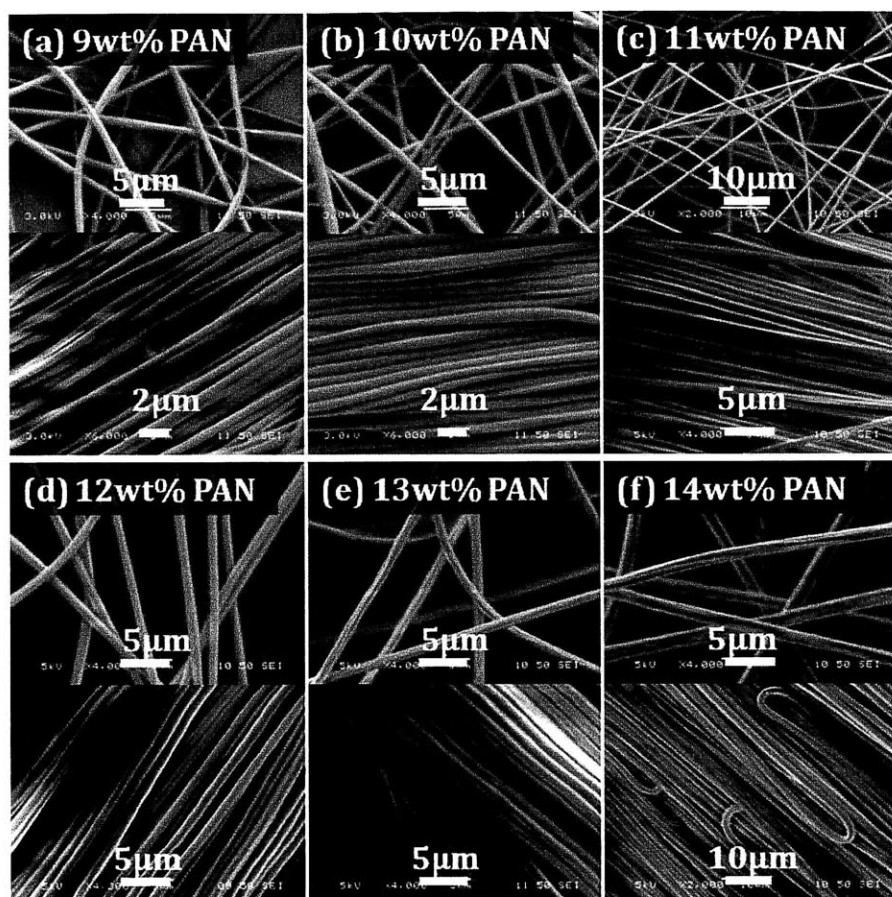


Figure 3-10. SEM images of randomly distributed as-spun nonwoven fabrics and aligned as-spun mats (the fibers were first electrospun into water and then collected on a rotating drum) electrospun from 9-14 wt% PAN/DMF solution.

As shown in Figure 3-11, processing at the higher relative humidity (or lower polymer concentration) produces smooth fibers, whose diameters decrease upon annealing. At the lower relative humidity and higher polymer concentration, wrinkled fibers are found, indicative of the buckling instability. These trends are consistent with those observed for the PS/DMF system. In this case, the void sizes in the porous fibers are smaller than in the PS/DMF system and harder to quantify, and changes in properties upon annealing are further complicated by the semicrystalline nature of PAN. According to the TEM image analysis, the void volume fraction is around 0.4, and the void diameter is about 20 nm for as-spun fibers electrospun from a 14 wt% PAN/DMF solution under 46% relative humidity, as shown in Figure 3-11(a). With the heat treatment to those fibers at 135°C for 2

hours, the annealed fibers shrank and had a smaller fraction of voids, as shown in Figure 3-11 (c). As shown in Figures 3-11(b) and (d), the PAN fibers electrospun from 14 wt% PAN/DMF at lower relative humidity (31%) exhibited in an interesting wrinkled shape. However, in Figure 3-12, fibers electrospun from lower polymer concentration, a 11 wt% PAN/DMF solution under 31% relative humidity did not collapse. This phenomenon can be explained by the competition among the phase separation, the fiber solidification, and a buckling instability, as discussed earlier. Note that porous structures can exist within small fibers with the diameter less than 1  $\mu\text{m}$ , as shown in Figure 3-12. We can demonstrate porous fibers electrospun from DMF in other polymer systems, such as PMMA and CA, as shown in Figure 3-13.

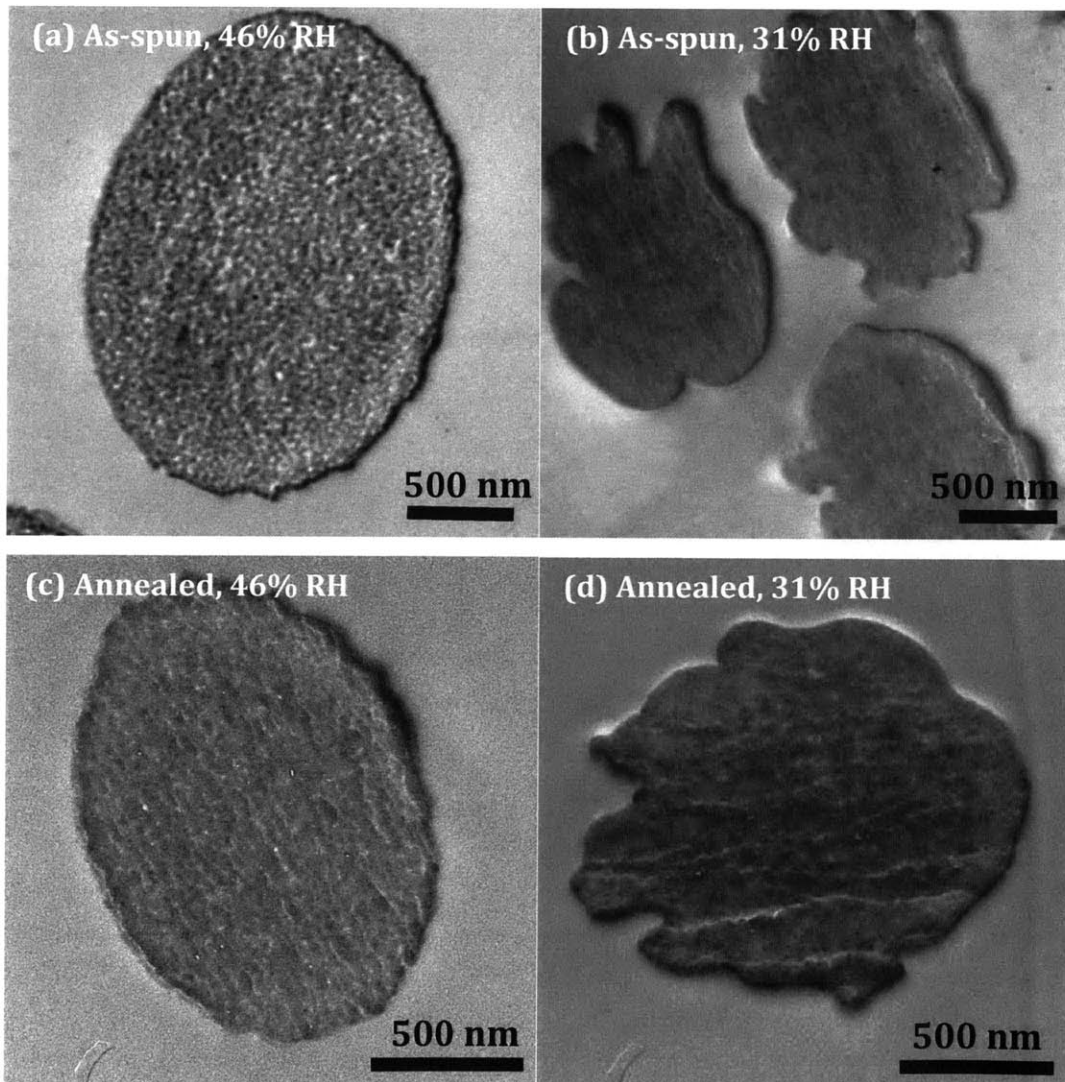


Figure 3-11. Cross-sectional TEM images of as-spun fibers electrospun from a 14 wt% PAN/DMF solution under (a) 46% and (b) 31% relative humidity, and annealed ones from (c) 46% and (d) 31% relative humidity.

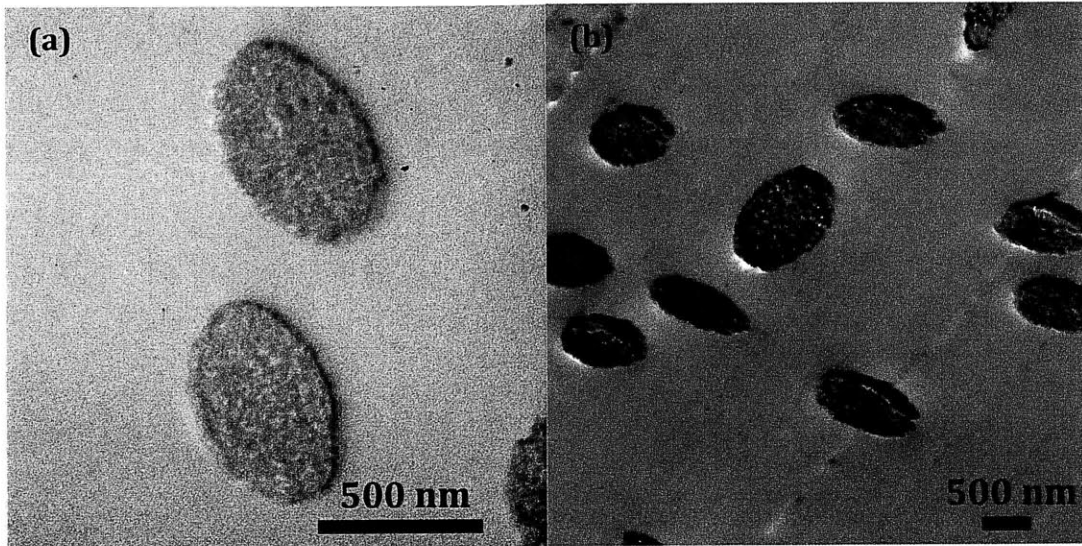


Figure 3-12. The cross-sectional TEM image of as-spun fibers electrospun from (a) a 9% PAN/DMF and (b) a 11 wt% PAN/DMF solution under 31% relative humidity.

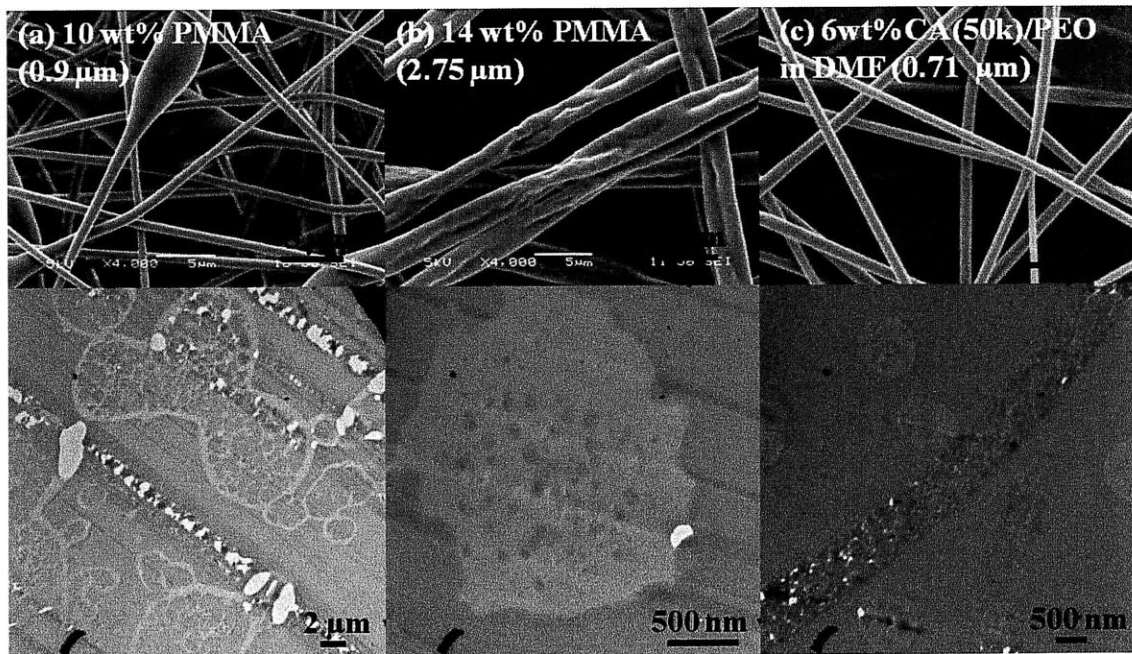


Figure 3-13. Other polymer systems producing porous fibers electrospun from DMF: PMMA and CA.

### 3.2.7 Explanation for Mechanical Behavior of Fibers with Voids

Three different theoretical models [41-48]: Mori-Tanaka, 2D honeycomb, and 3D open cell, are used here to understand the variation of the modulus of the single fiber with the void volume fraction. Mori-Tanaka theory [41-45] is a micromechanical model for the composite fiber, in which the glassy polymer is the matrix and the random voids comprise the dispersed phase. This model has been used by Benveniste [42] to describe the porosity dependence of the elastic modulus:

$$E \equiv 2\mu\mathbf{I}^{4x} + (\kappa - \frac{2}{3}\mu)\mathbf{I}^{2x} \otimes \mathbf{I}^{2x}. \quad (3-23)$$

$$\mu = \mu_1(1-f) / \left( 1 + 6f \left( \frac{\kappa_1 + 2\mu_1}{9\kappa_1 + 8\mu_1} \right) \right). \quad (3-24)$$

$$\kappa = 4(1-f) / \left( \frac{4}{\kappa_1} + \frac{3f}{\mu_1} \right). \quad (3-25)$$

$$\mu_1 = \frac{E_0}{2(1+\nu)}. \quad (3-26)$$

$$\kappa_1 = \frac{E_0}{3(1-2\nu)}. \quad (3-27)$$

where  $E$  is the Young's modulus of the porous fiber,  $\mathbf{I}^{2x}$  and  $\mathbf{I}^{4x}$  are the second and fourth order identity tensors,  $\mu$  and  $\kappa$  are the effective elastic shear and bulk moduli,  $\mu_1$  and  $\kappa_1$  are functions of the local matrix elastic shear and bulk moduli, and  $f$  is the void volume fraction.  $E_0$  is the modulus of the solid fiber without any voids, and  $\nu$  is Poisson's ratio, which is assumed to be 0.3 for glassy polymers in general. Although Mori-Tanaka theory has been developed for lower void volume fractions, it can be utilized for materials with void volume fractions up to 50% [45].

The 2D honeycomb and 3D open cell models are structural models [46-48], developed for foams and cellular materials, based on the analysis of approximate geometries of unit cells. The modulus of the 2D honeycomb with the hexagonal unit cell is:

$$E = 2.3E_0 \left( \frac{\sqrt{3}}{2}(1-f) \right)^3. \quad (3-28)$$

The modulus of the 3D open cell model with the cubic unit cell is given by Gibson and Ashby [48] as:

$$E = E_0(1 - f)^2. \quad (3-29)$$

The 2D honeycomb and 3D open cell models were derived assuming high porosity. The 2D honeycomb can give good prediction for void volume fractions above 70% but is unrealistic for void volume fractions less than 20%. The 3D open cell model can give good prediction with porosities in the range of 10 to 90% [47].

For all three different theoretical models, we assumed  $E_0$  to be 3.63 GPa, based on the value of the cast, annealed PS film. The relationship between  $f$  and  $E$  can be established according to Equations (3-23) through (3-29). Figure 3-14 compares the predictions of the three theoretical models with the data of as-spun and annealed PS fibers; the fiber moduli have been normalized by  $E_0 = 3.63$  GPa, based on the value obtained for the cast, annealed PS film. Those solid symbols located on the left hand side of the figure represent the data points of annealed fibers. Note that the assumption of no voids (void volume fraction = 0) is made here for annealed fibers; a few microvoids might still be present. Those symbols located in the middle part of the figure represent the data for as-spun fibers. The solid symbols and open symbols represent void volume fraction calculated from the shrinkage of fiber diameter, and from analysis of TEM image, respectively. For fibers electrospun from a 30 wt% PS/DMF solution under 29% relative humidity, the void volume fraction calculated from the shrinkage of fiber diameter and from analysis of TEM images, is about 0.5 and 0.3, respectively. The difference between these two analyses is explained in Chapter 2.3.5. Both of these analyses yield only an approximate estimation of the actual porosity of the fibers. Besides, the molecular chain orientation of the amorphous PS fibers is not considered here. It is assumed to be the same for both as-spun fibers and annealed fibers no matter what the fiber diameter is. This assumption might also contribute to the deviation of the prediction for the elastic modulus versus the void volume fraction.

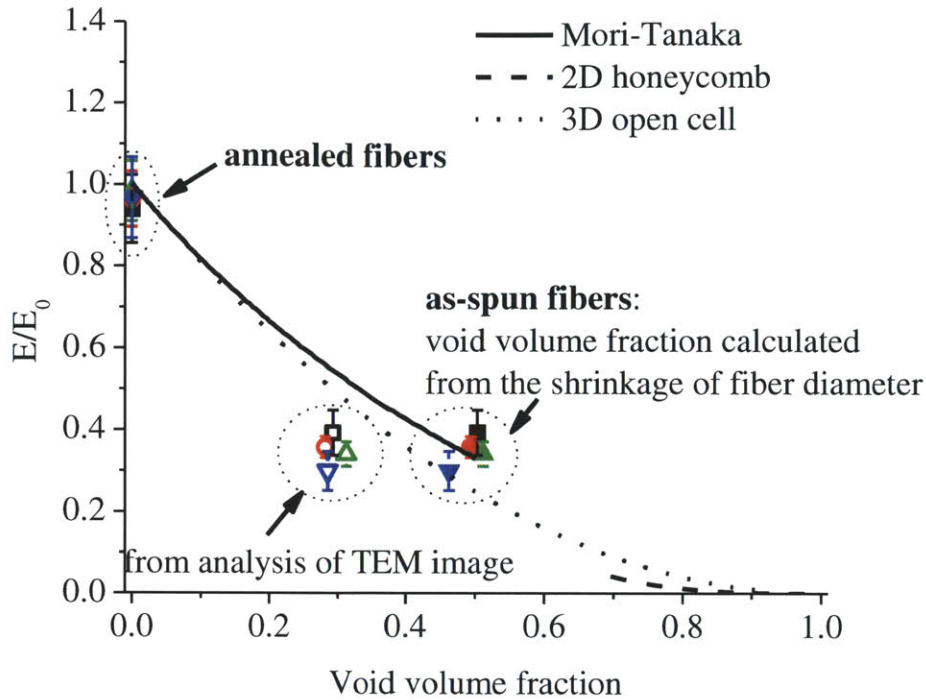


Figure 3-14. Comparison between different theoretical models (line) and experimental data from 30 wt% PS/DMF solutions (■: 43%, ●: 37%, ▲: 29%, ▼: 24% relative humidity). Solid symbols: void volume fraction calculated from the shrinkage of fiber diameter, and open symbols: from analysis of TEM image).

Mechanical properties of the semicrystalline PAN are influenced by the degree of crystallinity and orientation. The degree of crystallinity and its orientation of PAN can be measured by wide-angle X-ray diffraction (WAXD). A typical diffraction pattern and equatorial diffractogram of aligned electrospun PAN bundles are shown in Figure 3-15(a) and (b). Two equatorial peaks are located at  $2\theta = 16.5^\circ$  and  $28.9^\circ$ , corresponding to Bragg spacing of  $5.37 \text{ \AA}$  from  $(10\bar{1}0)$  reflection and  $3.09 \text{ \AA}$  from  $(1120)$  reflection, for all our PAN samples. These are characteristic of the hexagonal crystal unit cell of PAN [40,49-50]. Note that Miller indices  $(hki)$  are used for the identification of planes in hexagonal crystals, where the index  $i$  is equal to  $-(h+k)$  and can be omitted. Using a linear combination of Lorentzian functions to do the peak fitting for the curve in Figure 3-15(b), and splitting the total diffraction

pattern into amorphous and crystalline contributions, the degree of crystallinity  $X_c$  can be calculated:

$$X_c = \frac{A_c}{A_c + A_a} \quad (3-30)$$

where  $A_c$  and  $A_a$  are the areas under the crystalline and the amorphous peaks, respectively. The azimuthal scans of the diffraction rings at 5.37 Å peak are shown in Figure 3-15(c), from which an orientation parameter  $f_1$  for the polymer crystallites can be calculated [51]:

$$f_1 = \frac{90 - \varphi_0}{90} \quad (3-31)$$

where  $\varphi_0$  is the half-width of a reflected peak at half height. In order to understand the degree of chain orientation, FTIR is used to measure the dichroism of the nitrile-stretching ( $-C \equiv N$ ) group vibration around 2242  $\text{cm}^{-1}$ , as shown in Figure 3-15(d) and (e). The chain orientation factor  $f_2$  can be calculated by Equation (2-1) [40]. The transition moment angle between the direction of dipole moment change and the axis of the polymer chain is assumed to be 73° according to the literature [49]. The results of the crystallinity, molecular orientation:  $f_1$  and  $f_2$ , and Young's modulus for PAN samples are listed in Table 3-4. Not much difference can be found between  $f_1$  (0.5 ~ 0.6) and  $f_2$  (0.35 ~ 0.4) for as-spun and annealed fibers with different fiber diameters and from different polymer concentrations. The approximate independence of molecular chain orientation for PAN fibers is expected for PS fibers, as well. However, this apparent independence might be due to an insufficiently broad range of average fiber diameter. For example, these samples only differ in diameter from 0.60  $\mu\text{m}$  to 1.86  $\mu\text{m}$  for PAN fibers, and from 0.90  $\mu\text{m}$  to 4.09  $\mu\text{m}$  for PS fibers. On the other hand, if fibers can be produced with diameters that range from a few tens of nanometers to microns, or at least differ by one order of magnitude, the orientation of molecular chain in polymer fibers might change dramatically. For a 14 wt% PAN/DMF solution electrospun under 46% relative humidity, annealed fibers have an increase of crystallinity from 0.35 to 0.56 when compared to as-spun fibers. The increase of crystallinity is expected to enhance the mechanical performance. Therefore, the increase of the modulus from as-spun PAN



fibers to annealed PAN fibers can be the combined effect of the increasing crystallinity and the decreasing porosity. On the other hand, as-spun fibers from 11 wt% and 14 wt% PAN/DMF solutions have similar orientation and crystallinity. The difference in elastic modulus mainly comes from the contribution of the void volume fraction.

Table 3-5. Mechanical properties of as-spun and annealed PAN fibers

wt%	Annealed Temp.(°C)	RH (%)	Diameter ( $\mu\text{m}$ )	Modulus (GPa)	Crystallinity (%)	Crystallinity	
						$f_1$	$f_2$
14	As-spun	46	1.86 ( $\pm 0.08$ )	2.89	35	0.57	0.35
	100	46	1.58 ( $\pm 0.13$ )	5.28	56	0.60	0.39
	As-spun	31	1.35 ( $\pm 0.21$ )	5.29	31	0.57	0.40
11	As-spun	31	0.82 ( $\pm 0.05$ )	3.55	35	0.51	0.35

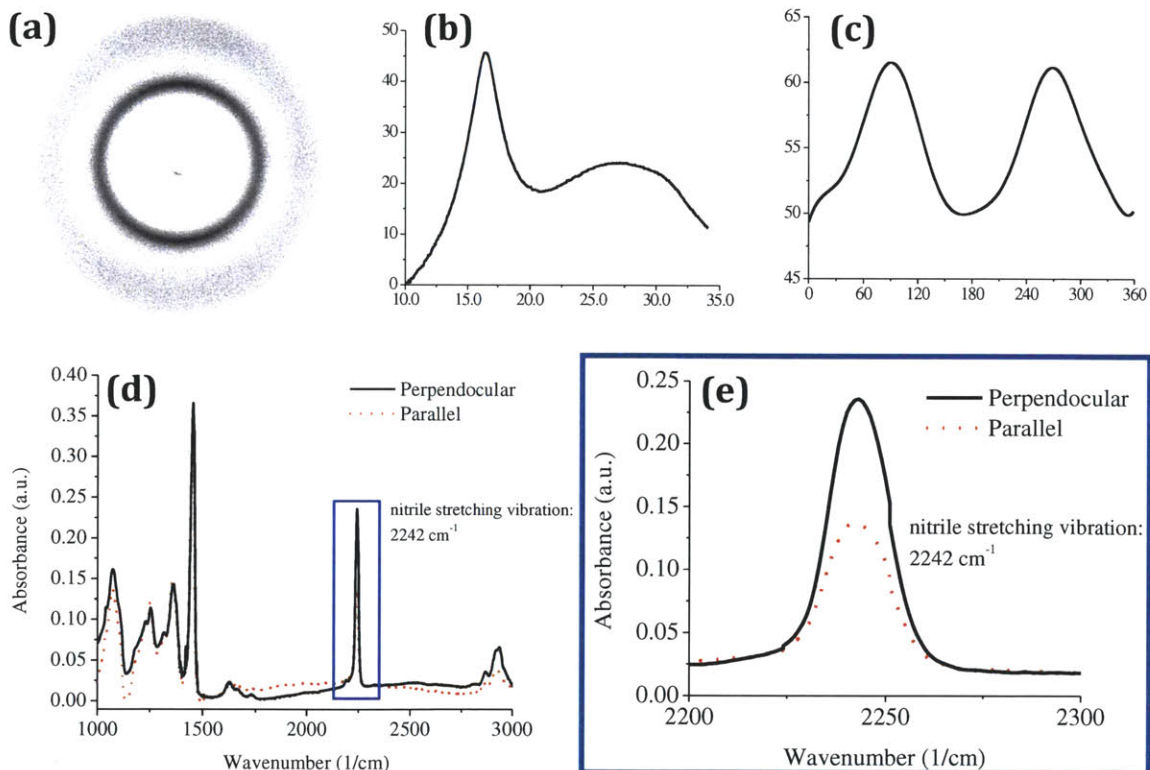


Figure 3-15. (a) Two-dimensional WAXD pattern, (b) WAXD diffractogram, (c) WAXD azimuthal scan, (d) polarized FTIR spectrum of electrospun PAN fibers, and (e) the enlarged version of the blue window in (d).

### 3.3 Concluding Remarks

Porous structures within fibers electrospun in a humid environment were found in a PS/DMF system, as well as other polymer systems. Because DMF is a commonly used solvent in electrospinning, the possible occurrence of this phenomenon may be more prevalent than has been appreciated to date, and may also occur for other similar polymer-solvent systems. The reason for porous structures to occur within fibers is because the humidity in the environment plays a role as nonsolvent. For the miscibility of water with DMF, liquid-induced phase separation precedes solidification due to the slow evaporation rate of DMF. The formation of porous features within the fibers has a significant effect on the mechanical performance. Other properties such as optical properties and electrical properties may be altered with different porosity, void sizes, void shapes, and their distribution inside the fibers. By controlling the environmental factors (such as relative humidity, temperature, and surrounding gas composition), the polymer-solvent interaction, the concentration of polymer, and the molecular weight of polymer, either porous or homogeneous solid fibers can be produced and manipulated in accord with the needs of specific applications, such as sensors, membranes in fuel cells, filtration, drug delivery, catalytic systems, hydrogen storage systems, protective clothing with breathability and toxic chemical resistance, and tissue engineering. For example, porous fibers can be considered a composite material composed of polymer and air. Depending on their volume fraction and distribution, the gas permeability through the fiber is different, which can be used to advantage for gas separation or to enhance the breathability of a material. For the collapsed structures such as those observed in Figure 3-11(b) and (d), the shape is excellent for enhancing the oleophobic or hydrophobic nature of the nonwoven material because the large re-entrant roughness stabilizes the interface and is resistant to wetting. Also, some of our collapsed fiber geometries are similar to the capillary surface materials with surfaces engineered to contain deep grooves, which can act as capillary channels or fluid conduits. The phenomenal absorbency of these fibers can be used in liquid chromatography. Most of this chapter has been published in Ref. [52].

### 3.4 References

- [1] Statton WO. "Microvoids in fibers as studied by small-angle scattering of x-rays", *Journal of Polymer Science* 1962; 58: 205-220.
- [2] Casper CL, Stephens JS, Tassi NG, Chase DB, Rabolt JF. "Controlling surface morphology of electrospun polystyrene fibers: Effect of humidity and molecular weight in the electrospinning process", *Macromolecules* 2004; 37: 573-578.
- [3] Megelski S, Stephens JS, Chase DB, Rabolt JF. "Micro- and nanostructured surface morphology on electrospun polymer fibers", *Macromolecules* 2002; 35: 8456-8466.
- [4] Bognitzki M, Czado W, Frese T, Schaper A, Hellwig M, Steinhart M, Greiner A, Wendorff JH. "Nanostructured fibers via electrospinning", *Adv. Mater.* 2001; 13: 70-72.
- [5] Jeun JP, Kim YH, Lim YM, Choi JH, Jung CH, Kang PH, Nho YC. "Electrospinning of poly(L-lactide-co-D,L-lactide)", *J. Ind. Eng. Chem.* 2007; 13: 592-596.
- [6] Miyauchi Y, Ding B, Shiratori S. "Fabrication of a silver-ragwort-leaf-like superhydrophobic micro/nanoporous fibrous mat surface by electrospinning", *Nanotechnology* 2006; 17(20): 5151-5156.
- [7] Dayal P, Kyu T. "Porous fiber formation in polymer-solvent system undergoing solvent evaporation", *J. Appl. Phys.* 2006; 100: 043512.
- [8] Guenther AJ, Khombhongse S, Liu WX, Dayal P, Reneker DH, Kyu T. "Dynamics of hollow nanofibers formation during solidification subjected to solvent evaporation", *Macromol. Theory Simul.* 2006; 15: 87-93.
- [9] Dayal P, Liu J, Kumar S, Kyu T. "Experimental and theoretical investigation of porous structure formation in electrospun fibers", *Macromolecules* 2007; 40: 7689-7694.
- [10] Doménech-Carbó MT, Aura-Castro E. "Evaluation of the phase inversion process as an application method for synthetic polymers in conservation work", *Studies in Conservation* 1999; 44: 19-28.
- [11] Tripatanasuwan S, Zhong ZX, Reneker DH. "Effect of evaporation and solidification of the charged jet in electrospinning of poly(ethylene oxide) aqueous solution", *Polymer* 2007; 48: 5742-5746.

- [12] Mathur D, Nauman EB. "The effect of diblocks and ripening on the Izod impact of bulk PS/PB blends", *J. Appl. Polym. Sci.* 1999; 72: 1165-1176.
- [13] Yokouchi M, Seto S, Kobayashi Y. "Comparison of polystyrene, poly(styrene acrylonitrile), high-impact polystyrene, and poly(acrylonitrile butadiene styrene) with respect to tensile and impact properties", *J. Appl. Polym. Sci.* 1983; 28: 2209-2216.
- [14] Srinivasarao M, Collings D, Philips A, Patel S. "Three-dimensionally ordered array of air bubbles in a polymer film", *Science* 2001; 292: 79-83.
- [15] Reneker DH, Chun I. "Nanometer diameter fibers of polymer, produced by electrospinning", *Nanotechnology* 1996; 7: 216-223.
- [16] Limaye AV, Narhe RD, Dhote AM, Ogale SB. "Evidence for convective effects in breath figure formation on volatile fluid surfaces", *Phys. Rev. Lett.* 1996; 76: 3762.
- [17] Yilmaz L, McHugh AJ. "Analysis of nonsolvent solvent polymer phase-diagrams and their relevance to membrane formation modeling", *J. Appl. Polym. Sci.* 1986; 31: 997-1018.
- [18] Tsay CS, McHugh AJ. "Mass-transfer modeling of asymmetric membrane formation by phase inversion", *Journal of Polymer Science: Part B: Polymer Physics* 1990; 28: 1327-1365.
- [19] Matsuyama H, Teramoto M, Nakatani R, Maki T. "Membrane formation via phase separation induced by penetration of nonsolvent from vapor phase. I. Phase diagram and mass transfer process", *J. Appl. Polym. Sci.* 1999; 74: 159-170.
- [20] Yip Y, McHugh AJ. "Modeling and simulation of nonsolvent vapor-induced phase separation", *J. Membrane Sci.* 2006; 271: 163-176.
- [21] Tompa H. *Polymer Solutions*, Butterworths, London, 1956: 46.
- [22] Altena FW, Smolders CA. "Calculation of liquid liquid-phase separation in a ternary-system of a polymer in a mixture of a solvent and a nonsolvent", *Macromolecules* 1982; 15: 1491-1497.
- [23] Brandrup J, Immergut EH, Grulke EA, Abe A, Bloch DR. *Polymer Handbook*, 4th ed.; Wiley-Interscience: New York, 1999.

- [24] Burke J. Solubility Parameters: Theory and Application, AIC Book and Paper Group Annual 1984; 3: 13-58.
- [25] Wolf BA, Willms MM. "Measured and calculated solubility of polymers in mixed-solvents-co-non-solvency", *Makromol. Chem.* 1978; 179: 2265-2277.
- [26] Kongkhleng T, Kotaki M, Kousaka Y, Umemura T, Nakaya D, Chirachanchai S. "Electrospun polyoxymethylene: Spinning conditions and its consequent nanoporous nanofibers", *Macromolecules* 2008; 41: 4746-4752.
- [27] Mattoso LHC, Offeman RD, Wood DF, Orts WJ, Medeiros ES. "Effect of relative humidity on the morphology of electrospun polymer fibers", *Can. J. Chem. Rev. Can. Chim.* 2008; 86: 590-599.
- [28] Koombhongse S, Liu WX, Reneker DH. "Flat polymer ribbons and other shapes by electrospinning", *Journal of Polymer Science: Part B: Polymer Physics* 2001; 39: 2598-2606.
- [29] Timoshenko SP, Gere JM. *Theory of Elastic Stability*, 2nd ed.; McGraw-Hill: New York, 1961.
- [30] Flügge W. *Stresses in Shells*, 2nd ed.; Springer: New York, 1973.
- [31] Pauchard L, Hulin JP, Allain C. "Drops that buckle", *Europhysics News* 2005; 36: 9-11.
- [32] Pauchard L, Allain C. "Buckling instability induced by polymer solution drying", *Europhys. Lett.* 2003; 62: 897-903.
- [33] Pauchard L, Couder Y. "Invagination during the collapse of an inhomogeneous spheroidal shell", *Europhys. Lett.* 2004; 66: 667-673.
- [34] Zussman E, Chen X, Ding W, Calabri L, Dikin DA, Quintana JP, Ruoff RS. "Mechanical and structural characterization of electrospun PAN-derived carbon nanofibers", *Carbon* 2005; 43: 2175.
- [35] Wang T, Kumar S. "Electrospinning of polyacrylonitrile nanofibers", *J. Appl. Polym. Sci.* 2006; 102: 1023.
- [36] Jalili R, Morshed M, Abdolkarim S, Ravandi H. Fundamental parameters affecting electrospinning of PAN nanofibers as uniaxially aligned fibers", *J. Appl. Polym. Sci.* 2006; 101: 4350.
- [37] Mack JJ, Viculis LM, Ali A, Luoh R, Yang G, Hahn HT, Ko FK, Kaner RB. "Graphite

- nanoplatelet reinforcement of electrospun polyacrylonitrile nanofibers”, *Adv. Mater.* 2005; 17: 77.
- [38] Ge JJ, Hou H, Li Q, Graham MJ, Greiner A, Reneker DH, Harris FW, Cheng SZD. “Assembly of well-aligned multiwalled carbon nanotubes in confined polyacrylonitrile environments: Electrospun composite nanofiber sheets”, *J. Am. Chem. Soc.* 2004; 126: 15754.
- [39] Gu SY, Wu QL, Ren J, Vancso GJ. “Mechanical properties of a single electrospun fiber and its structures”, *Macromol. Rapid Commun.* 2005; 26: 716.
- [40] Fennessey SF, Farris RJ. “Fabrication of aligned and molecularly oriented electrospun polyacrylonitrile nanofibers and the mechanical behavior of their twisted yarns”, *Polymer* 2004; 45: 4217.
- [41] Mori T, Tanaka K. “Average stress in matrix and average elastic energy of materials with misfitting inclusions”, *Acta Metall.* 1973; 21: 571.
- [42] Benveniste Y. “A new approach to the application of mori-tanaka theory in composite-materials”, *Mech. Mater.* 1987; 6: 147.
- [43] Berryman JG. “Long-wavelength propagation in composite elastic media. 2. Ellipsoidal inclusions”, *J. Acoust. Soc. Am.* 1980; 68(6): 1820.
- [44] Danielsson M, Parks DM, Boyce MC. “Micromechanics, macromechanics and constitutive modeling of the elasto-viscoplastic deformation of rubber-toughened glassy polymers”, *J. Mech. Phys. Solids* 2007; 55: 533.
- [45] Weng GJ. “Some elastic properties of reinforced solids, with special reference to isotropic ones containing spherical inclusions”, *Internat. J. Engng. Sci.* 1984; 22: 845.
- [46] Unnikrishnan VU, Unnikrishnan GU, Reddy JN, Lim CT. “Atomistic-mesoscale coupled mechanical analysis of polymeric nanofibers”, *J. Mater. Sci.* 2007; 42: 8844.
- [47] Thelen S, Barthelat F, Brinson LC. “Mechanics considerations for microporous titanium as an orthopedic implant material”, *J. Biomed. Mat. Res.* 2004; 69A: 601.
- [48] Gibson L, Ashby M. *Cellular solids: Structure and properties*. New York: Cambridge University Press, 1997.
- [49] Bashir Z, Tipping AR, Church SP. “Orientation studies in polyacrylonitrile films

- uniaxially drawn in the solid-state”, *Polymer International* 1994; 33: 9.
- [50] Davidson JA, Jung HT, Hudson SD, Percec S. “Investigation of molecular orientation in melt-spun high acrylonitrile fibers”, *Polymer* 2000; 41: 3357-3364.
- [51] Zussman E, Burman M, Yarin AL, Khalfin R, Cohen Y. “Tensile deformation of electrospun nylon-6,6 nanofibers”, *Journal of Polymer Science: Part B: Polymer Physics* 2006; 44: 1482.
- [52] Pai CL, Boyce MC, Rutledge GC. “Morphology of Porous and Wrinkled Fibers of Polystyrene Electrospun from Dimethylformamide”, *Macromolecules* 2009; 42: 2102.

## **Chapter 4 Wrinkled Surface Topographies of Electrospun Fibers**

### **4.1 Introduction**

Electrospun polymer fibers are shown to have wrinkled surface topographies that result from buckling instabilities during processing. Similar buckling phenomena have been studied for thin films on compliant substrates [1-3] and spheroidal structures with layered core-shell structures [4-6]. Various deformation mismatch conditions have been found and/or used to trigger buckling, including: deposition of a coating on a pre-tensioned elastomeric substrate followed by release of the pretension [2-3]; thermal expansion mismatch between a film and substrate [4]; and mismatch of either shrinkage or growth rates in multi-layered structures (e.g., dehydration of vegetable and fruits [5], growth of living plants [6]). We postulate the mechanism underlying the surface wrinkling of electrospun fibers to be a deformation mismatch between the shell and the core due to core shrinkage during solvent evaporation. A glassy shell forms on the surface of the gel-like core during solvent evaporation; continued evaporation leads to a contraction mismatch between the core and shell that triggers buckling of the shell. The wrinkled topographies are quantified in terms of the critical buckling wave number and wavelength. The results explain the observed wrinkled topographies and provide a framework for designing fibers with high specific surface areas and textured/patterned surface topographies to enhance surface dominated properties in fibers and fibrous mats.

### **4.2 Results and Discussion**

#### **4.2.1 Experimental Observation of Wrinkled Topographies**

In addition to the generally expected circular cross-section and smooth surface topology, a variety of cross-sectional shapes and corresponding surface textures have been observed [7-8] as shown in the representative examples of Figure 4-1. These include flat ribbon-like fiber geometries and wrinkled fiber surface



topographies, which further increase the specific surface area and also provide a texture suitable for additional property enhancements.

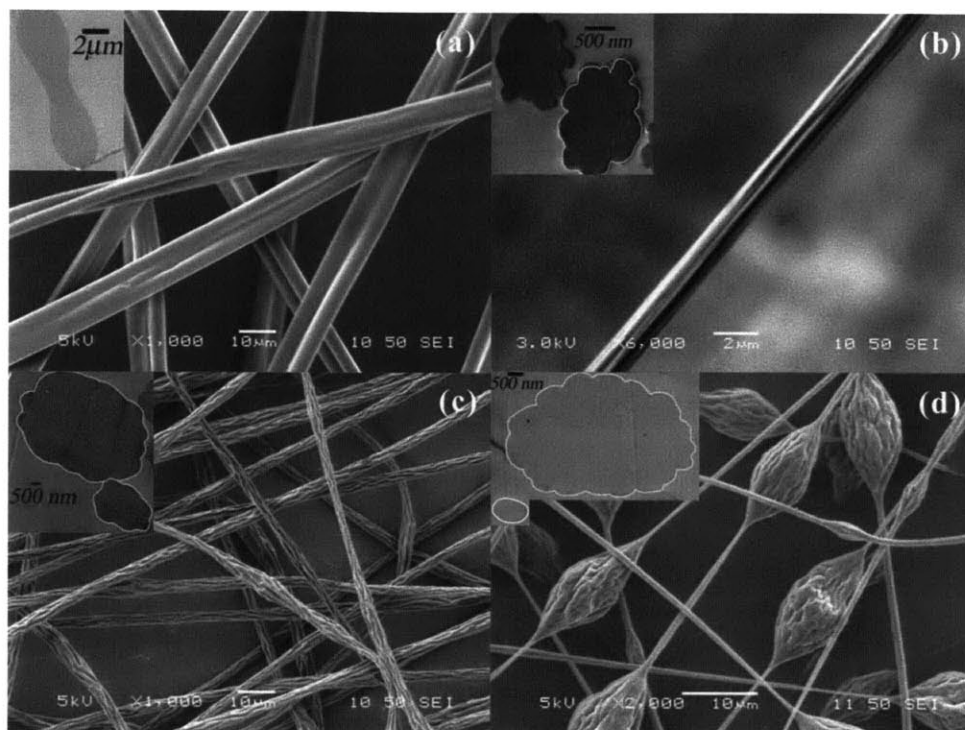


Figure 4-1. Surface morphology of polymer fibers electrospun from (a) a 30 wt% PS/THF solution; (b) a 14 wt% PAN/DMF solution; (c) a 30 wt% PS/DMF solution; and (d) a 15 wt% PS in a mixed solvent of DMF and THF. Inset fibers outlined in white for emphasis.

Figure 4-1(a) provides a SEM image of PS fibers electrospun from a 30 wt% solution of amorphous, atactic PS ( $M_w = 280$  kg/mol) dissolved in THF; the insert TEM image shows the corresponding cross-section typical of these fibers. The ribbon-like morphology has a minor diameter of  $\sim 2.1$   $\mu\text{m}$  and a major diameter of  $\sim 13.5$   $\mu\text{m}$ , and exhibits a wave number, defined as the number of maxima in radius around the perimeter ( $S$ ) of the fiber cross-section, of  $k = 2$  and wavelength  $\lambda = S/k \sim 14$   $\mu\text{m}$ . Figure 4-1(b) shows images of semicrystalline PAN fibers electrospun at 31% relative humidity (RH) from a 14 wt% solution of PAN ( $M_w = 150$  kg/mol) dissolved in DMF. The average fiber diameter is  $1.35 (\pm 0.21)$   $\mu\text{m}$ . These fibers

exhibit a wrinkled topography with  $k \sim 10$  and  $\lambda \sim 400$  nm. Figure 4-1(c) shows images for PS fibers electrospun at 15% RH from a 30 wt% PS/DMF solution. The fiber diameter is  $\sim 2.5$   $\mu\text{m}$  with  $k \sim 7$  and  $\lambda \sim 1.1$   $\mu\text{m}$ , and bead diameter  $\sim 5.2$   $\mu\text{m}$  with  $k \sim 12$  and  $\lambda \sim 1.4$   $\mu\text{m}$ . Figure 4-1(d) shows images for PS fibers electrospun from a 15 wt% solution of PS dissolved in a mixed solvent of DMF and THF (1:1 by weight). The fibers exhibit beads-on-string morphology with fiber diameter  $\sim 0.92$  ( $\pm 0.14$ )  $\mu\text{m}$  and maximum bead diameter  $\sim 8.86$  ( $\pm 1.80$ )  $\mu\text{m}$ . The cross-sectional TEM image in the inset shows a bead with  $k \sim 16$  and  $\lambda \sim 1$   $\mu\text{m}$  (cutting the bead diameter at  $\sim 3.8$   $\mu\text{m}$  in this case, not necessarily at the maximum diameter).

#### 4.2.2 Mechanism of Wrinkled Fibers

Khoombungse et al. proposed [7] a mechanism for the formation of shaped fibers whereby atmospheric pressure tends to collapse the thin glassy skin initially formed on the liquid jet during solvent evaporation, giving a ribbon-like structure. Pauchard and Allain [9-10] and Pauchard and Couder [11] observed a similar phenomenon as a result of solvent evaporation from a sessile droplet of polymer solution. The collapse of the droplet leads to topographies that are qualitatively similar to the surface topographies observed in the beads of beads-on-string structures of electrospun fibers (Figure 4-1(d)). The key to understanding this phenomenon is the buckling instability associated with the formation of a thin glassy skin (outer shell) on the surface of the fluid or gel-like core during processing. Solvent evaporation and drying lead to the rapid formation of a thin, elastic glassy shell; as solvent evaporation from the core proceeds, the core contracts and pulls radially inward on the stiff outer shell, resulting in a compressive hoop stress in the shell. Once a critical compressive stress is reached, buckling of the shell is energetically favored over continued uniform circumferential compression of the shell; the dominant buckling wavelength is that which results in the lowest total energy for the system. The total energy consists of the membrane and bending strain energy of the shell and the volumetric and shear strain energy of the core. The interplay between core and shell energy contributions is analogous to the classic

problem of buckling of a beam on an elastic foundation: consideration of the elastic foundation strain energy (for our fiber case, the gel-like core is the “elastic foundation”) leads to higher buckling modes being favored over the lowest mode of the shell, as demonstrated in Figure 4-2.

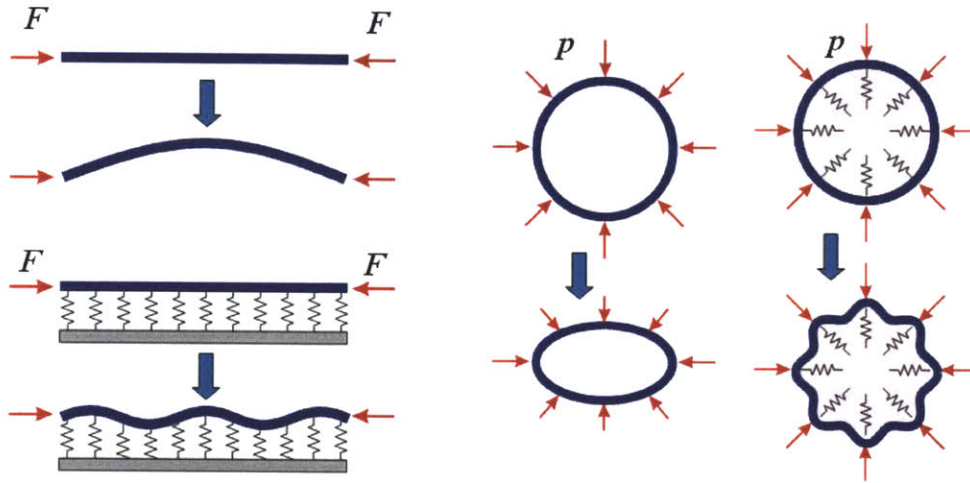


Figure 4-2. The interplay between core and shell energy contributions of the fiber is analogous to the classic problem of buckling of a beam on an elastic foundation (courtesy of Lifeng Wang).

#### 4.2.3 Analytical Solution for Critical Wave Number and Wavelength

The critical buckling conditions of a long cylindrical elastic shell containing a compliant elastic core subject to external pressure have been investigated in the context of the limiting pressure of structural tubes [12-13]. The Hermann and Forrestal expression [12] for the buckling pressure  $p$  of a shell as a function of buckling wave number  $k$  (for  $k = 2, 3, 4, \dots$ ), shell properties and geometry (Young’s modulus  $E_s$ , Poisson’s ratio  $\nu_s$ , thickness  $t$ ), and core properties and geometry (Young’s modulus  $E_c$ , Poisson’s ratio  $\nu_c$ , radius  $a$ ) is given by the following equations and illustrated in Figure 4-3:

$$\frac{p}{p_0(1+\alpha)} = \frac{k^2 - 1}{3} + \frac{4(1-\nu_s^2)}{(1+\nu_c)[2k(1-\nu_c) - (1-2\nu_c)]} \left( \frac{E_c}{E_s} \right) \left( \frac{a}{t} \right)^3, \quad (4-1)$$

where  $\alpha = \left[ \frac{1-\nu_s^2}{(1+\nu_c)(1-2\nu_c)} \right] \left( \frac{E_c}{E_s} \right) \left( \frac{a}{t} \right), p_0 = \frac{E_s}{4(1-\nu_s^2)} \left( \frac{t}{a} \right)^3$ .

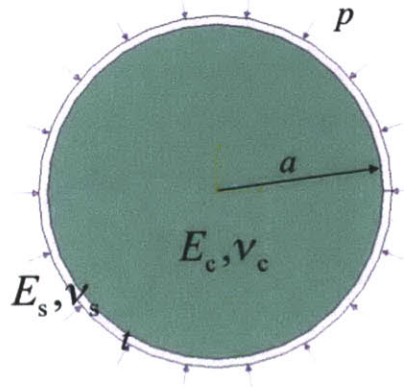


Figure 4-3. The illustration of properties and geometry of the core and shell.

The critical buckling wave number  $k_{crit}$  corresponds to the  $k$  that gives the lowest buckling pressure according to Equation (4-1). This linearized approximate solution is accurate for values of elastic core Poisson ratio between 0.4 and the incompressible limit of 0.5 [12]. The Hermann and Forrestal solution is applicable to our fiber system since the fluid or gel-like core of the fiber has a low shear modulus and a high bulk modulus which, accordingly, corresponds to a Poisson's ratio very close to 0.5. By minimizing Equation (4-1) with respect to  $k$  and then taking the limiting case of  $\nu_c$  approaching 0.5, we obtain expressions for the critical wave number,  $k_{crit}$ , and wavelength,  $\lambda_{crit}$ :

$$k_{crit} = (a/t)(3\bar{E}_c/\bar{E}_s)^{1/3}, k_{crit} \geq 2, \quad (4-2)$$

$$\lambda_{crit} = 2\pi t(3\bar{E}_c/\bar{E}_s)^{-1/3}, \lambda_{crit} \leq \pi a, \quad (4-3)$$

where  $\bar{E} = E/(1-\nu^2)$ . The wave number is seen to scale with elastic property ratio via  $(\bar{E}_c/\bar{E}_s)^{1/3}$  and linearly with  $a/t$ . The wavelength scales with  $(\bar{E}_c/\bar{E}_s)^{-1/3}$ , linearly with  $t$ , and, for  $\lambda_{crit} < \pi a$ , is independent of the radius  $a$ . When  $a/t < 2(3\bar{E}_c/\bar{E}_s)^{-1/3}$ , the most favorable wavelength is limited by the circumference and hence  $\lambda_{crit} = \pi a$ . The scaling of the wavelength with shell thickness and property ratios are

consistent with those for wavy thin films on compliant substrates at small deformations [2-3]. This consistency between the fiber and film wavelength scaling can be explained by simplified energy scaling and minimization argument. For both the fiber and the film, the shell energy contribution is due to bending and scale as  $\sim \overline{E}_s t^3 A^2 / \lambda^4$ ; the “foundation” energy contribution is due to straining that extends into the substrate (for film) or the core (for fiber) by a depth  $L_0$  that scales with the wavelength  $L_0 \sim \lambda$  giving energy scaling as  $\sim \overline{E}_c A^2 / L_0$ . Energy minimization then gives  $\lambda \sim t(3\overline{E}_c / \overline{E}_s)^{-1/3}$ , with  $\lambda$  being independent of radius and to scale in the same way as that of the film [14].

#### 4.2.4 Finite Element Analysis for Critical Wave Number and Wavelength

Buckling modes were determined using FEA (ABAQUS/STANDARD) [15] as follows. First, external pressure loading was assumed and an eigen-analysis was conducted to determine the critical wave number. Meshes were then “seeded” with infinitesimal amplitude of the critical mode. The core was then “contracted” to simulate solvent evaporation, leading to the radial mismatch condition that triggers the buckling.

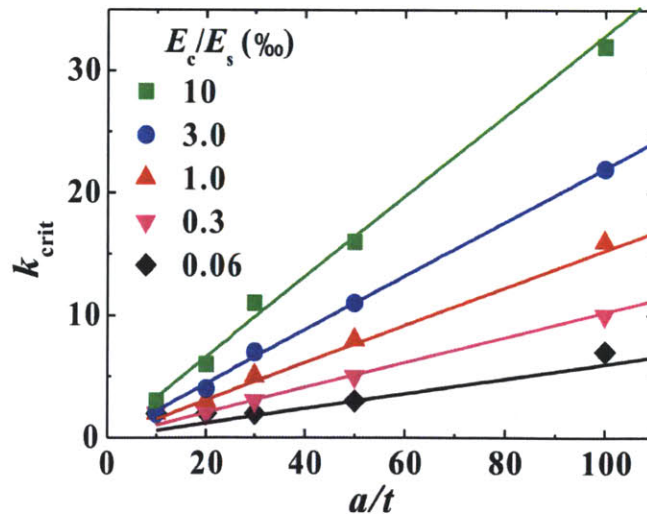


Figure 4-4. Dependence of critical wave number on  $a/t$  for different  $E_c/E_s$ . The lines are the Hermann and Forrestal analytical results of Equation (4-2) determined herein; the symbols are numerical results.

In Figure 4-4, both numerical and analytical results for the critical wave number  $k_{\text{crit}}$  as a function of  $a/t$  are shown for different  $E_c/E_s$ , and found to be in excellent agreement. At any given  $E_c/E_s$ , an increase in  $a/t$  gives an increase in  $k_{\text{crit}}$  that scales linearly with  $a/t$ ; at any given  $a/t$ , an increase in  $E_c/E_s$  gives an increase in  $k_{\text{crit}}$  that scales with the cube root of  $E_c/E_s$ . Both trends reflect the increased energy penalty encountered in deforming a core of increasing stiffness, where the increase in  $k_{\text{crit}}$  optimally reduces the core strain energy.

Figure 4-5 shows a map of wrinkled topographies as a function of  $a/t$  (from 10 to 100) and  $E_c/E_s$  (from 0.06‰ to 10‰). The buckled conformations depict a core contraction of about 50%. This map provides a visual explanation of the wrinkled topographies observed in Figure 4-1. For low  $E_c/E_s$  and low  $a/t$ , the core contraction provides relatively little energy penalty and hence the shell buckles in its lowest mode (the mode that would occur under pressure in the absence of any core, meaning  $k = 2$ ). As the core stiffness increases, either through increase in  $E_c/E_s$  or increase in  $a/t$ , the core energy penalty increases and the critical wave number  $k_{\text{crit}}$  increases.

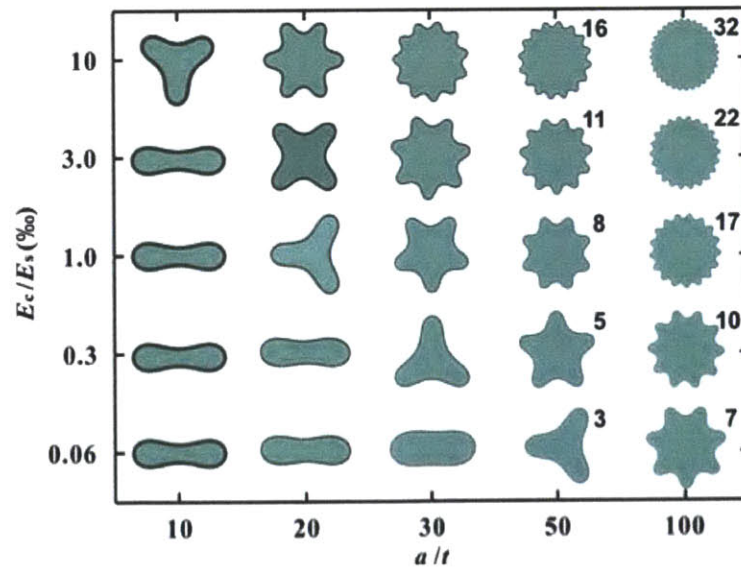


Figure 4-5. Map of numerical results for wrinkled cross-section as a function of  $E_c/E_s$  and  $a/t$ , shown for each pair of  $E_c/E_s$  and  $a/t$  values indicated by the axis labels.

The dependence of the critical buckling wave length on  $E_c/E_s$  as obtained from the analytical model and the numerical simulations is shown in Figure 4-6. Figure 4-6(a) plots  $\lambda_{\text{crit}}/t$  as a function of  $E_c/E_s$  for different  $a/t$  on a log plot. Equation (4-3), the analytical solution, indicates that  $\lambda_{\text{crit}}/t$  is independent of  $a/t$  (giving the solid line) and the numerical results are in agreement with this, with the exception of those cases where the wave number is 2 (which corresponds to the geometric limiting case of  $\lambda_{\text{crit}} = \pi a$ ).  $\lambda_{\text{crit}}/t$  is shown to be an exponential function (with exponent = -1/3) of  $E_c/E_s$ , independent of  $a/t$ , except for the cases of low stiffness core where  $k_{\text{crit}}$  is 2. This also indicates that, when  $k_{\text{crit}} > 2$ , the buckling wavelength is independent of fiber diameter. This behavior is illustrated graphically in the topography results of Figure 4-6(b), which show numerical results for cross-sections of three fibers with identical shell thickness but different radii. For the two cases of  $E_c/E_s = 10^{-3}$  and  $E_c/E_s = 10^{-2}$ , one obtains  $\lambda_{\text{crit}} = 41t$  and  $19t$ , respectively. Note that for each  $E_c/E_s$  case, the wavelength is nearly the same (i.e., independent of fiber radius).

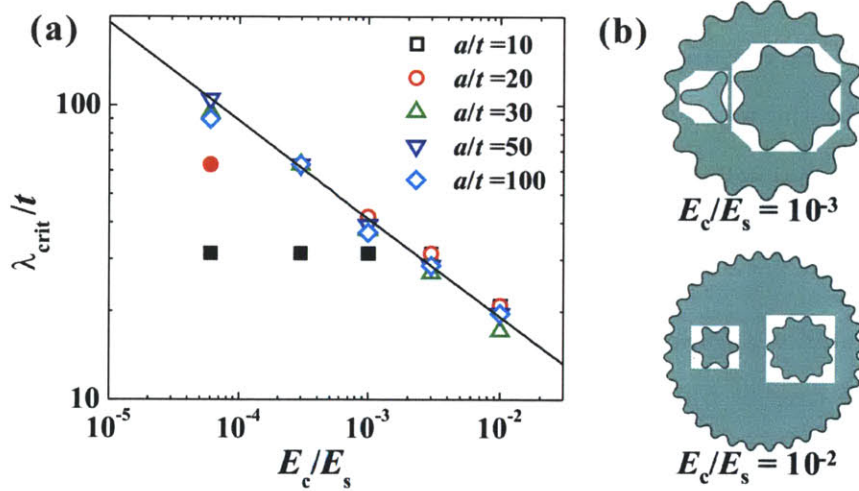


Figure 4-6. (a) Dependence of  $\lambda_{\text{crit}} /t$  on  $E_c/E_s$  for different  $a/t$  (solid line is the theory solution according to Equation (4-3)); filled symbols correspond to lowest mode cases where  $k_{\text{crit}} = 2$  and  $\lambda_{\text{crit}} = \pi a$ . (b) Surface patterns for different radius fibers with the same thickness  $t$  at  $E_c/E_s = 10^{-3}$  and  $E_c/E_s = 10^{-2}$ , showing wavelength ( $\lambda_{\text{crit}} = 41t$  and  $19t$  respectively) to be independent of fiber radius.

#### 4.2.5 Rationalization of Experimental Results

For dry-spinning processes like electrospinning where  $E_c/E_s$  is likely to be consistently very small, the buckling wavelength can be tailored by manipulating the thickness of the shell, which can be easily achieved by controlling solvent volatility. This is illustrated by a comparison of Figure 4-1(a) and Figure 4-1(c).  $E_c/E_s$  is believed to be similar for these two cases since the polymer, molecular weight, and polymer concentration are the same for these two systems. The only difference is the choice of solvent: THF, a low boiling point solvent used in the system for Figure 4-1(a), and DMF, a high boiling point solvent used in the system for Figure 4-1(c). Because THF evaporates more quickly than DMF, the thickness of the shell in Figure 4-1(a) is thicker than Figure 4-1(c), which manifests as the longer wavelength in Figure 4-1(a) compared to Figure 4-1(c).

Taking for instance the case of the beads-on-string morphology of Figure 4-1(d), if we assume that the thickness of the polymer shell is uniform along the entire bead-on-string structure, then the small diameter of the string region corresponds to a small  $a/t$  and hence a smooth surface results. Meanwhile, the diameter of the bead is about 10 times larger than that of the fiber. Thus, the larger  $a/t$  of the bead results in a wrinkled topography with a large  $k_{crit}$  (between 7 and 32 from the map, depending on the relative properties  $E_c/E_s$ ). (Here, the prolate spheroid geometry of the bead enabled use of the cylinder solution as an approximation to obtain the bead buckling conditions [5].) This is consistent with the experimental observation of  $k \sim 16$ .

Conversely, it should be possible to estimate the shell thickness, and hence to quantify the rate of solidification during the fiber forming process, from the mode number observed; a quantitative analysis to this effect, however, requires further experimental investigation. This effect can also be applied to core/shell fibers formed by co-axial electrospinning [16], where selection of the core and shell fluids can potentially be used to tailor the surface topography of fiber or beads.



### 4.3 Concluding Remarks

In conclusion, experimental, analytical and numerical studies were carried out to investigate the wrinkled surface topographies of electrospun polymer fibers. Wrinkled fibers can be viewed as 1-dimensional nanostructured materials. The wrinkled or patterned topographies act to increase the specific surface area and to texture the surface, providing avenues for enhancing various attributes and properties of fibers and fibrous mats. For example, the hydrophobic nature of nonwoven mats can be enhanced because wrinkling imparts a second, finer scale roughness on top of the curved fiber surfaces. Some wrinkled fiber topographies contain deep axial grooves, which can act as capillary channels or fluid conduits such as those used in liquid chromatography. Conformal coating and/or functionalizing using chemical vapor deposition (CVD) or layer-by-layer techniques can further enhance surface dominated properties [17]. Most of this chapter has been published in Ref. [18].

### 4.4 References

- [1] Pocivavsek L, Dellsy R, Kern A, Johnson S, Lin B, Lee KYC, Cerda E. "Stress and fold localization in thin elastic membranes", *Science* 2008; 320: 912.
- [2] Khang DY, Jiang H, Huang Y, Rogers JA. "A stretchable form of single-crystal silicon for high-performance electronics on rubber substrates", *Science* 2006; 311: 208.
- [3] Wang S, Song J, Kim DH, Huang Y, Rogers JA. "Local versus global buckling of thin films on elastomeric substrates", *Appl. Phys. Lett.* 2008; 93: 023126.
- [4] Cao G, Chen X, Li C, Ji A, Cao Z. "Self-assembled triangular and labyrinth buckling patterns of thin films on spherical substrates", *Phys. Rev. Lett.* 2008; 100: 036102.
- [5] Yin J, Cao Z, Li C, Sheinman I, Chen X. "Stress-driven buckling patterns in spheroidal core/shell structures", *Proc. Natl. Acad. Sci. U.S.A.* 2008; 105: 19132.
- [6] Newell AC, Shipman PD, Sun Z. "Phyllotaxis: Cooperation and competition between mechanical and biochemical processes", *J. Theor. Biol.* 2008; 251: 421.

- [7] Koombhongse S, Liu W, Reneker DH. "Flat polymer ribbons and other shapes by electrospinning", *J. Appl. Polym. Sci. Part B: Polym. Phys.* 2001; 39: 2598.
- [8] Pai CL, Boyce MC, Rutledge GC. "Morphology of Porous and Wrinkled Fibers of Polystyrene Electrospun from Dimethylformamide", *Macromolecules* 2009; 42: 2102.
- [9] Pauchard L, Allain C. "Stable and unstable surface evolution during the drying of a polymer solution drop", *Phys. Rev. E* 2003; 68: 052801.
- [10] Pauchard L, Allain C. "Buckling instability induced by polymer solution drying", *Europhys. Lett.* 2003; 62: 897.
- [11] Pauchard L, Couder Y. "Invagination during the collapse of an inhomogeneous spheroidal shell", *Europhys. Lett.* 2004; 66: 667.
- [12] Herrmann G, Forrestal MJ. "Buckling of a long cylindrical shell containing an elastic core", *AIAA Journal* 1965; 3: 1710.
- [13] Seide P. "The stability under axial compression and lateral pressure of circular-cylindrical shells with a soft elastic core", *J. Aerospace Sci.* 1962; 29: 851.
- [14] Cerda E, Mahadevan L. "Geometry and physics of wrinkling", *Phys. Rev. Lett.* 2003; 90: 074302.
- [15] ABAQUS/Standard users' manual version 6.6. Providence, RI: ABAQUS Inc., 2006.
- [16] Yu JH, Fridrikh SV, Rutledge GC. "Production of submicrometer diameter fibers by two-fluid electrospinning", *Adv. Mater.* 2004; 16: 1562.
- [17] Ma M, Gupta M, Li Z, Zhai L, Gleason KK, Cohen RE, Rubner MF, Rutledge GC. "Decorated electrospun fibers exhibiting superhydrophobicity", *Adv. Mater.* 2007; 19: 255.
- [18] Wang LF, Pai CL, Boyce MC, Rutledge GC. "Wrinkled surface topographies of electrospun polymer fibers", *Appl. Phys. Lett.* 2009; 94(15): 151916.

## **Chapter 5 Mechanical Properties of Individual Electrospun Polymer Fibers and Their Variation with Fiber Diameter**

### **5.1 Introduction**

Over the past decade, several research groups have reported remarkable enhancements in mechanical properties of electrospun polymeric fibers, relative to their bulk values, for fibers below a critical diameter, typically in the submicron range [1-14]. Different techniques have been developed to overcome the difficulties of sample preparation and handling of such small fibers; among these are direct tensile testing using a small load cell and special gripping techniques [1-2,15], nanoindentation where the loading-unloading behavior of load-depth curves are reduced using models, such as the Oliver and Pharr model [16], to estimate modulus [3], 2-point and 3-point bending tests using atomic force microscopy (AFM) and simple beam theory [4-9], and the resonance test using a piezoelectric actuator to drive a mechanical oscillation under microscopy [10]. Typically, when the fiber diameter drops below one micron, the Young's modulus is found to increase with decreasing fiber diameter, with the Young's modulus of the smallest electrospun polymeric fibers being larger than that of the bulk material [1, 3, 4, 6, 8, 12, 26]. This phenomenon has been found in different polymers, such as polypyrrole nanotubes [4], polyethylene oxide (PEO) [6], polystyrene (PS) [3], poly( $\epsilon$ -caprolactone) (PCL) [1], Nylon 6 [8], Nylon 6/6 [12], and poly(vinyl alcohol) (PVA) [26].

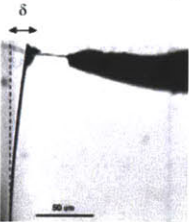
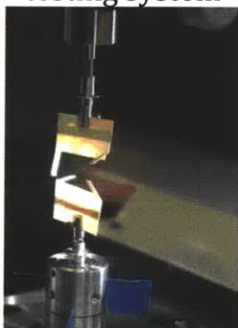
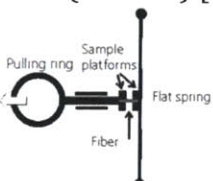
It is worth noting that some studies did not obtain the modulus of the bulk material, but only compared the moduli of fibers of different diameters. In some instances the largest fibers exhibited moduli that were inferior to that of the bulk material; these inferior fiber moduli were attributed to such diverse factors as shear deformation during bending [5], fiber plasticization by atmospheric moisture [7], or reduced density within the fiber arising from vapor-induced phase separation during fiber formation [11]. Nevertheless, the reported enhancement in the Young's modulus with decreasing diameter of fully dense submicron electrospun fibers is very promising and still requires explanation.

## 5.2 Different Techniques for Mechanical Measurement of Single Fibers

Different methods for measuring the mechanical properties of an electrospun nanofiber have been proposed and several publications have appeared in the past few years, as can be seen from Table 5-1 to Table 5-4. Generally speaking, these methods have been developed first for measuring the mechanical properties of nanotubes and metal wires; however, they are also suitable for electrospun nanofibers. They can be classified into four categories: tensile tests (Table 5-1), nanoindentation (Table 5-2), bending tests (Table 5-3), and resonance tests (Table 5-4). We have tried all but the resonance tests to see which method works best for small fibers. We started from commercial fibers with known mechanical properties to make sure the characterization is correct, followed by testing large electrospun fibers to see if their properties approach to the bulk material. Finally, the small electrospun fibers with unknown properties were tested.

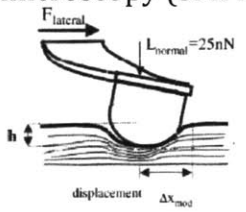
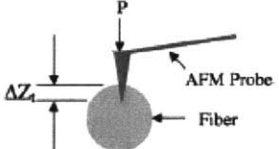
Among all these tests, the tensile test is the most direct way to measure mechanical properties. In addition to Young's elastic modulus, a tensile test also measures a yield stress, an ultimate tensile strength, and an elongation to failure. The actual gripping and handling of the fiber are major issues in conducting a reliable tensile test. Challenges to address includes: gripping the fiber on the template without slip and stress concentration; aligning the fiber without inducing off-axis loading such as torsion are two issues that require special care during the measurement. Also, it is difficult to handle a single fiber when it is invisible to the naked eye. With the aid of proper lighting, we can handle fiber diameter down to around 100 nm. Table 5-5 shows our preliminary results by using UTM T150 universal tensile testing system for commercial fibers (Kevlar and Nomex fiber with the fiber diameter larger than 10  $\mu\text{m}$ ) and electrospun fibers of different polymers. Although the UTM T150 universal tensile testing system claims the load resolution is 50 nN, the noise level during the measurement can approach 1  $\mu\text{N}$ , which limits the usage of this instrument on very small fibers.

Table 5-1. Mechanical properties of a single electrospun fiber by the tensile test

Method	Materials	d (nm)	Properties	Author
AFM cantilever [13] 	PAN-derived carbon	70 ~ 500	$\sigma_{UTS} = 350 \sim 1000$ MPa	[6] Zussman E, 2005
	Nylon 6/6 (PA 6/6)	400 ~ 900	$E_r = 1 \sim 3.25$	[12] Arinstein A, 2007
	PA 6/6	550	$E_f = 0.45 \sim 0.95$ GPa $\sigma_{UTS} = 110 \sim 150$ MPa Elongation = 61 ~ 66%	[13] Zussman E, 2005
	PAN	1250	$\sigma_{UTS} = 302$ MPa	[17] Buer A, 2001
	Poly(ethylene oxide) (PEO)	700	$E_f = 45$ MPa	[18] Tan EPS, 2005
UTM T150 universal tensile testing system 	Poly( $\epsilon$ -caprolactone) (PCL)	200 ~ 5000	$E_f = 0.3 \sim 3.2$ GPa $\sigma_{UTS} = 20 \sim 200$ MPa Elongation = 20 ~ 300 %	[1] Chew SY, 2006
	Poly(caprolactone-co-ethylene phosphate) (PCLEEP)			
	PCL	400 ~ 2600	$E_f = 0.35$ GPa	[2] Wong SC, 2008
	Poly(L-lactide) (PLLA)	610 ~ 890	$E_f = 1.0 \sim 2.9$ GPa $\sigma_{UTS} = 89 \sim 183$ MPa Elongation = 0.45 ~ 1.54 %	[19] Inai R, 2005
Microelectronic mechanical systems (MEMSs) [14] 	PCL	1030 ~ 1700	$E_f = 0.12$ GPa $\sigma_{UTS} = 40$ MPa Elongation = 200 %	[20] Tan EPS, 2005
	PLLA	150 ~ 2000	$E_f = <1 \sim 7$ GPa	[14] Jaeger D, 2009

Note that  $E_f$  is the Young's modulus of a single fiber,  $\sigma_{UTS}$  is the ultimate tensile strength of a single fiber,  $E_r$  is  $E_f/E_{bulk}$ , where  $E_{bulk}$  is the modulus of the bulk material.

Table 5-2. Mechanical properties of a single electrospun fiber by nanoindentation

Method	Materials	d (nm)	Properties	Author
Shear modulation force microscopy (SMFM) [3]  $h = \left( \frac{3(1-\nu)L}{8GR^{1/2}} \right)^{2/3} *$	PS/MMT clays (Cloistie-6A)	150 ~ 4000	surface shear modulus: 1.22 ~ 3.7 times larger than the bulk value	[3] Ji Y, 2006
AFM [22]  $S = \left. \frac{dP}{dh} \right _{P=P_{max}} = \frac{2}{\sqrt{\pi}} \sqrt{AE^*} **$ $\frac{1}{E^*} = \frac{1-\nu_s^2}{E_s} + \frac{1-\nu_t^2}{E_t}$	B. mori silk/PEO	800	$E_f = 0.75 \sim 8.0$ GPa	[21] Wang M, 2004
	Fe <sub>3</sub> O <sub>4</sub> /PEO Fe <sub>3</sub> O <sub>4</sub> /polyvinyl alcohol (PVA)	400 140 ~ 320	$E_f = 0.66 \sim 1.04$ GPa $E_f = 4.1 \sim 4.8$ GPa	[22] Wang M, 2004
	PAN/Graphite nanoplatelets (GNPs)	5 ~ 500	modulus increases 2 times with different wt% fillers	[23] Mack JJ, 2005
	PAN/SWNT-derived carbon	50 ~ 200	$E_f = 60 \sim 130$ GPa	[24] Ko F, 2003

Note that  $E_f$  is the Young's modulus of a single fiber.

\* $h$  is the tip penetration into an elastic substrate,  $\nu$  is the Poisson's ratio,  $G$  is the shear modulus, and  $L$  is the load applied to the tip, and  $R$  is the tip radius.

\*\* $P$  is the applied load,  $h$  is the indentation depth,  $A$  is the contact area,  $E^*$  is the effective Young's modulus,  $E_s$  and  $E_t$  are the elastic moduli of sample and the tip,  $\nu_s$  and  $\nu_t$  are the Poisson ratios of the sample and the tip.

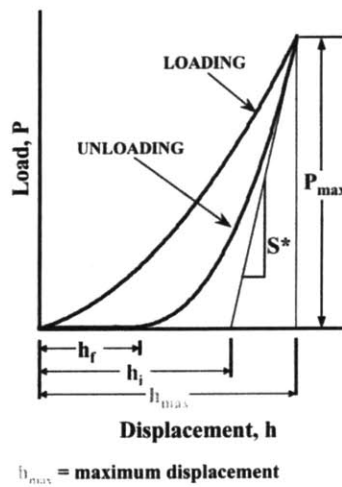
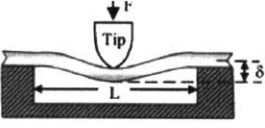
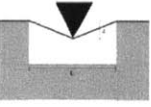
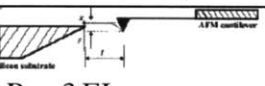
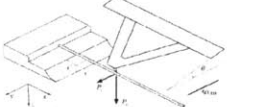


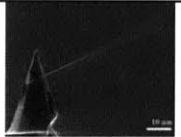
Figure 5-1. Important Parameters in Oliver and Pharr's model [16].

Table 5-3. Mechanical properties of a single electrospun fiber by AFM bending test

Method	Materials	d (nm)	Properties	Author
AFM [5]  $\frac{P}{\delta} = \frac{192EI}{L^3}$	Polypyrrole nanotubes	$d_{out} = 35 \sim 160^*$	$E_f = 1.2 \sim 60$ GPa	[4] Cuenot S, 2000
	PLLA	260 ~ 410	$E_f = 0.1 \sim 1.0$ GPa	[5] Tan EPS, 2004
	Poly(2-acrylamido-2-methyl-1-propanesulfonic acid) (PAMPS)	60 ~ 250	$E_f = 0.3 \sim 2.1$ GPa	[7] Shin MK, 2006
	TiO <sub>2</sub>	38 ~ 72	$E_f = 52 \sim 125$ GPa	[25] Lee SH, 2005
	TiO <sub>2</sub> /poly(vinyl pyrrolidone) (PVP)	68 ~ 148	$E_f = 0.33 \sim 2.33$ GPa	
	Poly(vinyl alcohol)(PVA)	10 ~ 160	$E_f = 20 \sim 500$ GPa (higher than expected.)	[26] Fu Q, 2010
The small deflection approximation [6]  $P = 8AE(\delta/L)^3$	PEO	70 ~ 450	$E_f = 7$ GPa	[6] Bellan LM, 2005
	Polysiloxane/PVP	100 ~ 300	$E_f = 24$ GPa	
	Silica glass	70 ~ 250	$E_f = 240$ GPa	
 $\frac{P}{\delta} = \frac{3EI}{L^3}$	Nylon 6	70 ~ 150	$E_f = 15 \sim 30$ GPa	[8] Li L, 2006
	Nylon 6/MMT clays (Cloistie-30B)		$E_f = 15 \sim 100$ GPa	
	PAN	179 ~ 408	$E_f = 3.79 \sim 47.79$ GPa (higher than expected.)	[27] Gu SY, 2005
	Silica nanowires	281 ~ 1948	$E_{vertical} = 68 \sim 76$ GPa $E_{in-plane} = 105$ GPa	[28] Silva ECCM, 2006

Note that  $E_f$  is the Young's modulus of a single fiber,  $d_{out}$  is the outer diameter of the nanotube,  $I = \pi d^4 / 64$  for a circular nanofiber,  $P$  is the applied load,  $\delta$  is the deflection of the nanofiber,  $E$  is the Young's modulus,  $d$  is the diameter of the nanofiber,  $L$  is the length of the nanofiber, and  $A$  is the cross-sectional area of the nanofiber.

Table 5-4. Mechanical properties of a single electrospun fiber by resonance test

Instrument	Method	Materials	d (nm)	Properties	Author
Piezoelectric actuator and SEM	 Ref.[10] $f_n = \frac{\beta_n^2 d}{2\pi L^2} \sqrt{\frac{E}{16\rho}}$	PAN-derived carbon ( $\beta_1 = 1.875$ )	100 ~ 200	$E_f = 57 \sim 75$ GPa	[10] Zussman E, 2005
Resonators and laser interference		Silica glass ( $\beta_1 = 4.73$ )	120	$E_f = 266$ GPa	[29] Craighead HG, 2004

Note that  $E_f$  is the Young's modulus of a single fiber,  $I = \pi d^4 / 64$  for a circular nanofiber,  $E$  is the Young's modulus,  $d$  is the diameter of the nanofiber,  $L$  is the length of the nanofiber,  $\beta_n$  is the eigenvalue, and  $\rho$  is the material density.

Table 5-5: Preliminary results by UTM T150 universal tensile testing system

Single Fiber Tensile Testing		Polymer System	Fiber Diameter ( $\mu\text{m}$ )	Strain rate (1/s)	Modulus (GPa)	Elongation (%)	Tensile Strength (MPa)	Toughness (MPa)
Commercial		Kevlar 29	11.2(4%)	$10^{-4}$	98.2(10%)	4.4(12%)	4116(15%)	93(28%)
		Nomex	16.3	$5 \times 10^{-3}$	10.9(8%)	38(9%)	402(13%)	120(19%)
Electrospun	Nomex	20wt% Nomex /DMAc/5wt%LiCl	0.26(10%)	$10^{-3}$	4.2(44%)	20(32%)	435(19%)	51(25%)
		25wt% Nomex /DMAc/5wt%LiCl	0.77(20%)	$10^{-3}$	6.5(31%)	33(40%)	474(31%)	88(35%)
	PMMA	PMMA	3.93	$10^{-3}$	2.9(10%)	4.9(54%)	53(9%)	2 (70%)
		PMMA	2.58(8%)	$10^{-3}$	3.3(11%)	3.2(16%)	56(11%)	1.2(26%)
		PMMA/2.5wt.% Cloisite™ 20A	2.40(4%)	$10^{-3}$	3.9(10%)	3.4(16%)	62(8%)	1.5(22%)
		PMMA/2.5wt.% methacryl-tethered clay	2.71(5%)	$10^{-3}$	3.7(12%)	3.6(24%)	62(9%)	1.6(34%)
	PC	15wt% PC/Chloroform	3.7(65%)	$10^{-3}$	2.6(29%)	53(56%)	272(36%)	86(30%)
	Nylon	10wt% Nylon 6/6/HFIP	0.62(8%)	$10^{-3}$	2.0(16%)	22(30%)	334(11%)	44(34%)
	PAN	12wt% PAN/DMF	1.23(8%)	$10^{-3}$	2.7(6%)	78(39%)	54(6%)	38(37%)
		12wt% PAN/DMF (Gauge length 4mm)	1.23(4%)	$10^{-3}$	2.6(13%)	90(25%)	57(7%)	48(23%)
		12wt% PAN/DMF (anneal 90°C, 15mm)	1.10(5%)	$10^{-3}$	5.3(23%)	12(55%)	90(9%)	9(56%)
		12wt% PAN/DMF (anneal 90°C, 4mm)	1.05(4%)	$10^{-3}$	4.3(8%)	30(98%)	86(2%)	24(105%)
		10wt% PAN/DMF	0.39(17%)	$10^{-3}$	4.9(55%)	18(114%)	124(40%)	14(97%)
		10wt% PAN/DMF (anneal 90°C)	0.36(13%)	$10^{-3}$	4.5(28%)	15(24%)	137(22%)	14(20%)

*The parenthesis corresponds to one standard deviation due to the variation between samples. The large standard deviation of fiber diameter in 15wt% PC/Chloroform came from the unstable electrospinning when a low boiling point solvent was used.*

Nanoindentation is the simplest technique with respect to sample preparation. We can perform nanoindentation loading into either the elastic regime or the elastic-plastic regime of behavior. Various data reduction schemes have been utilized to reduce the load-depth curves to useful mechanical property data of modulus and yield strength. A popular method is the Oliver-Pharr method [16]. Important parameters for this method are shown in Figure 5-1, and equations are listed in Table 5-2. We performed the nanoindentation on commercial Nomex fibers, standard PP fibers, and electrospun PAN fibers. Their force-deformation curves are shown in Figure 5-2. The modulus of the fiber can be derived from the curve with known contact area, the Poisson's ratio of the fiber and the tip, and the modulus of the tip. However, it is hard to determine the contact area between the tip and the



sample due to the uncertainties of both the contact radius and the exact shape of the tip. An equation [16] was used to estimate the contact area by assuming a perfect Berkovich indenter:  $A(h_c) = 24.5h_c^2$ , where  $h_c = h_{\max} - \varepsilon_{tg} P_{\max} / S$ ,  $\varepsilon_{tg}$  is the function of the particular tip geometry, and  $S$  is the indent size. The indent size can be derived from the indent mark on fibers, as shown in Figure 5-3. Other concerns for the nanoindentation are that it measures mainly local and surface properties, and requires the surface to be relatively flat compared to the tip curvature. Also, some unexpected aspects in experimental approaches might affect the apparent results, such as the Tweedie et al.'s discovery [30] of different trend of stiffness for varied indentation depth from free surface. Finite element analysis of the indentation process is increasingly useful to provide more accurate estimation of properties.

Bending tests, either 2-point or 3-point bending tests, are conducted utilizing AFM. For 3-point bending tests, nanofibers must be suspended over trenches, restrained at the ends and then centrally loaded. Generally speaking, investigators perform bending tests on a single electrospun nanofiber with two clamped ends and then measure the deflection when the fiber is subjected to a small force. By applying simple beam theory, the data can be reduced to an elastic modulus.

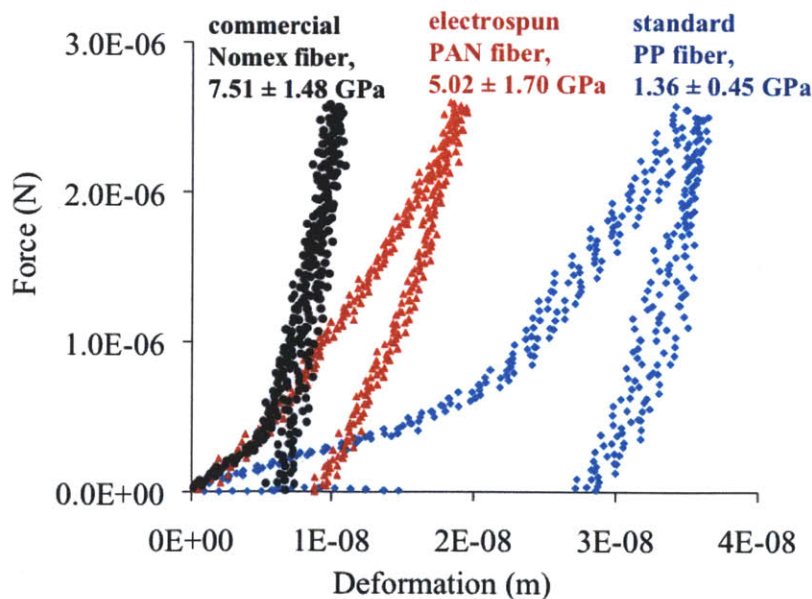


Figure 5-2. The force-deformation curves of nanoindentation measured by AFM and the corresponding elastic modulus of the fiber.

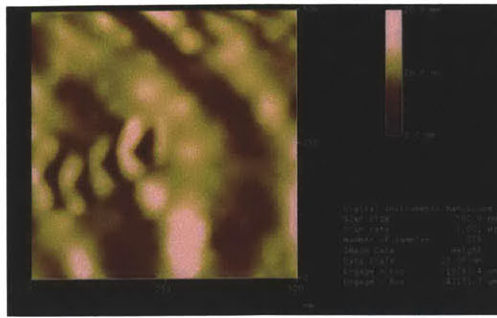


Figure 5-3. Four indentations on a Nomex fiber.

The difficulty of bending tests lies in the sample preparation as well as the measurement. How to place a single fiber over a trench and restrain the ends is a difficult task due to the small size of the sample. Also, it is easy to break the fiber during the imaging process or the force mode if the set point (determine how the tip approaches the fiber) of the AFM tip is not well controlled. Microelectronic mechanical systems (MEMS) technology can be utilized to construct the trench structure (e.g. micro-scale groove on the silicon wafer). Fibers are then carefully placed and secured with epoxy. Some typical conditions happened during the 3-point bending test and sample preparation are shown in Figure 5-4.

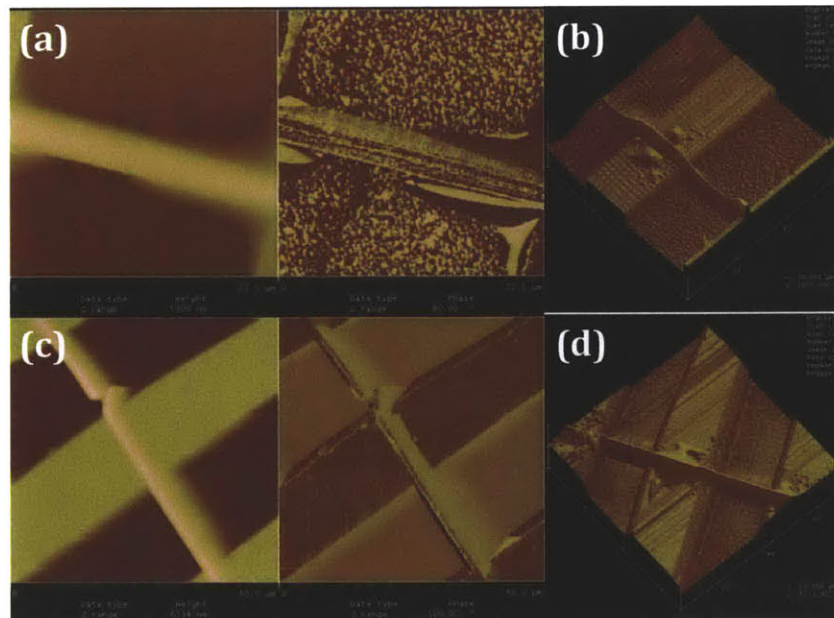


Figure 5-4. AFM images show that (a) epoxy diffused along the fiber; (b) the fiber

cannot sustain itself and fell on the trench; (c) the fiber was damaged during the image scanning; and (d) a fiber was carefully placed and secured with epoxy.

Another possible way to measure the mechanical properties of a single fiber is the resonance test. Typically, a piezoelectric actuator is used to drive a mechanical oscillation in the fiber. If the sample is conductive, for example, the oscillation can be driven by electric force under transmission electron microscope (TEM). The modulus-frequency relationship is described using Bernoulli-Euler beam theory, describing flexural motion of a linear elastic beam. The corresponding frequency

equation is:  $f_n = \frac{\beta_n^2}{2\pi L^2} \sqrt{\frac{EI}{\rho A}}$  ( $n$ : mode number,  $\beta_n$ : eigenvalue for  $n$ th mode,  $L$ : length

of the beam,  $E$ : modulus,  $I$ : moment of inertia of beam cross-section,  $\rho$ : material density,  $A$ : cross-sectional area of the beam). The eigenvalue depends on the boundary conditions. For a fixed-free cantilever beam, the fundamental mode  $\beta_1 = 1.875$ , whereas for a free-free beam,  $\beta_1 = 4.73$ . The difficulties of resonance tests are to prepare the integrated system of sample and actuator, and to apply suitable frequency and then determine the mode of resonance.

### 5.3 Results and Discussion

However, studies to date either cover a limited range of fiber diameter, or are complicated by variations in crystallinity or molecular orientation with fiber diameter, both of which may contribute to the enhanced stiffness of small fibers. It is hard to clarify each contribution, such that their relative importance to the enhancement remains unresolved. In this work, we have chosen to simplify the issue by studying PA 6(3)T, which does not crystallize and can be formed by electrospinning into fibers over a wide range of average fiber diameter. Our experiments reveal a clear dependence of modulus and strength of PA 6(3)T fibers on the diameter of the fibers, and explain it in terms of increased molecular orientation with decreasing fiber diameter. We also report the yield strength variation with fiber diameter.

PA 6(3)T was readily electrospun into a wide range of fiber diameters ( $d$ ), from 170 nm to 3600 nm, as shown in Figure 5-5. Detailed electrospinning conditions are listed in Table 5-6. As demonstrated by Figure 5-5, all of the fibers employed in this work were smooth and regular in structure. Cross-sectional images of the fibers in SEM in Figure 5-6 confirmed that the fibers are nonporous and consolidated. Figure 5-7 shows engineering stress-strain curves of uniaxial tensile testing for four representative individual fibers. As can be seen, smaller diameter fibers tend to have higher Young's moduli and yield strengths, and to break at smaller strains, than larger diameter fibers.

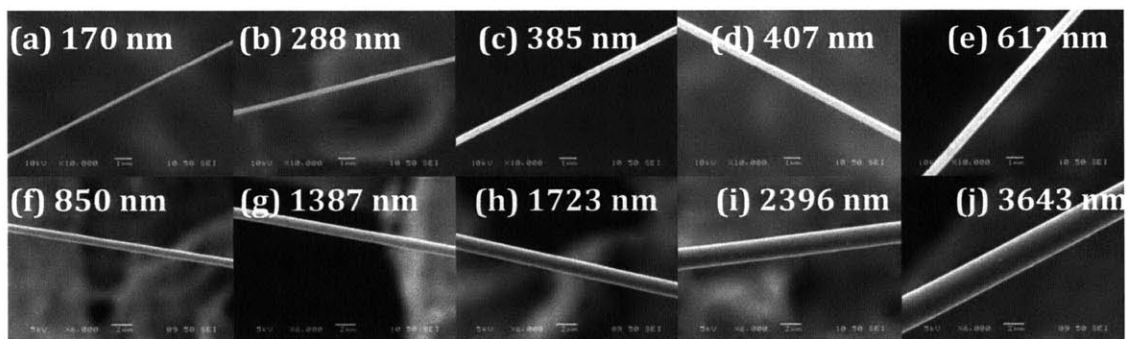


Figure 5-5. SEM images of individual PA 6(3)T fibers with different average diameters. Images (a) through (e) were taken under 10,000x magnification (scale bar = 1  $\mu$ m), while images (f) through (l) were taken under 6000x magnification (scale bar = 2  $\mu$ m).

Table 5-6: Processing parameters of electrospinning and resulting fiber diameter.

wt %	solvent	Q (ml/min)	V (kV)	D (cm)	$E_{\infty}$ (kV/cm)	I (nA)	d (mm)
22	DMF/FA	0.002	35	42	0.83	131	0.17 $\pm$ 0.026
28	DMF/FA	0.002	36.5	33	1.11	272	0.288 $\pm$ 0.027
30	DMF/FA	0.002	34	33	1.03	442	0.385 $\pm$ 0.039
28	DMF/FA	0.01	40	33	1.21	1470	0.407 $\pm$ 0.055
30	DMF/FA	0.01	40	33	1.21	1227	0.612 $\pm$ 0.054
30	DMF	0.002	30	38	0.79	25	0.85 $\pm$ 0.088
30	DMF	0.01	32	38	0.84	96	1.387 $\pm$ 0.128
30	DMF	0.05	40	38	1.05	626	1.723 $\pm$ 0.464
36	DMF	0.01	34	53.5	0.64	205	2.396 $\pm$ 0.093
36	DMF	0.05	40	53.5	0.75	433	3.643 $\pm$ 0.070

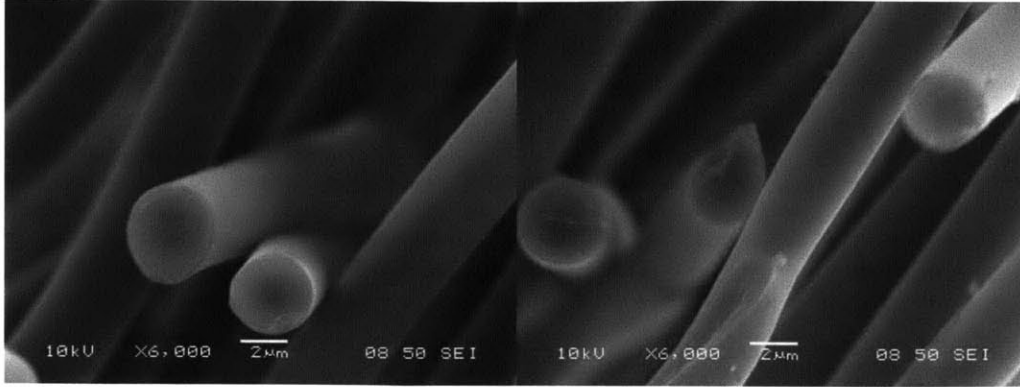


Figure 5-6. Cross-sectional images of the PA 6(3)T fibers cut under liquid nitrogen to confirm the nonporous and consolidated structures. SEM images were taken under 6,000x magnification (scale bar = 2  $\mu\text{m}$ ).

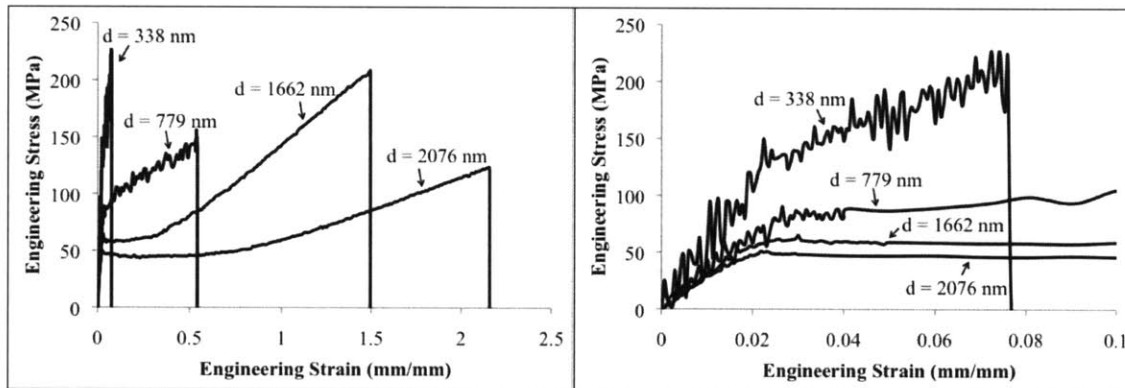


Figure 5-7. Representative stress-strain curves of individual fibers. The figure on the right hand side accentuates the small engineering strain of the figure on the left hand side.

Figure 5-8 shows the Young's modulus and yield strength versus the fiber diameter, obtained from the stress vs strain data for individual fibers deformed. Each diamond represents a single fiber measurement; the error bar corresponds to one standard deviation, due to variation in diameter of the fiber along its length as well as measurement error in the SEM, which affects the calculated stress. Yield was found to occur at strains around 0.025 for these fibers. Our results show that both Young's modulus and yield strength increase as fiber diameter decrease. Yuan and Ruckenstein have reported [31] values of 1.0 GPa and 50 MPa for the Young's

modulus and yield strength, respectively, for pure PA 6(3)T films. The average and standard deviation of Young's modulus and the yield strength measured for the films we made were  $1.99 \pm 0.34$  GPa and  $43.7 \pm 14.9$  MPa, respectively as shown by the horizontal lines in Figure 5-8. Although there is some discrepancy in the Young's modulus and yield strength reported for the isotropic bulk material, our results show that both Young's modulus and yield strength of the largest fibers are at least as large as those of the bulk films, while the Young's modulus and yield strength of the smallest fibers exceed these values by 2 to 3 fold.

We use T-test to analyze the statistical significance of the Young's modulus of Figure 5-8(a) to two groups: one with small fiber diameter ( $< 839$  nm), and the other with large fiber diameter ( $> 839$  nm). Each group has 61 measurements. We used two tails and type 1 in T-test, and analyze two groups at their mean value of Young's modulus, their upper bound (the mean value + one standard deviation), and their lower bound (the mean value - one standard deviation). The results are as followings:

p-value for the mean value:  $2.95 \times 10^{-7}$ .

p-value for the upper bound:  $1.25 \times 10^{-5}$ .

p-value for the lower bound:  $3.22 \times 10^{-6}$ .

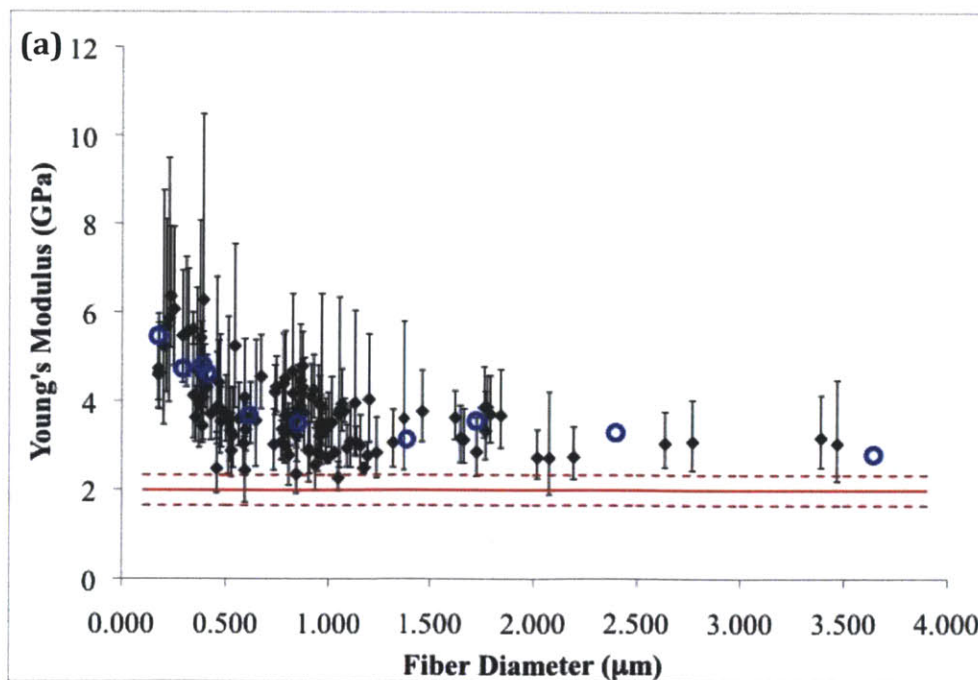
All p-values are far smaller than 0.05, which suggest the statistical significance between two groups. The result supports our conclusion that smaller fibers have different Young's modulus from the bulk value.

Another way to further analyze Figure 5-8(a) and to clear the possibility of due to chance for the Young's modulus of the smallest fibers to exceed bulk materials is to do the moving average on the relation of the Young's modulus of these fibers to their fiber diameter. We perform a moving average over 11-point, 21-point, 31-point, 41-point, and 51-point of data for individual fibers with different fiber diameters, and a weighted moving average (zeroth-order locally weighted regression) using a common tri-cube function  $(1-|x|^3)^3$  over 10%, 20%, and 50% of data for individual fibers with different fiber diameters (the number of total measurements is 123), as shown in Figure 5-8(c). We conclude the Young's modulus of the smallest fibers is different and larger than that of the largest fibers. This

apparent trend is unlikely to be due to chance alone. These analyses are sufficient for the nonlinear trends that appear in our results of the Young's modulus vs. fiber diameter, and additional bootstrap re-sampling method is not needed here.

Polarized FTIR was used to measure the dichroism of the stretching mode of the amide carbonyl peak (C=O) around  $1640\text{ cm}^{-1}$  [32], as shown in Figure 5-8. The stretching mode of the C=C bond in the phenyl ring is around  $1610\text{ cm}^{-1}$ , which overlaps with the C=O bond in which we are interested. To deconvolute these two peaks in the FTIR spectrum, a Gaussian function was used to describe each peak, and their sum was fit to the experimental data in the range of  $1585$  to  $1678\text{ cm}^{-1}$ . Note that we clear the possibility of the fringing effect in Chapter 2 (p.21-22).

The absorbance curves of the parallel polarization of  $d = 3643\text{ nm}$  and  $170\text{ nm}$  are used to demonstrate the two deconvoluted peaks, as shown in thin solid lines in Figure 5-9(a). The absorbance, determined from the area under the C=O peak, was obtained for polarization of the incident beam both parallel and perpendicular to the fiber axis, from which the dichroic ratio,  $D$ , was calculated. The overall molecular orientation,  $f_2$ , was calculated from Equation (2-1), and is listed in Table 5-7.



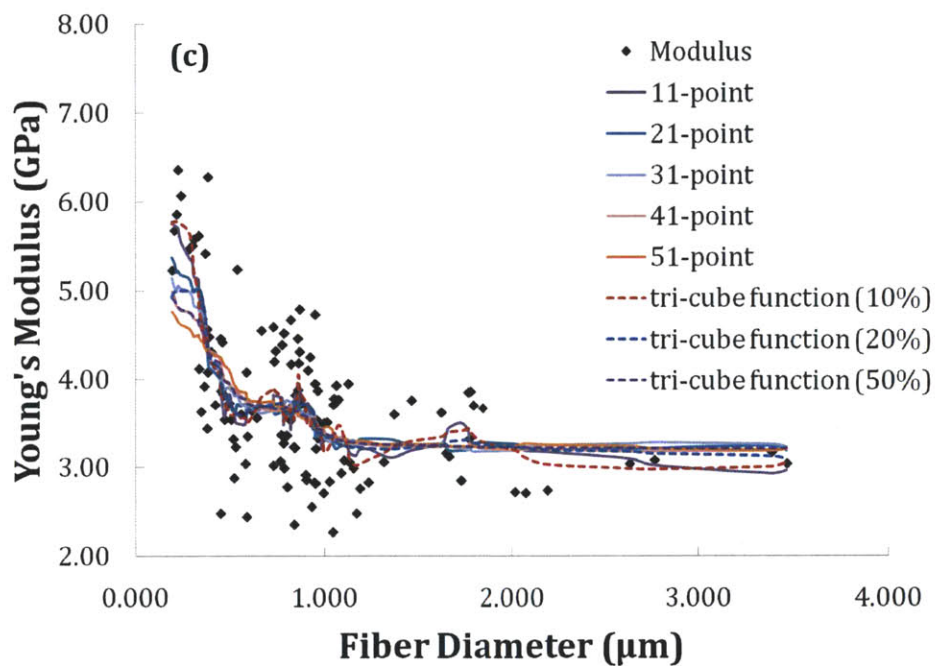
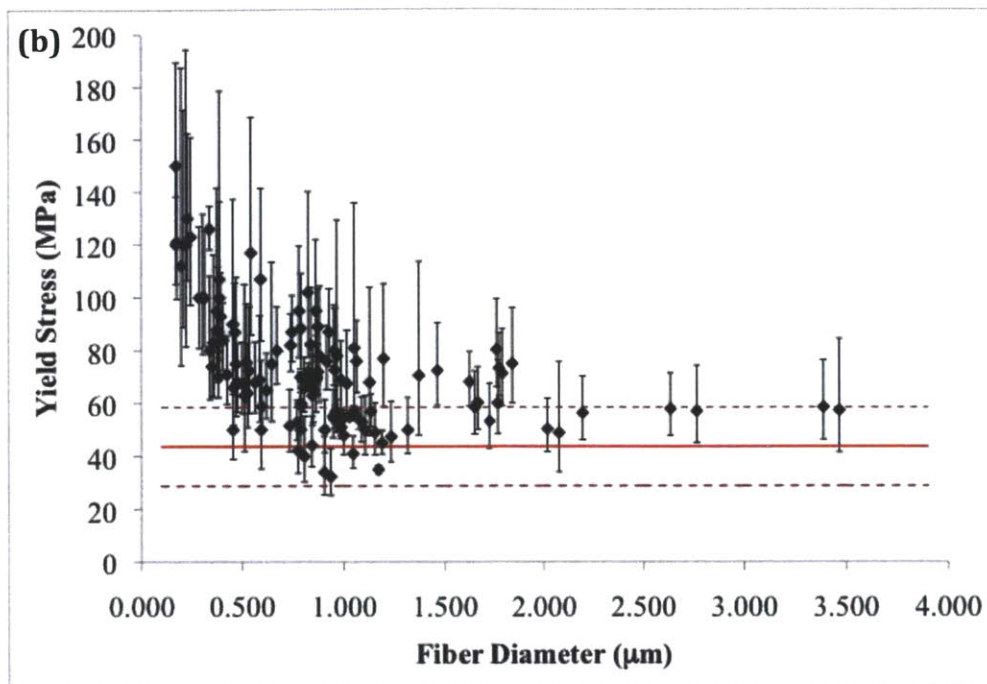


Figure 5-8. Dependence of (a) Young's modulus and (b) yield stress on fiber diameter. Filled diamonds represent experimental data for individual fibers deformed in uniaxial extension; open circles represent values obtained from molecular orientation measurements using Ward's aggregate model [41]; solid lines represent our experimental values for bulk films; dashed lines represent one standard deviation. (c) The moving average on Figure 5-8(a).



The molecular orientation increases with decreasing fiber diameter, as seen in Figure 5-9(b). It should be noted that this trend cannot be attributed to differences in degree of alignment of fibers within a bundle, whose trend with fiber diameter is opposite to this, as shown in Figure 5-10. The orientation distribution of fibers within bundles was determined by image analysis of SEM images [33], as shown in Figure 5-10(a) ~ (c), using the method of Tzeranis [34]. The representative results are plotted in Figure 5-10(d) ~ (f). The increase in molecular orientation with decreasing fiber diameter can account for the observed dramatic increase of the fiber stiffness and yield strength. Additional supporting evidence is provided by the shift of the C=O peak to higher wavenumber for the smaller fibers; such shifts have been attributed to higher orientation [35] or to residual molecular strain within the fibers [36-37]. Both of these interpretations are consistent with a freezing in of a higher level of molecular deformation and orientation in the smaller diameter fibers compared to the larger diameter fibers. The observation of greater molecular deformation in the smaller fibers may be indicative of several phenomena at work in the electrospinning jet. The first is that the electrical shear stress operative on the surface of the jet is responsible for such molecular deformation and affects a larger fraction of the jet when the diameter is small due to the higher ratio of surface area to volume. A second is that the smaller fibers are the result of larger growth amplitude of the whipping instability, thus resulting in higher drawing ratio and better molecular orientation in fibers. The Hencky strain,  $\varepsilon$ , defined below [38], from the spinning process was calculated and listed in Table 5-7 as a rough indicator of spinning-induced extension.

$$\varepsilon = 2 \ln \left( \frac{h_0}{h_{mid}(t)} \right) \quad (5-1)$$

where  $h_0$  is the initial diameter of the unstretched fluid filament, which was assumed to be 100  $\mu\text{m}$  in our electrospinning system [39].  $h_{mid}(t)$  is a time-dependent diameter of the stretched fluid filament. For the total Hencky strain, we estimate  $h_{mid}(t)$  using the as-spun fiber diameter divided by the square root of the polymer concentration, to approximate the final jet diameter before evaporation of solvent [40]. The resulting strain is higher for smaller fibers. The third phenomenon

at work is the more rapid solidification of the smallest diameter jets due to solvent evaporation; molecular relaxation in incompletely solidified fibers has less time to act in the small fibers compared to the large fibers.

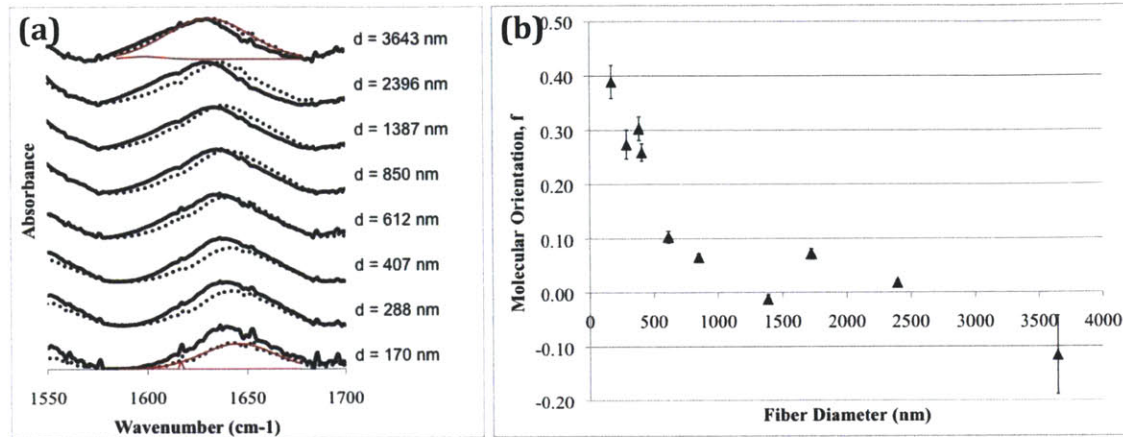


Figure 5-9. (a) Polarized FTIR of representing PA 6(3)T single fiber with different diameters. Solid lines represent  $A_{\perp}$ , and dotted lines represent  $A_{\parallel}$ . (b) The overall molecular orientation versus the fiber diameter.

Table 5-7: Data for Ward's Aggregate Model

$d$ ( $\mu\text{m}$ )	$\varepsilon$	$D$	$f_2$	$\langle \sin^4\Omega \rangle$	$\langle \cos^4\Omega \rangle$	$E_0$ (GPa)
0.170	12.8	0.59	0.39	0.17	0.35	5.46
0.288	11.7	0.70	0.27	0.23	0.27	4.73
0.385	11.1	0.67	0.30	0.22	0.29	4.80
0.407	11.0	0.71	0.26	0.24	0.26	4.62
0.612	10.2	0.88	0.10	0.36	0.16	3.68
0.850	9.5	0.92	0.07	0.39	0.14	3.51
1.387	8.6	1.01	-0.01	0.46	0.11	3.14
1.723	8.1	0.91	0.07	0.38	0.15	3.55
2.396	7.5	0.98	0.02	0.43	0.12	3.29
3.643	6.6	1.15	-0.12	0.55	0.07	2.80

Input data:  $S_{11} = 0.544$ ,  $S_{33} = 0.07$ ,  $S_{13} = -0.035$  (or  $\nu_{13} = 0.5$ ), and  $S_{44} = 0.341$ .

The observed anisotropy of fiber modulus can be related to the measured orientation distribution through Ward's single-phase aggregate model [41]. This

model represents the fiber as an aggregate of identical, anisotropic structural “units” that are dispersed at different orientations within the fiber. In this case, the anisotropic structural unit is considered to be a short segment of PA 6(3)T, on the order of a single repeat unit, whose orientation is measured by FT-IR. Using the aggregate model, the Young’s modulus along the fiber direction ( $E_0$ ) is given by:

$$\frac{1}{E_0} = \langle \sin^4 \hat{\Omega} \rangle S_{11} + \langle \cos^4 \hat{\Omega} \rangle S_{33} + \langle \sin^2 \hat{\Omega} \cos^2 \hat{\Omega} \rangle (2S_{13} + S_{44}) \quad (5-2)$$

where  $\hat{\Omega}$  is the angle between the molecular segment and the fiber axis.  $S_{ij}$  is a compliance constant of the molecular segment with unit of  $\text{GPa}^{-1}$ , where  $i$  and  $j$  refer to directions relative to the molecular axis (Voigt notation). Direction ‘3’ is the molecular axis, directions ‘1’ and ‘2’ are transverse to this axis, and direction ‘4’ corresponds to shear in a plane containing the molecular axis. The molecular unit is assumed to be transversely isotropic.

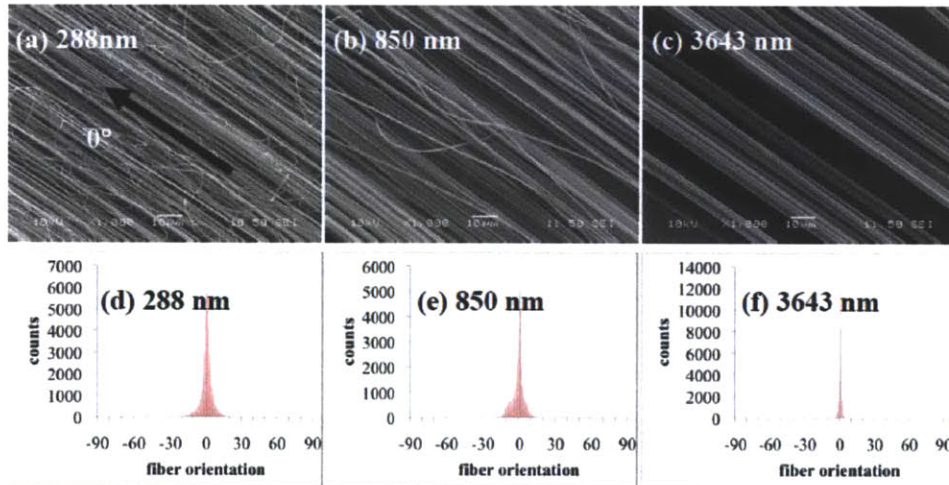


Figure 5-10. Distribution of fiber orientation within aligned bundles of fibers used for molecular orientation determination. (a) ~ (c) SEM images of fiber bundles with different average fiber diameter. Images were taken under 1000x magnification (scale bar = 10  $\mu\text{m}$ ). (d) ~ (f) The distribution of fiber orientation within bundles corresponding to SEM images (a) ~ (c), respectively, determined by image analysis.

We used the angle between the molecular axis and the fiber axis,  $\Omega$ , determined according to Equation (2-1) to approximate the angle between the unit of the aggregate and the fiber axis,  $\hat{\Omega}$ , in Equation (5-2) of Ward's single phase aggregate model. The values of  $S_{11}$ ,  $S_{33}$ ,  $S_{13}$  ( $= -\nu_{13}S_{33}$ , where  $\nu_{13}$  is a Poisson's ratio), and  $S_{44}$  for the molecular unit were treated as fitting parameters using a constrained linear least squares method in the optimization toolbox in MATLAB to obtain the best representation of our experimental data for fiber modulus versus fiber diameter, subject to the constraints that  $S_{33}$  is smaller than  $S_{11}$  and  $S_{44}$ , and  $\nu_{13}$  is assumed to be 0.5. The values obtained are  $S_{11} = 0.544 \text{ GPa}^{-1}$ ,  $S_{33} = 0.07 \text{ GPa}^{-1}$ ,  $S_{13} = -0.035 \text{ GPa}^{-1}$  (or  $\nu_{13} = 0.5$ ), and  $S_{44} = 0.341 \text{ GPa}^{-1}$ . These values were then used to convert the measured molecular orientation within a bundle to an effective fiber modulus for each of the ten bundles reported in Table 5-6. The results are shown by unfilled circles in Figure 5-8(a) and listed in Table 5-7. Mechanical anisotropy due to the effect of molecular orientation on stiffness of amorphous fibers is represented well by Ward's aggregate model. Moreover, the calculated Young's modulus is linearly proportional to the Hencky strain [ $E_0(\text{GPa}) = 0.47 \cdot \varepsilon = 0.94 \cdot \ln(100/d(\mu\text{m}))$ ], which supports the explanation that the greater extensional strain ( $\varepsilon$ ) associated with smaller diameter fibers ( $d$ ) gives rise to increased molecular alignment, which in turn is associated with higher axial stiffness ( $E_0$ ).

#### 5.4 Concluding Remarks

We have studied the dependence of fiber modulus and yield strength for individual electrospun PA 6(3)T fibers on the diameter of the fibers. As the diameter of a PA 6(3)T fiber decreases below 500 nm, the Young's modulus increases; in particular, when the diameter drops to 170 nm, the Young's modulus of the fiber increases to 2 times that of fibers with 3.6  $\mu\text{m}$  diameter. The trend was found to be a consequence of structural anisotropy within the fiber associated with molecular orientation. This conclusion is supported by polarized FTIR measurements and by subsequent modeling using Ward's single-phase aggregate model, which explains the effect of orientation on elastic properties. Similarly, the fiber yield stress also

increases as fiber diameter decreases below one micron, with a factor of 2 increase observed comparing 170 nm fibers with 3.6  $\mu\text{m}$  fibers. The most likely cause of enhanced molecular orientation in smaller diameter fibers is that they have undergone greater extensional deformation during the electrospinning process. Most of this chapter has been published in Ref. [42].

## 5.5 References

- [1] Chew SY, Hufnagel TC, Lim CT, Leong KW. "Mechanical properties of single electrospun drug-encapsulated nanofibers", *Nanotechnology* 2006; 17: 3880-3891.
- [2] Wong SC, Baji A, Leng S. "Effect of fiber diameter on tensile properties of electrospun poly(epsilon-caprolactone)", *Polymer* 2008; 49: 4713-4722.
- [3] Ji Y, Li B, Ge S, Sokolov JC, Rafailovich MH. "Structure and nanomechanical characterization of electrospun PS/clay nanocomposite fibers", *Langmuir* 2006; 22(3): 1321-1328.
- [4] Cuenot S, Demoustier-Champagne S, Nysten B. "Elastic modulus of polypyrrole nanotubes", *Physical Review Letters* 2000; 85(8): 1690-1693.
- [5] Tan EPS, Lim CT. "Physical properties of a single polymeric nanofibers", *Appl. Phys. Lett.* 2004; 84(9): 1603-1605.
- [6] Bellan LM, Kameoka J, Craighead HG. "Measurement of the Young's moduli of individual polyethylene oxide and glass nanofibers", *Nanotechnology* 2005; 16: 1095-1099.
- [7] Shin MK, Kim SI, Kim SJ, Kim SK, Lee H, Spinks GM. "Size-dependent elastic modulus of single electroactive polymer nanofibers", *Appl. Phys. Lett.* 2006; 89: 231929.
- [8] Li L, Bellan LM, Craighead HG, Fret MW. "Formation and properties of nylon-6 and nylon-6/montmorillonite composite nanofibers", *Polymer* 2006; 47: 6208-6217.

- [9] Fu Q, Jin Y, Song X, Gao J, Han X, Jiang X, Zhao Q, Yu D. "Size-dependent mechanical properties of PVA nanofibers reduced via air plasma treatment", *Nanotechnology* 2010; 21: 095703.
- [10] Zussman E, Chen X, Ding W, Calabri L, Dikin DA, Quintana JP, Ruoff RS. "Mechanical and structural characterization of electrospun PAN-derived carbon nanofibers", *Carbon* 2005; 43: 2175-2185.
- [11] Pai CL, Boyce MC, Rutledge GC. "Morphology of porous and wrinkled fibers of polystyrene electrospun from dimethylformamide", *Macromolecules* 2009; 42(6): 2102-2114.
- [12] Arinstein A, Burman M, Gendelman O, Zussman E. "Effect of supramolecular structure on polymer nanofibers elasticity", *Nature Nanotechnology* 2007; 2: 59-62.
- [13] Zussman E, Burman M, Yarin AL. "Tensile deformation of electrospun nylon-6,6 nanofibers", *J. Polym. Sci. Part B: Polym. Phys.* 2006; 44: 1482-1489.
- [14] Jaeger D, Schischka J, Bagdahn J, Jaeger R. "Tensile testing of individual ultrathin electrospun poly(L-lactic acid) fibers", *Journal of Applied Polymer Science* 2009; 114: 3774-3779.
- [15] Naraghi M, Chasiotis I, Kahn H, Wen Y, Dzenis Y. "Novel method for mechanical characterization of polymeric nanofibers", *Review of Scientific Instruments* 2007; 78: 085108.
- [16] Oliver WC, Pharr GM. "An improved technique for determining hardness and elastic-modulus using load and displacement sensing indentation experiments", *J. Mater. Res.* 1992; 7(6): 1564-1583.
- [17] Buer A, Ugbolue SC, Warner SB. "Electrospinning and properties of some nanofibers", *Textile Res. J.* 2001; 71(4): 323.
- [18] Tan EPS, Goh CN, Sow CH, Lim CT. "Tensile test of a single nanofibers using an atomic force microscope tip", *Appl. Phys. Lett.* 2005; 86: 073115.
- [19] Inai R, Kotaki M, Ramakrishna S. "Structure and properties of electrospun PLLA single nanofibers", *Nanotechnology* 2005; 16: 208.
- [20] Tan EPS, Ng SY, Lim CT. "Tensile testing of a single ultrafine polymeric fiber", *Biomaterials* 2005; 26: 1453.

- [21] Wang M, Jin HJ, Kaplan DL, Rutledge GC. "Mechanical properties of electrospun silk fibers", *Macromolecules* 2004; 37: 6856.
- [22] Wang M, Singh H, Hatton TA, Rutledge GC. "Field-responsive superparamagnetic composite nanofibers by electrospinning", *Polymer* 2004; 45: 5505.
- [23] Mack JJ, Viculis LM, Ali A, Luoh R, Yang G, Hahn HT, Ko FK, Kaner RB. "Graphite nanoplatelet reinforcement of electrospun polyacrylonitrile nanofibers", *Adv. Mater.* 2005; 17: 77.
- [24] Ko F, Gogotsi Y, Ali A, Naguib N, Ye H, Yang G, Li C, Willis P. "Electrospinning of continuous carbon nanotube-filled nanofiber yarns", *Adv. Mater.* 2003; 15: 1161.
- [25] Lee SH, Tekmen C, Sigmund WM. "Three-point bending of electrospun TiO<sub>2</sub> nanofibers", *Material Science and Engineering A* 2005; 398: 77.
- [26] Fu Q, Jin Y, Song X, Gao J, Han X, Jiang X, Zhao Q, Yu D. Size-dependent mechanical properties of PVA nanofibers reduced via air plasma treatment", *Nanotechnology* 2010, 21: 095703.
- [27] Gu SY, Wu QL, Ren J, Vancso G. J."Mechanical properties of a single electrospun fiber and its structures", *Macromol. Rapid Commun.* 2005; 26: 716.
- [28] Silva ECCM, Tong L, Yip S, Van Vliet KJ. "Size effects on the stiffness of silica nanowires", *Small* 2006; 2(2): 239-243.
- [29] Kameoka J, Verbridge SS, Liu H, Czaplewski DA, Craighead HG. "Fabrication of suspended silica glass nanofibers from polymeric materials using a scanned electrospinning source", *Nano Lett.* 2004; 4: 2105.
- [30] Tweedie CA, Constantinides G, Lehman KE, Brill DJ, Blackman GS, Van Vliet KJ. "Enhanced stiffness of amorphous polymer surfaces under confinement of localized contact loads", *Adv. Mater.* 2007; 19: 2540-2546.
- [31] Yuan Y, Ruckenstein E. "Colloidal scale blend of rigid and flexible polyamides", *Polymer Bulletin* 1996; 37: 671-677.
- [32] Umemura J, Murata Y, Tsunashima K, Koizumi N. "Polarized infrared spectra of poled aromatic polyamide films", *J. Polym. Sci. Part B: Polym. Phys.* 1999; 37: 531-538.
- [33] Jaehne B. *Digital Image processing*, 6th ed. Springer, 2005.

- [34] Implementation of the Tzeranis method in MATLAB (R2009a, The Mathworks Inc.) was kindly provided by Dimitrios Tzeranis.
- [35] Gaudiana RA, Sinta RF. "Infrared spectral study of noncrystalline rodlike polymers", *J. Polym. Sci. Part A: Polym. Chem.* 1991; 29: 45-53.
- [36] Kalra A, Parks DM, Rutledge GC. "Molecular simulation of strain dependence of vibrational frequencies for montmorillonite clay and analysis of strain transfer in a polymer-clay nanocomposite", *Macromolecules* 2007; 40(1): 140-144.
- [37] Tashiro K, Minami S, Wu G, Kobayashi M. "Quasi-harmonic treatment of infrared and Raman vibrational frequency-shifts induced by tensile deformation of polymer-chains. 2. Application to the polyoxymethylene and isotactic polypropylene single chains and the 3-dimensional orthorhombic polyethylene crystal", *J. Polym. Sci. Part B: Polym. Phys.* 1992; 30: 1143-1155.
- [38] McKinley GH, Sridhar T. "Filament-stretching rheometry of complex fluids", *Annu. Rev. Fluid Mech.* 2002; 34: 375-415.
- [39] Yu JH, Fridrikh SV, Rutledge GC. "The role of elasticity in the formation of electrospun fibers", *Polymer* 2006; 47: 4789-4797.
- [40] Fridrikh SV, Yu JH, Brenner MP, Rutledge GC. "Controlling the fiber diameter during electrospinning", *Phys. Rev. Lett.* 2003; 90(14): 144502.
- [41] Biswas, PK. "The mechanical and optical-properties of oriented fibers of semicrystalline polymers", *Colloid & Polymer Sci.* 1984; 262: 623-626.
- [42] Pai CL, Boyce MC, Rutledge GC. "Mechanical properties of individual electrospun PA 6(3)T fibers and their variation with fiber diameter", *Polymer*, 2011; 52: 2295.



## **Chapter 6 Microstructural Modeling of the Elastic Modulus of Electrospun Nonwoven Fiber Meshes**

### **6.1 Introduction**

Electrospun nonwoven fabrics can be used in many applications that benefit from a high surface area and porous fibrous structure, such as filtration materials, fuel cell membranes, catalytic systems, and sensors [2-3]. Mechanical integrity is particularly of concern in the usage of these mats. Although many experimental and theoretical studies on mechanical properties have been conducted on nonwoven fabrics, especially for traditional ones, no systematic and comprehensive studies that can be easily applied to mats comprising relatively small electrospun fibers have been carefully done. For example, the fiber below a critical diameter, such as 500 nm for poly(trimethyl hexamethylene terephthalamide) (PA 6(3)T) [4], exhibits enhanced Young's modulus and yield stress compared to microscale fibers.

According to Jearanaisilawong [5], models of nonwoven fabrics can be categorized into four main approaches. These four approaches are: (i) an idealized composite model of homogenous continuum components without considering the structure of the material at fiber level; (ii) a composite structure consisting of many continuum components to represent the idealized elements of the fabric structure; (iii) a complex fiber network structure to capture the macroscopic response of the fabric from the interactions between the components of the structure at the fiber and bond level; and (iv) a both continuum- and microstructurally-based approach that uses a representative volume element of the material to homogenize the macroscopic response of nonwoven fabrics [6,7]. The requirement of moderate computational expense for practical usage and acceptable prediction for rational physical features of fibers motivates us to choose the microstructurally-based continuum approach.

In the experimental part, uniaxial tensile testing of nonwoven fabrics is usually performed as an assurance of their mechanical performance [8-11]. The reported Young's modulus is calculated from the slope of the stress-strain curve, where the

engineering stress, the force divided by the initial cross sectional area, is usually used. In that case, to measure the thickness of a soft material accurately with contact methods (e.g. simply using a micrometer) is an issue because the thickness of soft materials is a function of applied pressure. Therefore, the thickness should be reported under a certain pressure, which is usually not the case when people report the thickness of the nonwoven fabrics. A more reliable way to report the stress for nonwoven fabrics is to report force per unit width of the fabric, also called the membrane modulus, and the mass per unit area of fabric, also called the basis weight, which is a typical way to report stress data on nonwoven fabrics in industry. Reporting values in terms of membrane modulus and basis weight, rather than the traditional elastic modulus and fabric density, circumvents the error-prone determination of fabric thickness. Basis weight is defined as weight per area (width x length), and can be equal to the product of multiplying the apparent density of the mat (density of the fiber x volume fraction of the fibers) times the thickness of the mat.

We present a relatively simple model that can relate the Young's modulus of single fibers to their nonwoven fabrics, and vice versa, focusing on electrospun polymeric fibers for experimental validation. Two quantitative microstructure-based models that relate the Young's modulus of these fabrics to that of the fibers are considered, one assuming straight fibers and the other allowing for sinuous fibers. This study is particularly important for meshes comprising fibers because of the recent discovery of an enhanced size effect on their Young's modulus as well as the tendency towards a curving nature. The governing factors that affect the mechanical properties of nonwoven mats are the fiber network, fiber curvature, intrinsic fiber properties, and fiber-fiber junctions.

## **6.2 Theoretical Section**

### **6.2.1. Nonwoven Fabric Model for Straight Fibers**

The constitutive model for a two-dimensional network of fibers of nonwoven mats is developed here using a 4-fiber construction as the representative volume element (RVE) [6,7], as shown in Figure 6-1. Individual fibers are allowed to rotate

and to extend or compress. The torsional resistance comes from the junction stiffness and the effective influence of laterally oriented fibers which also restrict rotation of other fibers, and it is shown schematically in Figure 6-1 by a spring with a torsional potential  $k_{junction}$  (similar to the spring constant in Hooke's law, but in terms of the change in angle instead of in length).

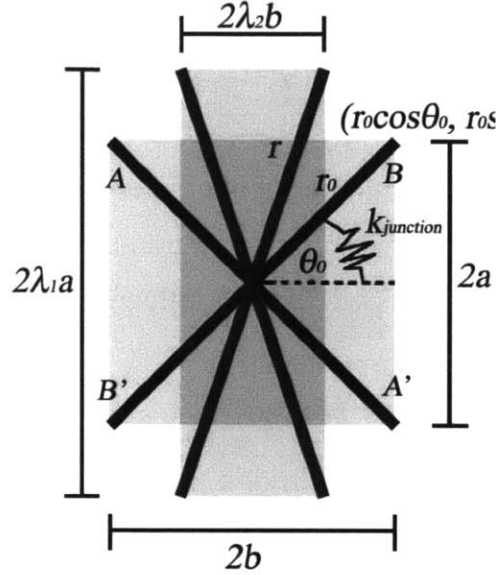


Figure 6-1. Schematic of a 4-fiber model with square region ( $2a \times 2b$ ) representing the RVE before deformation and the rectangular region ( $2\lambda_1 a \times 2\lambda_2 b$ ) representing the RVE after deformation.

A strain energy density function is constructed for this 4-fiber model using the macroscopic deformation gradient to capture the force-extension behaviors of fibers. The macroscopic deformation gradient is:

$$F_{2D} = \frac{\partial x}{\partial X} = \begin{bmatrix} F_{11} & F_{12} \\ F_{21} & F_{22} \end{bmatrix} = \begin{bmatrix} \lambda_1 & 0 \\ 0 & \lambda_2 \end{bmatrix} \quad (6-1)$$

where  $x$  is the deformed position of a material point,  $X$  is the reference position, and  $\lambda_i$  is one of the two principle stretches within the plane.

$$\text{The stretch ratio of fibers is: } \lambda_f = \frac{r}{r_0} = \left( \lambda_1^2 \sin^2 \theta_0 + \lambda_2^2 \cos^2 \theta_0 \right)^{1/2} \quad (6-2)$$

where  $r_0$  is the initial fiber length between junctions,  $r$  is the deformed fiber length, and  $\theta_0 = \tan^{-1}(a/b)$  is the angle between the initial fiber orientation and the lateral axis.

$$\text{The strain energy is: } u_f = \frac{1}{2} k_f r_0^2 (\lambda_f - 1)^2 \quad (6-3)$$

where  $k_f$  is the fiber axial stiffness in units of force per unit length.

The strain energy density for the RVE containing 4 fibers (A, A', B, and B') is

$$u^* = \frac{\nu}{n} \left[ \left( \sum_{i=1}^{n=4} u_i \right) + u_{\text{junction}} \right] = \frac{\nu}{2} k_f r_0^2 (\lambda_f - 1)^2 + u_{\text{junction}}^* = \nu u_f + u_{\text{junction}}^* \quad (6-4)$$

where  $\nu$  is the areal density (number of fibers per unit area), and  $u_{\text{junction}}$  is the strain energy that captures resistance of fiber rotation [13], here arising from both the junction rotational stiffness as well as the influence of lateral fibers in restrictively rotation.

The Cauchy stress tensors can be calculated from the following equations:

$$T_1 = \frac{1}{J} \frac{\partial(\nu u_f)}{\partial \mathcal{F}_{11}} F_{11}^T + \frac{\lambda_1}{J} n_{\text{junction}} k_{\text{junction}} (\theta - \theta_0) \frac{\partial}{\partial \lambda_1}; \quad (6-5a)$$

$$T_2 = \frac{1}{J} \frac{\partial(\nu u_f)}{\partial \mathcal{F}_{22}} F_{22}^T + \frac{\lambda_2}{J} n_{\text{junction}} k_{\text{junction}} (\theta - \theta_0) \frac{\partial}{\partial \lambda_2} = 0 \quad (6-5b)$$

where  $J = \det(F) = \lambda_1 \lambda_2$  is the ratio of deformed area to original area,  $n_{\text{junction}}$  is the number density of junctions per unit area within the network, and  $k_{\text{junction}}$  is the effective torsional stiffness, with the unit of J/rad<sup>2</sup>. Because no restriction is imposed on deformation in the lateral direction,  $T_2$  is identically equal to zero. This  $T_2 = 0$  conclusion provides the equation needed to determine  $k_{\text{junction}}$ .

The derivatives of the chain angle with respect to the principal stretches can be expressed as

$$\frac{\partial}{\partial \lambda_1} = \frac{\partial \cos^{-1} \left( \lambda_2 / \sqrt{\lambda_1^2 + \lambda_2^2} \right)}{\partial \lambda_1} = \frac{\lambda_2}{(\lambda_1^2 + \lambda_2^2)^{3/2}}; \quad (6-6a)$$

$$\frac{\partial}{\partial \lambda_2} = \frac{\partial \cos^{-1} \left( \lambda_2 / \sqrt{\lambda_1^2 + \lambda_2^2} \right)}{\partial \lambda_2} = \frac{-\lambda_1}{(\lambda_1^2 + \lambda_2^2)^{3/2}} \quad (6-6b)$$

By using Equation (6-5b), we can substitute  $n_{junction}k_{junction}$  in Equation (6-5a) with a function containing the principal stretches and the angle.

Young's modulus of the nonwoven fabric can be derived from the first derivative of the Cauchy stress in Equation (6-5) with the principal stretch in the uniaxial direction:

$$E_{mat} = \frac{\lambda_1}{t_{mat}} \frac{\partial T_1}{\partial \lambda_1} \Big|_{\lambda_1=1} = \frac{\nu k_f r_0^2}{t_{mat}} \left[ \langle \sin^2 \theta_0 \rangle^2 + \langle \sin^2 \theta_0 \rangle \langle \cos^2 \theta_0 \rangle \right] \quad (6-7)$$

where  $t_{mat}$  represents the thickness of nonwoven mats.

For a nonwoven mesh of randomly oriented fibers, the two-dimensional ensemble average value for  $\langle \sin^2 \theta_0 \rangle^2 = \langle \cos^2 \theta_0 \rangle^2 = 1/4$ , giving  $\theta = 45^\circ$ , so that:

$$E_{mat} = \frac{\nu k_f r_0^2}{2t_{mat}} \quad (6-8)$$

The relation between  $k_f$  and the Young's modulus of single fibers,  $E_f$ , is:

$$k_f = \frac{E_f A_f}{r_0} = \frac{E_f (\pi d^2 / 4)}{r_0} \quad (6-9)$$

where  $A_f$  is the cross sectional area of a fiber, and  $d$  is the fiber diameter.

The relation between  $\nu$  and the porosity of the nonwoven mat,  $\phi$ , is:

$$1 - \phi = \frac{V_f}{V_{mat}} = \frac{m / \rho_f}{W_{mat} L_{mat} t_{mat}} = \frac{(b.w.) / \rho_f}{t_{mat}} = \frac{N A_f r_0}{W_{mat} L_{mat} t_{mat}} = \frac{\nu A_f r_0}{t_{mat}} \quad (6-10)$$

where  $V_f$  and  $V_{mat}$  are the volume of solid fibers alone and of the nonwoven mat, respectively. Further,  $m$  is the sample weight,  $\rho_f$  is the material density of the fibers,  $W_{mat}$  is the width of the nonwoven mat,  $L_{mat}$  is the length of the nonwoven mat,  $b.w.$  is the basis weight of the sample, and  $N$  is the total number of fibers in the nonwoven mat.

We substitute Equation (6-9) and (6-10) into Equation (6-8) to replace parameters  $k_f$  and  $\nu$  by parameters that can be measured easily:

$$E_f = \frac{2\rho_f}{(b.w.)} E_{mat} t_{mat} = \frac{2\rho_f}{(b.w.)} \frac{\Delta F}{W_{mat} \Delta \varepsilon} \Big|_{elastic} \quad (6-11)$$

We measure the width, length, and weight of the nonwoven sample with known material density of the fibers. Once the elastic region of mechanical testing is obtained, the Young's modulus of fibers can be estimated by Equation (6-11).

### 6.2.2. Nonwoven Fabric Model for Sinuous Fibers

Up to this point, all fibers have been assumed to be straight, responding to an imposed deformation by changing length and rotating in response to the applied force. However, electrospun fibers generally are observed by SEM to have some degree of curvature [14]. Such fibers can respond to deformation by bending or unbending. A modified version of the foregoing model that includes consideration of bending or unbending on the change of fiber stiffness is shown in Figure 6-2.

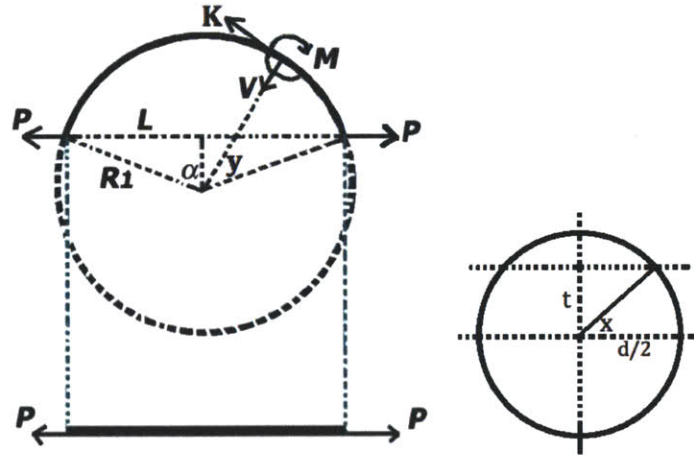


Figure 6-2. (left) Schematic of a curving fiber with a radius of curvature  $R_1$ , and a straight fiber with infinite curvature and fiber length  $2L$ , under the same loading force  $P$ ; (right) cross-section of a fiber with diameter  $d$ , and arbitrary  $t = \sin x \cdot d/2$ .

First, the force and moment balances for the sinuous fiber segment are expressed by the following equations:

$$\text{Force balance: } K \cos(\alpha - y) + V \sin(\alpha - y) = P \quad (6-12a)$$

$$K \sin(\alpha - y) = V \cos(\alpha - y) \quad (6-12b)$$

$$\text{Moment balance: } M = P \left( R_1 \cos(\alpha - y) - \sqrt{R_1^2 - L^2} \right) \quad (6-13)$$

where  $K$  and  $V$  are the axial and transverse forces acting on the fiber,  $P$  is the applied load,  $\alpha = \arcsin(L/R_1)$ , and  $y$  is an arbitrary angle.  $M$  is the moment,  $R_1$  is the radius of curvature, and  $2L$  is the distance between two adjacent junction points.

From Equation (6-12a) and (6-12b), we find:

$$K = P \cos(\alpha - y) \quad (6-14)$$

We also need to formulate the axial stress distribution across any cross-section of the fiber in order to calculate the strain energy.

$$\text{Axial stress: } \sigma_{axial} = -\frac{Mt}{I} + \frac{K}{A_f} \quad (6-15)$$

where  $M$  varies along the fiber as described by Equation (6-13),  $t$  is shown in Fig.2, and  $I = \pi d^4/64$ . Note in particular that the second moment of area,  $I$ , is proportional to the fourth power of fiber diameter, which indicates the tendency towards a curvy nature because smaller fibers has smaller  $I$ , thus having smaller resistance to the bending and deflection.

$$\text{The strain energy is: } U = \int_{V_f} \frac{\sigma_{axial}^2}{2E_f} dV_f = \frac{1}{2E_f} \int_{V_f} \left( \frac{M^2 t^2}{I^2} - \frac{2MtK}{IA_f} + \frac{K^2}{A_f^2} \right) dV_f \quad (6-16)$$

where  $dV_f = dA_f(R_1 dy)$ . After the integration,  $U = P^2\beta$ , where:

$$\beta = \left[ \frac{R_1^3}{2E_f I} \alpha + \frac{R_1^3}{4E_f I} \sin(2\alpha) - \frac{2R_1^2 \sqrt{R_1^2 - L^2}}{E_f I} \sin\alpha + \frac{(R_1^2 - L^2)R_1}{E_f I} \alpha + \frac{R_1 \alpha}{2E_f A_f} + \frac{R_1 \sin(2\alpha)}{4E_f A_f} \right] \quad (6-17)$$

The displacement can be calculated by  $\delta = \frac{\partial U}{\partial P} = 2P\beta$ .

As a result  $U = \delta^2/(4\beta) = k_{cf}\delta^2/2$ , and the axial stiffness of sinuous fibers,  $k_{cf} = 1/(2\beta)$ .

We define the stiffness ratio (SR) as the ratios of the stiffness of a curved fiber to the stiffness of a straight fiber of same end-to-end length as:

$$\text{SR} = \frac{E_{cf}}{E_f} = \frac{2k_{cf}L/A_f}{2k_f L/A_f} = \frac{1/(2\beta)}{k_f} \text{ with } 0 < \text{SR} \leq 1 \quad (6-18)$$

Note that  $E_f$  in Equation (11) becomes  $E_{cf}$  in Equation (6-18), which can be rewritten as a function of only junction length (L), fiber diameter (d), and radius of curvature ( $R_1$ ):

$$SR = \frac{1}{\left[ \frac{8R_1^3}{d^2L} \operatorname{asin}\left(\frac{L}{R_1}\right) + \frac{8R_1\sqrt{R_1^2 - L^2}}{d^2} - \frac{32R_1\sqrt{R_1^2 - L^2}}{d^2} + \frac{16(R_1^2 - L^2)R_1}{d^2L} \operatorname{asin}\left(\frac{L}{R_1}\right) + \frac{R_1}{2L} \operatorname{asin}\left(\frac{L}{R_1}\right) + \frac{\sqrt{R_1^2 - L^2}}{2R_1} \right]} \quad (6-19)$$

As a limiting case:  $R_1 \rightarrow \infty$ ,  $\alpha$  is very small and  $\sin \alpha \rightarrow \alpha = L/R_1$ , and also  $R_1 \gg L$ . Equation (6-19) turns out to be  $SR = 1$ , which is the case for straight fibers, without any effect of bending on the SR.

### 6.3 Results and Discussion

PA 6(3)T was electrospun to form nonwoven fabrics consisting of homogeneous and smooth fibers over a wide range of fiber diameters, from 113 nm to 3643 nm, as shown in Figure 6-3. Results of the mechanical measurement for randomly distributed nonwoven fabrics comprising different average fiber diameter were listed in Table 6-1. At least four nonwoven fabrics were tested for each fiber diameter. The basis weight, width of the sample (0.7 cm), and the elastic change of force with strain (the value can be retrieved by calculating  $E_{mat} \cdot t_{mat} \cdot W_{mat}$ ) were measured, and can be found in Table 6-1. The material density of PA 6(3)T is known to be 1.12 g/cm<sup>3</sup> [15].

The thickness of the nonwoven fabrics,  $t_{mat}$ , can be measured by the micrometer with a constant pressure, or calculated by using Equation (6-10) with the porosity measured by the mercury penetrometer. In other words, we can either choose to measure the porosity and calculate the  $t_{mat}$ , or vice versa. The porosity for all nonwoven fabrics is about 0.875 to 0.914 obtained from the calculation according to the thickness measurement of the micrometer, and it is about 0.915 to 0.925 from the porosity measurement of the mercury penetrometer. The porosity does not vary much despite the mats comprising average fiber diameters ranging from 113 nm to 3643 nm, and shows only a little bit higher value for smaller fibers. According to the work done by Pham et al. [16], they also observed a constant porosity for poly( $\epsilon$ -caprolactone)(PCL) microfiber scaffolds with average fiber diameters ranging from



2 to 10  $\mu\text{m}$ . Also note that the slight discrepancy of measured porosity from different techniques.

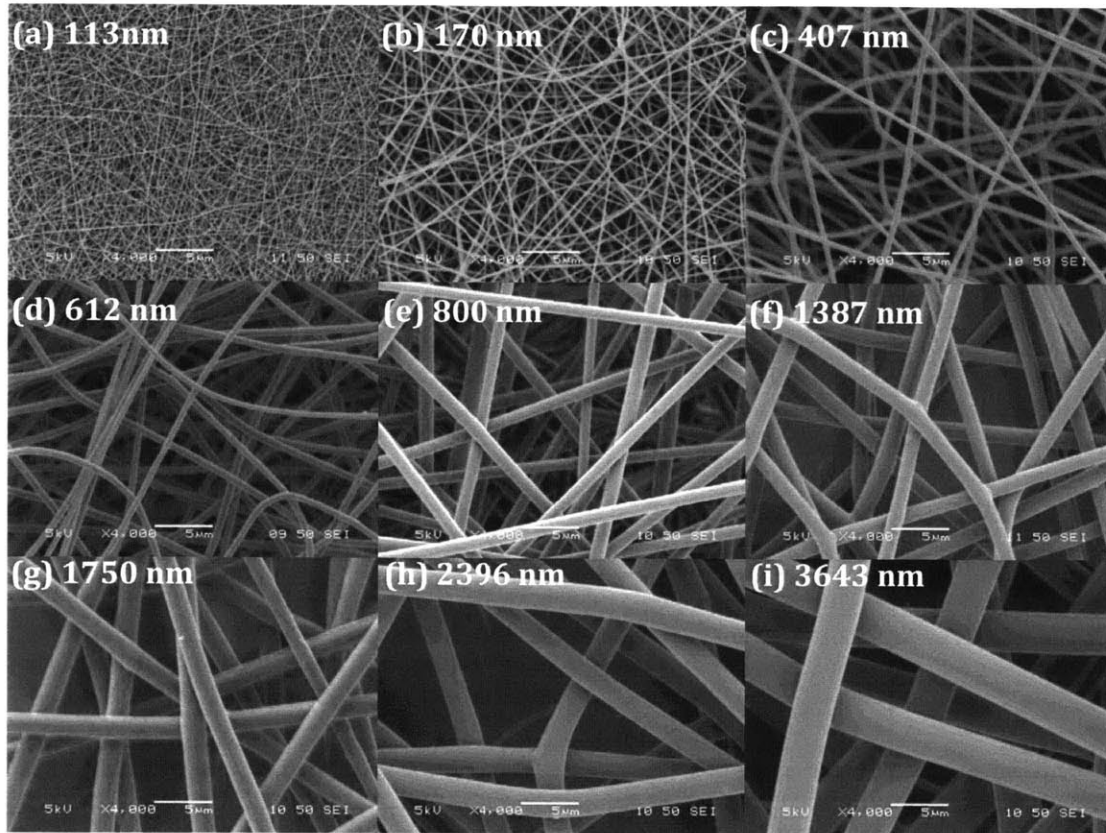


Figure 6-3. Representative SEM images of PA 6(3)T nonwoven fabrics with different diameters (scale bar = 5  $\mu\text{m}$ ).

Previously, we investigated how the Young's modulus of a single electrospun fiber depends on its diameter and found that small fibers below a critical diameter have higher stiffness than large fibers. When we combine this size effect of fibers on their nonwovens, The dependence of the Young's modulus of nonwoven fabrics on fiber diameters is plotted in Figure 6-5(a), obtained from the force vs strain data for nonwoven fabrics of known sample width and thickness. The error bar corresponds to one standard deviation, due to the variation between samples. Remarkably,  $E_{mat}$  is observed to decrease slightly with decreasing fiber diameter. This contrasts with the mechanical measurements of single fibers, reported previously in Chap 5 as well as in [4] and shown as the filled diamond symbols in Figure 6-5(b), in which it was observed that the smaller fibers are notably stiffer. Using Equation (6-11) for the

model for straight fibers, the fiber modulus  $E_{cf}$  can be calculated; the resulting values are listed in Table 6-1. We plot  $E_{cf}$  calculated from Equation (6-11) in Figure 6-5(b), as shown in the filled triangular symbols, and compare with data obtained from the direct measurement of each single fiber. We found that the Young's moduli of fibers derived from the measurement of nonwoven fabrics fall below the values measured and reported previously. This discrepancy indicates that the simple model based on straight fibers does not capture all the major factors implicated in the expression of elastic modulus of nonwoven fabrics to nanofibers.

Table 6-1: Data for the modified model for fibers with curvature and the results

$d$ ( $\mu\text{m}$ )	$b.w.$ ( $\text{kg}/\text{m}^2$ )	$t_{mat}$ ( $\mu\text{m}$ )	$E_{mat}$ (MPa)	$R_1$ ( $\mu\text{m}$ )	$\phi$	$L$ ( $\mu\text{m}$ )	$SR$	$E_{cf}$ (Gpa)	$E_f$ (Gpa)	$E_{ward}$ (Gpa)
0.113	0.0031	28	53±11	15.4	0.90	1.67	0.15	1.05±0.11	6.83	6.38
0.128	0.0031	27	49±7	17.7	0.90	1.89	0.16	0.98±0.14	6.21	6.26
0.143	0.0019	17	51±15	20.0	0.90	2.11	0.16	1.01±0.31	6.25	6.16
0.170	0.0051	45	56±2	24.2	0.90	2.50	0.17	1.12±0.05	6.69	5.99
0.288	0.0090	79	48±7	43.5	0.90	4.21	0.19	0.95±0.13	5.03	5.50
0.385	0.0097	85	51±10	60.0	0.90	5.59	0.20	1.00±0.20	4.93	5.23
0.407	0.0139	122	55±13	63.8	0.90	5.90	0.21	1.08±0.25	5.25	5.17
0.612	0.0220	191	47±6	100.3	0.90	8.77	0.23	0.92±0.25	4.01	4.79
0.800	0.0110	89	58±4	135.1	0.90	11.33	0.25	1.06±0.09	4.27	4.54
1.040	0.0091	77	52±3	180.7	0.89	14.53	0.27	0.99±0.06	3.66	4.29
1.290	0.0052	43	70±9	229.5	0.89	17.76	0.29	1.32±0.16	4.53	4.09
1.387	0.0113	94	69±14	248.7	0.89	18.99	0.30	1.28±0.26	4.27	4.02
1.750	0.0127	104	61±9	321.8	0.89	23.46	0.33	1.11±0.16	3.38	3.80
1.840	0.0136	111	57±8	340.3	0.89	24.54	0.34	1.04±0.15	3.10	3.76
1.910	0.0143	116	66±9	354.6	0.89	25.38	0.34	1.19±0.16	3.49	3.72
1.960	0.0131	106	60±9	365.0	0.89	25.97	0.34	1.08±0.17	3.13	3.70
2.240	0.0126	101	54±14	423.2	0.89	29.22	0.37	0.96±0.25	2.62	3.57
2.396	0.0145	115	71±9	456.1	0.89	30.98	0.38	1.26±0.17	3.34	3.51
3.643	0.0399	297	89±12	725.9	0.88	44.06	0.46	1.49±0.20	3.20	3.11

As is apparent from Figure 6-3 and similar images of nanofiber nonwoven fabrics, the fibers are distinctly sinuous, especially when the fibers are small in diameter. Therefore, the original four-fiber model is modified by replacing straight fiber elements with sinuous fiber elements. As shown by Equation (6-18) and

Equation (6-19), the actual Young's modulus of fibers is equal to that predicted by Equation (6-11) divided by the stiffness ratio. Three additional characteristics of the nonwoven mat are required: the through-space distance between consecutive junctions along a fiber ( $2L$ ), and the radius of curvature ( $R_1$ ).

For purposes of this work, these characteristics are measured manually from SEM images as shown in Figure 6-4 and averaged over at least 300 measurements per image, with 5 images per sample; automation of this procedure can be readily envisioned. The radius of curvature is determined by tracing visually along a fiber and taking the coordinates of three points where the fiber appears to cross, or form a junction with, another fiber. Then, these three points were used to construct a circle, from which the radius of curvature is obtained. The average radius of curvature was calculated from about 300 circles per sample, and for 5 samples of different average fiber diameter. The results can be described by a logarithmic function, as shown in Figure 6-5 and the following equation, in order to be applied to all fiber diameters, as listed in Table 6-1.

$$R_1 = d^{1.1094} \exp(5.1532) \quad (6-20)$$

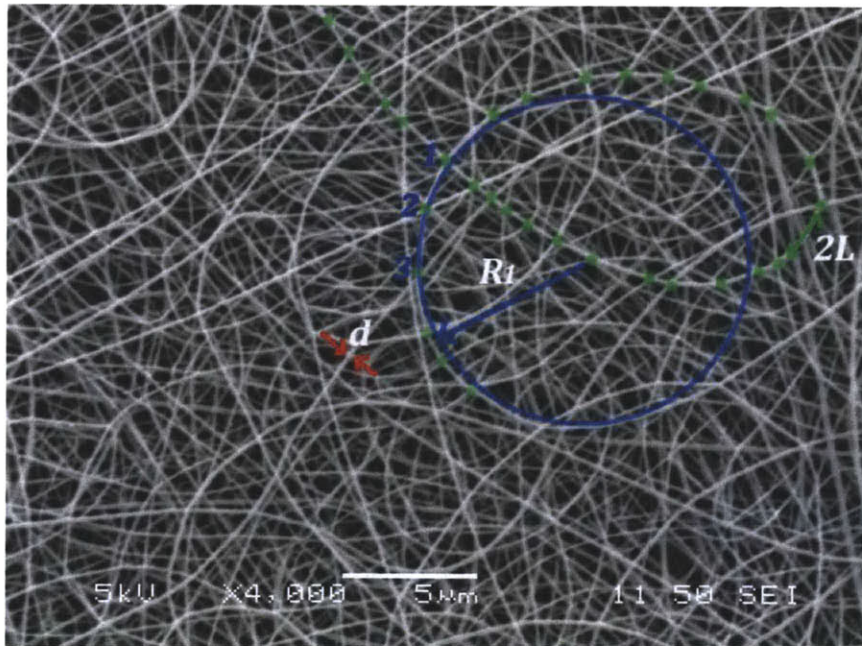


Figure 6-4. Schematic illustration of the radius of curvature ( $R_1$ ), the distance between the adjacent junctions ( $2L$ ), and the diameter of fibers ( $d$ ).

However, the determination of the distance between adjacent junctions ( $2L$ ) is very subjective because several layers of the nonwoven fabric were viewed in SEM instead of only a coplanar layer of it. The image involves the depth of field, and the layers viewed depend on fiber size, so it is hard to tell if the cross point is a true junction or not. Using the naked eye is apparently not a good way to distinguish junction points in SEM images, but we tried our best to distinguish junction points in SEM images that way and the results are plotted in Figure 6-5(b). At the same time, an equation for the calculation of the mean pore radius [17] was used to approximate the half distance between the adjacent junctions,  $L$ .

$$L = -\frac{d\sqrt{\pi}}{4} \left( 1 + \frac{\pi}{2 \log \phi} \right) \quad (6-21)$$

We find that  $L$  calculated from Equation (6-21) is larger than what we measured in SEM images. This can be attributed to the possibility that the junction points judged by the naked eye might not be true junction points, thus underestimating the  $L$ . Therefore, we choose to use  $L$  from Equation (6-21) instead of  $L$  from Figure 6-6(b). The results of the derived Young's modulus of fibers,  $E_f$ , based on the model for fibers with curvature, listed in Table 6-1 and plotted in Figure 6-6(b) by open triangles, now approach what we measured from the single fiber. Note that  $L$  in Equation (6-25) is very sensitive to the porosity,  $\phi$ . Therefore, we used a reasonable range of porosity (0.88~0.90), and assumed a linear dependence on fiber diameter (0.90 for the smallest fibers and 0.88 for the largest fibers) in order to reasonably predict the Young's modulus of single fibers. Other than that, no fitting parameters were used in our models. In order to further verify the model, we calculate the SR for the size of commercial fiber,  $\sim 10 \mu\text{m}$ . SR equals 0.78, which is reasonable to overlook compared to that of the relatively small electrospun fibers.

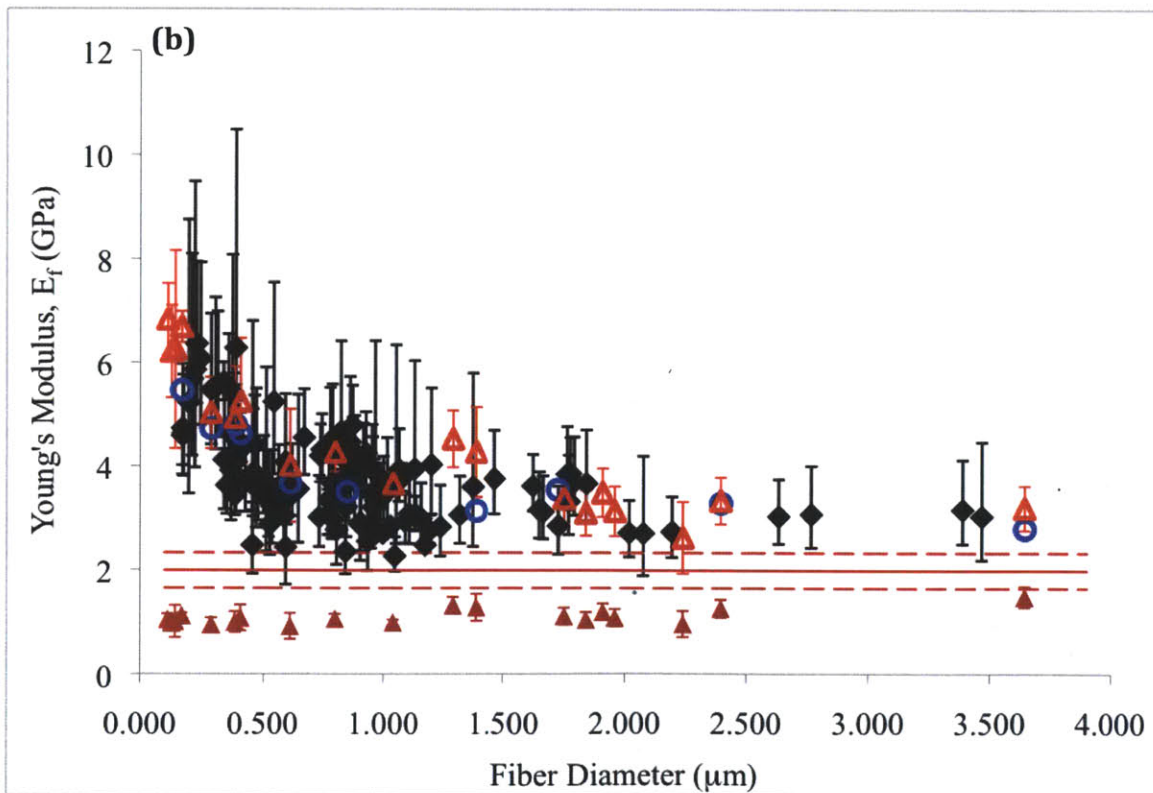
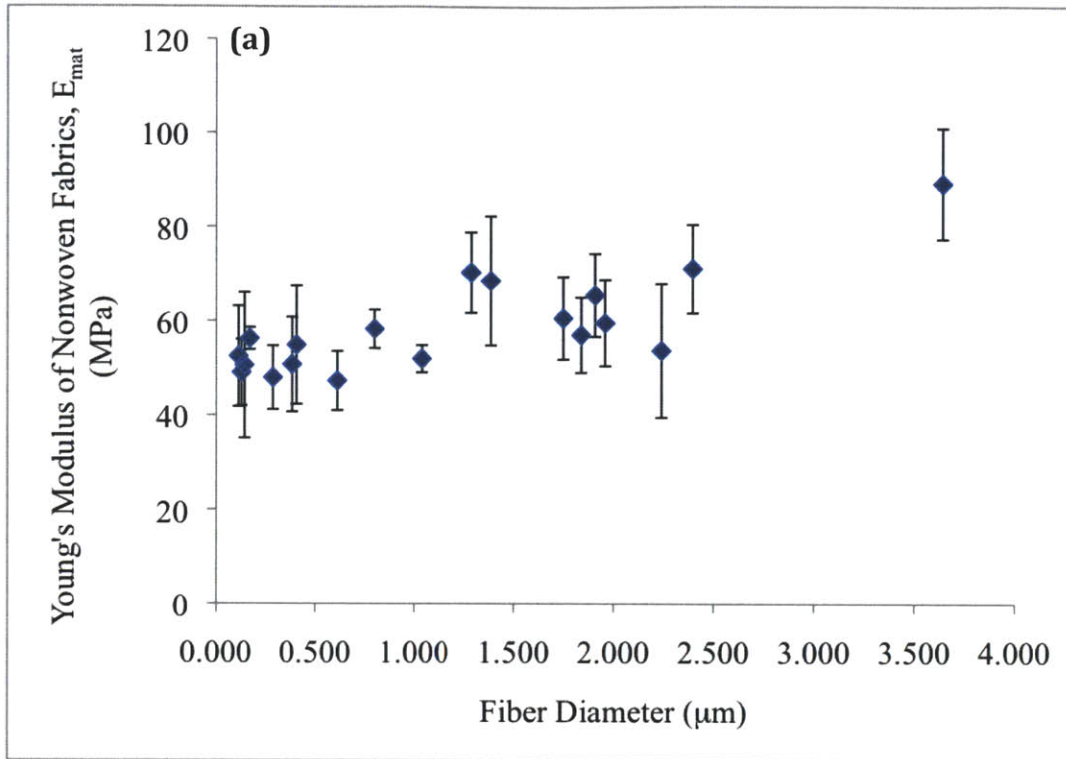


Figure 6-5. Dependence of (a) Young's modulus of nonwoven fabrics on fiber diameter, and (b) Young's modulus of single fibers on fiber diameter. Filled

diamonds represent experimental data in uniaxial extension; open circles represent values obtained from molecular orientation measurements using Ward's aggregate model [4]. Filled triangles represent derived Young's modulus of the single fiber from mat data assuming straight fibers, and open triangles represent that assuming sinuous fibers.

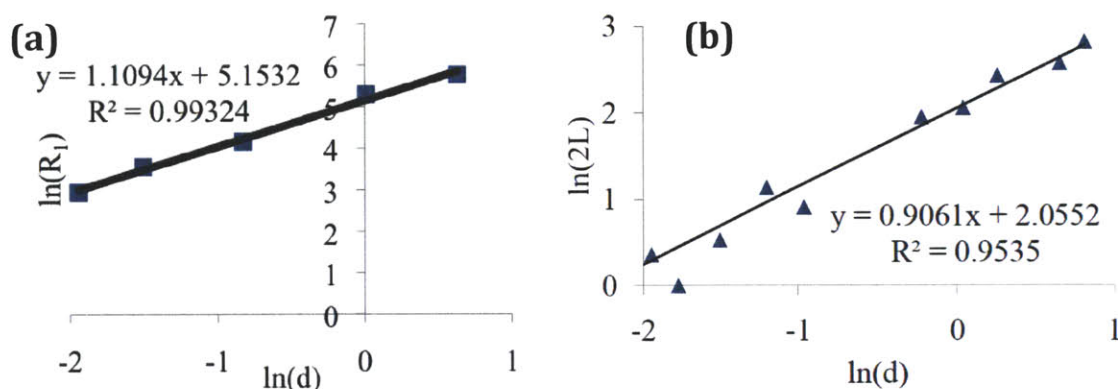


Figure 6-6. The logarithmic relation of (a) radius of the curvature and fiber diameter; (b) distance between adjacent junctions and fiber diameter.

#### 6.4 Concluding Remarks

We conducted a systematic study on the dependence of the Young's modulus of nonwoven fabrics on fiber diameters, and found that the nonwoven fabric comprising smaller fibers does not show enhanced Young's modulus compared to larger fibers. We identified three important parameters, which are the fiber diameter, radius of the curvature, and the junction length, which significantly affect the Young's modulus of nonwoven fabrics. We can modify our process of electrospinning in order to change any of these parameters. For example, we can try to fuse or weld the fibers by thermal treatment or residual solvent in order to decrease the junction length. This study provides us simple analytical equations to calculate the Young's modulus of fibers by measuring properties of the nonwoven fabrics, which is useful for the nanofibers due to the current instrument load cell limitation and difficulty of tiny sample handling by human.

## 6.5 References

- [1] Shin YM, Hohman MM, Brenner MP, Rutledge GC. "Electrospinning: A whipping fluid jet generates submicron polymer fibers" *Appl Phys Lett* 2001; 8: 1149-1151.
- [2] Huang ZM, Zhang YZ, Kotaki M, Ramakrishna S. "A review on polymer nanofibers by electrospinning and their applications in nanocomposites", *Composites Science and Technology* 2003; 63: 2223-2253.
- [3] Li D, Xia Y. "Electrospinning of nanofibers: Reinventing the wheel?", *Adv Mater* 2004; 16: 1151-1170.
- [4] Pai CL, Boyce MC, Rutledge GC. "Mechanical properties of individual electrospun PA 6(3)T fibers and their variation with fiber diameter", *Polymer*, 2011; 52: 2295.
- [5] Jearanaisilawong P, Ph.D. thesis at MIT, 2008; 19-23.
- [6] Arslan M, Boyce MC. "Constitutive modeling of the finite deformation behavior of membranes possessing a triangulated network microstructure", *Journal of Applied Mechanics* 2006; 73: 536-543.
- [7] Qi HJ, Ortiz C, Boyce MC. "Mechanics of biomacromolecular networks containing folded domains", *Journal of Engineering Materials and Technology* 2006; 128: 509-518.
- [8] Jin HJ, Chen J, Karageorgiou V, Altman GH, Kaplan DL. "human bone marrow stromal cell responses on electrospun silk fibroin mats", *Biomaterials* 2004; 25: 1039-1047.
- [9] Sen R, Zhao B, Perea D, Itkis ME, Hu H, Love J, Bekyarova E, Haddon RC. "Preparation of single-walled carbon nanotube reinforced polystyrene and polyurethane nanofibers and membranes by electrospinning", *Nano Letters* 2004; 4(3): 459-464.
- [10] Li L, Bellan LM, Craighead HG, Frey MW. "Formation and properties of nylon-6 and nylon-6/montmorillonite composite nanofibers", *Polymer* 2006; 47: 6208-6217.

- [11] Zong X, Ran S, Fang D, Hsiao BS, Chu B. "Control of structure, morphology and property in electrospun poly(glycolide-co-lactide) non-woven membranes via post-draw treatments", *Polymer* 2003; 44: 4959-4967.
- [12] Hohman MM, Shin M, Rutledge GC, Brenner MP. "Electrospinning and electrically forced jets. II. Applications", *Phys. Fluids* 2001; 13(8): 2221-2236.
- [13] Palmer JS, Ph.D. thesis at MIT, 2008; 172-175.
- [14] Engelmayr GC Jr, Sacks MS. "A structural model for the flexural mechanics of nonwoven tissue engineering scaffolds", *Journal of Biomechanical Engineering* 2006; 128: 610-622.
- [15] Feldman D, Barbalata A. *Synthetic Polymers*, 1st ed.; Chapman & Hall: London, UK, 1996; 242.
- [16] Pham QP, Sharma U, Mikos AG. "Electrospun poly(epsilon-caprolactone) microfiber and multilayer nanofibers/microfiber scaffolds: Characterization of scaffolds and measurement of cellular infiltration", *Biomacromolecules* 2006; 7: 2796-2805.
- [17] Sampson WW. "A multiplanar model for the pore radius distribution in isotropic near-planar stochastic fiber networks", *J. Mater. Sci.* 2003; 38: 1617-1622.



## **Chapter 7 Conclusions and Recommendation**

### **7.1 Conclusions**

Experimental confirmation of electrospun fibers exhibiting a smooth fiber surface and porous interior has not been reported, because such morphologies are easy to overlook by conventional SEM analysis of the fibers, yet will dramatically affect any attempt to rationalize fiber properties. For this reason, it is important to understand the conditions under which such morphologies may arise. From this standing point, we discovered a way to tailor the structures and the topographies of electrospun fibers by investigating the competition among three characteristic times during the process of electrospinning: the drying time, the buckling time, and the phase separation time. The quantitative equations for these characteristic times are provided in this thesis for people to be able to design the desirable structures and topographies of the electrospun fibers, such as smooth and solid fibers; smooth and porous fibers; buckled and solid fibers; and buckled and porous fibers. These electrospun fibers can have a different degree of void volume fraction within the fiber and/or a different critical wave number and wavelength on the wrinkled topographies by varying the fluid properties (e.g. the molecular weight of the polymer, the concentration of the polymer solution, pure or mixed solvent, any additives in the solution) and processing parameters (e.g. the flow rate, electric field, and the environment for the electrospinning).

We conducted a systematic study on the dependence of the Young's modulus of both amorphous nylon single fibers and nonwoven fabrics on fiber diameters. We found the size effect on the Young's modulus of single fibers and explained the trend by the anisotropy induced by the molecular orientation. However, we found that the nonwoven fabric comprising smaller fibers does not show enhanced Young's modulus compared to larger fibers. A quantitative micromechanical model was established to relate the Young's modulus of single fibers to their nonwoven fabrics by assuming all electrospun fibers are straight. However, this model is insufficient to capture all the major factors implicated in the expression of elastic modulus of

nonwoven fabrics to fibers and cannot give us a good prediction for the Young's modulus of the single fiber from the measurement of the nonwoven fabrics. This discrepancy leads us to further examine the fiber network and then realize that electrospun fibers generally are observed by SEM to have some degree of curvature. A modified model for the sinuous fibers was then established, and it can predict the relation between the Young's modulus of the single fiber and the nonwoven fabrics well. We identified three important parameters from this modified model, which are the fiber diameter, radius of the curvature, and the junction length. These key parameters can significantly affect the Young's modulus of nonwoven fabrics. From this finding, we can modify our process of electrospinning or perform some post-treatment on the nonwoven fabrics in order to change any of these parameters and to achieve desirable mechanical performance.

## **7.2 Recommendation for Future Work**

The future work of this study is categorized into three topics: structures (porous fibers), topographies (wrinkle fibers), and size (nanofibers).

### **7.2.1 Porous Fibers**

In the future work, the void size, void shape, void volume fraction, and the distribution of voids inside the fibers should be investigated by varying polymer/solvent/nonsolvent systems, thus varying the behavior of phase separation. For those porous fibers we made from the PS/DMF/Water system, they are lightweight and can be used in the thermal insulation because the thermal conductivity of air is about an order of magnitude lower than polymer. In this case, only the void volume fraction matters. However, if the goal is to create highly porous lightweight carbon structures for the hydrogen storage devices, the surface areas has to be larger than 3700 m<sup>2</sup>/g (for achieving the target of department of energy (DOE), 6.5 wt% hydrogen to carbon at 100 atm and room temperature), which needs the pore size smaller than 0.6 nm if only one layer of hydrogen is adsorbed on the carbon surface. In this case, block copolymer should be considered here because the phase separation domain is smaller and can be around 1~5 nm. If the selective dissolution (to remove one domain of the polymer) followed carbonization and/or

graphitization are done on electrospun fibers of these block copolymer fibers, nanoporous fibers should be obtained. Well defined pores of nanoporous fibers with controllable size can be achieved with more efforts. Sequential surface modification to allow multi-layer adsorption of hydrogen on the carbon surface should be considered as well.

### 7.2.2 Wrinkled Fibers

For the advanced control of surface topographies, the technique of coaxial electrospinning can be applied, and particular polymers in the core and the shell can be selected to vary the ratio of the Young's modulus between them ( $E_c$  and  $E_s$ ). Also, the radius of the resulting fibers ( $a$ ) and the thickness of the shell ( $t$ ) can be varied by changing the operating parameters. For example, choose glassy polymers as both shell and core makes  $E_c/E_s \sim 1$ , whereas choose glassy polymers as shell and elastomer as core makes  $E_c/E_s \sim 0.001$ . In addition, by controlling the flow rate of polymer solution in coaxial electrospinning or the concentration of each component, we can change the ratio of  $a/t$ . Note the miscibility of the solvents used for the shell and core solution in electrospinning will affect the formed interface between these two polymers in fibers.

Bio-antifouling is a possible application for these wrinkle fibers. The adhesion related to the number of attachment points between the size of the organisms and the characteristic topographic dimensions of the fibers can be studied systematically.

### 7.2.3 Nanofibers

In previous work, the size effect was found in amorphous electrospun nylon fibers. Smaller fibers show stiffer mechanical behavior than their bulk materials due to the increasing molecular level orientation within the fibers with decreasing fiber diameter. Further study on semicrystalline polymer should be established in order to understand the effect of the degree of crystalline with decreasing fiber diameter. Once the influence of molecular orientation and crystalline can be fully investigated, the size effect can be explained for electrospun polymeric fibers. Other unforeseen

factors affecting the properties of fibers might be discovered through the progress of the study.

These nanofibers can be used as the reinforcement in nanocomposites. If the reflective index is matched between the matrix and the nanofibers (better <100 nm), the transparent composites can be made. These nanofibers can also be used as the masks to block the small hazardous particle (such as particles with the radiation, but even the small particle itself is a hazard), virus, and pollen. Not only the pore size between interconnected nonwoven fabrics is smaller enough to block the particles, but these nanofibers can be modified with additional surface treatment to trap these particles.

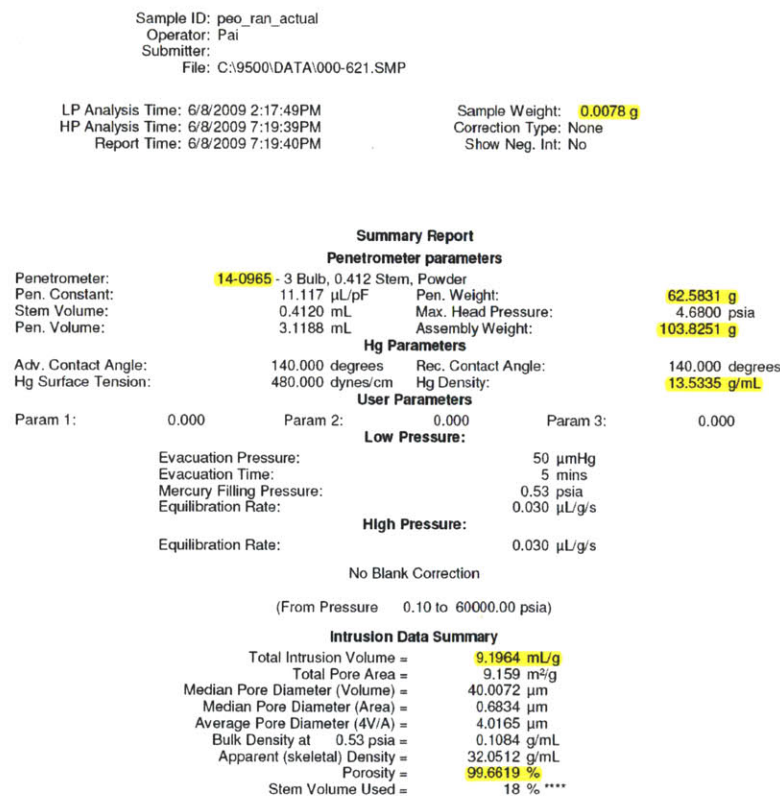
## Appendix I: Modified Equations for Mercury Porosimetry

### Mercury Porosimetry Default Approach for Porosity Calculation (BAD):

The mercury porosimetry uses the following sensitive equation for porosity calculation, which can easily give us porosity over 100% (not correct) unless we weight everything accurately. Take one of my measurements for example.

$$\begin{aligned}
 \text{Porosity} &= \frac{\text{intrusion volume}}{\text{nonwoven bulk volume}} = \frac{\text{intrusion volume}}{\text{penetrometer volume} - \text{mercury volume}} \\
 &= \frac{\text{Total intrusion volume/g} * \text{sample weight}}{\text{penetrometer volume (from the table in manual)} - \text{mercury weight} / \text{mercury density}} \\
 &= \frac{\text{Total intrusion volume/g} * \text{sample weight}}{\text{penetrometer volume (from the table in manual)} - (\text{Assembly weight} - \text{Pen. weight} - \text{Sample weight}) / \text{mercury density}} \\
 &= \frac{9.1964 \text{ mL/g} * 0.0078 \text{ g}}{3.1188 \text{ mL} - (103.8251 - 62.5831 - 0.0078) \text{ g} / 13.5335 \text{ g/mL}} \\
 &= 0.9966
 \end{aligned}$$

The numbers used here are from the figure below with yellow color highlighted:



From the equation, we know that the weight measurement of the sample, assembly and penetrometer (pen.) should be very accurate. Note that the mercury density will change with the temperature. We need to make sure this number is also accurate too. If I measured my sample weight as 0.0079 g (only 0.0001 g differ from

my original number, and the current scale cannot measure this digit very accurate).

Now we found that the porosity is greater than 100%:

$$\begin{aligned} \text{Porosity} &= \frac{9.1964 \text{ mL/g} * 0.0079 \text{ g}}{3.1188 \text{ mL} - (103.8251 - 62.5831 - 0.0079) \text{ g} / 13.5335 \text{ g/mL}} \\ &= 1.0093 \end{aligned}$$

So, the poor equation used by the machine is not a best choice for the calculation of porosity.

**Another Approach (BETTER):**

Another better approach (just rearrange the equation listed above):

$$\begin{aligned} \text{Porosity} &= 1 - \frac{\text{fiber actual volume}}{\text{nonwoven bulk volume}} = 1 - \frac{1}{(\text{intrusion volume} + \text{fiber actual volume}) / \text{fiber actual volume}} \\ &= 1 - \frac{1}{1 + \text{intrusion volume} / \text{fiber actual volume}} \\ &= 1 - \frac{1}{1 + (\text{total intrusion volume/g}) * (\text{sample weight}) / \text{fiber actual volume}} \\ &= 1 - \frac{1}{1 + (\text{total intrusion volume/g}) * \text{sample density}} \\ &= 1 - \frac{1}{1 + 9.1964 \text{ mL/g} * 1.12 \text{ g/mL}} \\ &= 0.9115 \end{aligned}$$

To use this equation, we need to know or assume the density of the polymer. This equation gives us better estimation, at least, the porosity is always smaller than 100%. Also, the porosity calculated from this equation is similar to what I measured using gravity method for thickness (~3% difference) with a constant pressure applied on the sample.

## Appendix II: Matlab Codes for Spinodal and Binodal Curves of Ternary Phase Separation

### (1) Data for spinodal curve:

```
%% Nonsolvent(1)/Solvent(2)/Polymer(3) Ternary System
function iflag_main =spinodal();
clear all; clc; close all;
iflag_main = 0; format long;

%% 1. Initialization
% The molar volume of the Nonsolvent/Solvent/Polymer ternary system.
global nsvol
nsvol=18; % Assume the nonsolvent is water, so the molar volume is 18 cm^3/mole.
global solvol
solvol=77.4; % DMF % Assume the solvent is also a small molecule, which has the same molar volume as the nonsolvent.
global polyvol
polyvol=266667; % Assume the polymer is only 5 times larger than the nonsolvent small molecule.

% Open a file to record the spinodal curve.
fid = fopen('aaa_spinodal.dat','w');
fprintf(fid,'Nonsolvent Polymer Solvent\n');

% error vector to double check if the solver gives correct answers at each iteration.
error_phi1=[0]; error_phi2=[0];

% Initialize the phi3 (the polymer) vector.
phi3_vect=linspace(0.08,0.7,200);

x_guess=[0.5]; % initial guess of phi2
options = optimset('TolFun',1e-6, 'Display','off', 'LargeScale','off');

%% 2. Calculate the spinodal
phians=zeros(length(phi3_vect),3);
for k=1:length(phi3_vect)
    global phi3
    phi3=phi3_vect(k);
    [x,fval] = fsolve(@spinodal_calc,x_guess);
    phi2=x;
    phi1=1-phi3-phi2;
    phians(k,1)=phi1; phians(k,2)=phi2; phians(k,3)=phi3;
    fprintf(fid,'%f\t%f\t%f\n',phi1,phi3,phi2);
    if (phi1<=0)|(phi1>=1)
        error_phi1=[error_phi1 k];
    end
    if (phi2<=0)|(phi2>=1)
        error_phi2=[error_phi2 k];
    end
    x_guess=x;
end
phians(:,1); phians(:,2); phians(:,3);
fclose(fid);

% Display the error message
display(error_phi1), display(error_phi2),

iflag_main=1;
return;

function [fval]=spinodal_calc(x)
fval = zeros(size(x));
phi2=x(1);
global phi3
phi1=1-phi3-phi2;
% Input: The interaction parameters of ternary system: \chi (or called g).
% The parameters could be concentration dependent.
```

```

u1=phi1/(phi1+phi2); u2=phi2/(phi1+phi2);
g12=0.5+0.04*u2+0.8*u2^2-1.2*u2^3+0.8*u2^4; g13=2.2; g23=0.497;
% Derivatives
dg12_du2=0.04+2*0.8*u2-1.2*3*u2^2+0.8*4*u2^3; ddg12_ddu2=2*0.8-1.2*3*2*u2+0.8*4*3*u2^2;
dg13_dphi3=0; ddg13_ddphi3=0;
dg23_dphi3=0; ddg23_ddphi3=0;
global nsvol
global solvol
global polyvol
G22=1/phi1+nsvol/solvol/phi2-2*g12+2*(u1-u2)*dg12_du2+u1*u2*ddg12_ddu2;
G23=1/phi1-(g12+g13)+nsvol/solvol*g23+u2*(u1-2*u2)*dg12_du2+u1*u2*u2*ddg12_ddu2-
phi3*dg13_dphi3+nsvol/solvol*phi3*dg23_dphi3;
G33=1/phi1+nsvol/polyvol/phi3-2*g13-2*u2^2*(1-u1)*dg12_du2+u1*u2^3*ddg12_ddu2+2*(phi1-phi3)*dg13_dphi3+...
phi1*phi3*ddg13_ddphi3+2*nsvol/solvol*dg23_dphi3+nsvol/solvol*phi2*phi3*ddg23_ddphi3;
fval(1)=G22*G33-G23*G23;
return;

```

## (2) Data for binodal curve:

```

%% Nonsolvent(1)/Solvent(2)/Polymer(3) Ternary System
function iflag_main =binodal();
clear all;
iflag_main = 0; format long;

%% 1. Initialization
% The molar volume of the Nonsolvent/Solvent/Polymer ternary system.
global nsvol
nsvol=18; % Assume the nonsolvent is water, so the molar volume is 18 cm^3/mole.
global solvol
solvol=77.4; % Assume the solvent is also a small molecule, which has the same molar volume as the nonsolvent.
global polyvol
polyvol=266667; % Assume the polymer is only ? times larger than the nonsolvent small molecule.

% Open a file to record the spinodal curve.
% A: polymer-rich and B:polymer-poor
fid = fopen('aaa_binodal.dat','w');
fprintf(fid,'NonsolventA PolymerA SolventA NonsolventB PolymerB SolventB\n');

% error vector to double check if the solver gives correct answers at each iteration.
error_phi1A=[0]; error_phi2A=[0];

% Initialize the phi3B (the polymer) vector.
N1=200;N2=200;
phi3B_vect1=linspace(0.0000000002,0.00000001,N1);
for i=1:N2
    phi3B_vect1=[phi3B_vect1 0]
end
phi3B_vect2=linspace(0.000000001,0.05,N2);
for i=1:N1
    phi3B_vect2=[0 phi3B_vect2];
end
phi3B_vect=phi3B_vect1+phi3B_vect2;

x_guess=[0.98 0.01 0.8]; % initial guess of phi2B, phi2A, phi3A
options = optimset('TolFun',1e-6, 'Display','off', 'LargeScale','off');

%% 2. Calculate the binodal
phians=zeros(length(phi3B_vect),6);
for k=1:length(phi3B_vect)
    global phi3B
    phi3B=phi3B_vect(k);
    [x,fval] = fsolve(@binodal_calc,x_guess);
    phi2B=x(1); phi2A=x(2); phi3A=x(3);
    phi1B=1-phi3B-phi2B; phi1A=1-phi3A-phi2A;

    phians(k,1)=phi1A; phians(k,2)=phi2A; phians(k,3)=phi3A;
    phians(k,4)=phi1B; phians(k,5)=phi2B; phians(k,6)=phi3B;
end

```





## Appendix III: Matlab Codes for Mass Transfer Paths

```

function iflag_main = diffusion_stiffness(N);
clear all; clc; close all;
iflag_main = 0; tic
fid = fopen('PS_L10RH50_g13e22_g23e49.txt','w');
% generate 1-D grid
N=40; x = linspace(0,1,N); dx = x(2) - x(1); nx = length(x);
% set vector of times at which to print answer
t_end = 0.0002; t_space = t_end; t_vect=[0:t_space:t_end]; Cons.dt=t_vect(end)-t_vect(end-1);
mins=1/60; t_tot=ceil(1/t_end*60*mins);
%%%%Cons.dt=t_space;
% constant
Cons.lo1=1; Cons.lo2=0.94; Cons.lo3=1.05; % input density unit: g/cm^3
Cons.w10=10^-20; Cons.w20=0.7; Cons.w30=1-Cons.w10-Cons.w20; % input weight fraction
Cons.phi_10=Cons.w10/Cons.lo1/(Cons.w10/Cons.lo1+Cons.w20/Cons.lo2+Cons.w30/Cons.lo3);
Cons.phi_20=Cons.w20/Cons.lo2/(Cons.w10/Cons.lo1+Cons.w20/Cons.lo2+Cons.w30/Cons.lo3);
Cons.phi_30=1-Cons.phi_10-Cons.phi_20; % calculated volume fraction
Cons.L_0=0.0005; % initial thickness of thin film, unit:cm (for PS, 10mum)
Cons.V1=1/Cons.lo1;Cons.V2=1/Cons.lo2; Cons.V3=1/Cons.lo3; % partial specific volume, unit: cm^3/g
Cons.R=8.314*10^7; % unit: erg/mol/K
Cons.T=300; % temperature, unit: K
Cons.pmv1=18.0; Cons.pmv2=77.4; Cons.pmv3=266667; % pure molar volume, unit: cm^3/mole
Cons.M1=18.0; Cons.M2=73.09; Cons.g23=0.497; Cons.g13=2.2; Cons.NA=6.022*10^23;
% constant from Table II
Cons.V2sta=0.926; Cons.V3sta=0.850; % unit: cm^3/g
Cons.mw=0.47;
Cons.D20=8.48*10^-4; % unit: cm^2/s
Cons.K22_div_gamma=9.76*10^-4; % unit: cm^3/(g K)
Cons.K32_min_Tg2=-43.8; % unit: K % K32 or K22
Cons.K23_div_gamma=5.82*10^-4; % unit: cm^3/(g K)
Cons.K33=111; Cons.Tg3=111-(-327); % unit: K % K33 or K23
Cons.D12_1=1.12*10^-5; % unit: cm^2/s
Cons.friccoef12=Cons.pmv1*Cons.R*Cons.T/Cons.NA^2/Cons.D12_1;
% constant from Table III
Cons.D1g=0.267; Cons.D2g=0.023; % unit: cm^2/s
Cons.mug=1.85*10^-4; % unit: g/cm/s (Pa*s)
Cons.lo_g=1.18*10^-3; % unit: g/cm^3
Cons.tau1=0.413; Cons.tau2=-1.65; % unit: N/A
Cons.Lc=Cons.L_0; % unit: cm
Cons.P10=0.0313; Cons.P20=4.97*10^-3; Cons.Pt=1; % unit: atm
Cons.V1g=1358; Cons.V2g=335; % unit: cm^3/g
Cons.Sc_1=Cons.mug/Cons.lo_g/Cons.D1g; Cons.Sc_2=Cons.mug/Cons.lo_g/Cons.D2g;
L_pre=Cons.L_0;

% initial condition
phi_1 = ones(1,nx)*Cons.phi_10; phi_2 = ones(1,nx)*Cons.phi_20; phi_3=1-phi_1-phi_2;
phi_10 = phi_1; phi_20 = phi_2; phi_300=1-phi_10-phi_20;
phi0=[phi_1 phi_2];

% First simulate using ode15s solver with BDF method
%OptionsODE = odeset('BDF','on');
B=[N; dx; mins];fprintf(fid,'N dx mins\n'); fprintf(fid,'%12.8f%12.8f%12.8f\n',B);fprintf(fid,'phi1 phi2 phi3\n');

for k=1:t_tot
    time_sec=k/t_tot*mins*60
    [t,phi] = ode45(@diff_calc_f,t_vect,phi0,[],N,Cons,L_pre);
    t_cal=t;
    for i=1:N
        phi_1(1,i)=phi(end,i);
        phi_2(1,i)=phi(end,i+N);
        phi_3(1,i)=1-phi(end,i)-phi(end,i+N);
    end
    if rem(k,0.2*mins/Cons.dt)==0
        A=[phi_1; phi_2; phi_3];
        fprintf(fid,'%12.8f\t %12.8f\t %12.8f\n',A);
    end
    L_pre=(Cons.L_0^2*Cons.phi_30/2/(sum(((phi_3(1,1:end-1)+phi_3(1,2:end))/2).*((x(1,1:end-1)+x(1,2:end))/2))*dx))^0.5

```

```

phi0(1,:)=phi(end,:);
phi1=phi_1(end), phi2=phi_2(end), phi3=phi_3(end),
%drawnow;
end
fclose(fid);

plot(x,phi_20,'rx',x, phi_10,'rx',x, phi_300,'rx'); hold on;
plot(x,phi_2,'b',x, phi_1,'g', x, phi_3,'y');

%phi_1(end,:), phi_2(end,:), phi_3(end,:),

iflag_main = 1; toc
return;

%-----
function f = diff_calc_f(t,phi,N,Cons,L_pre);
% generate 1-D grid
t; x = linspace(0,1,N); dx = x(2) - x(1); phi_3=zeros(N,1);
for i=1:N
    phi_1(i,1)=phi(i,1);
    phi_2(i,1)=phi(i+N,1);
end
phi_3(:)=1-phi_1(:)-phi_2(:);
summation=0;
for i=1:N-1
    summation=summation+2*(phi_3(i)+phi_3(i+1))/2*(x(i)+x(i+1))/2;
end
%L=(Cons.L_0^2*Cons.phi_30/2/(sum((phi_3(1:end-1)+phi_3(2:end))./2)*((x(1:end-1)+x(2:end))./2)*dx))^0.5
L=(Cons.L_0^2*Cons.phi_30/(summation*dx))^0.5;
% assign space
u1=zeros(N,1);u2=zeros(N,1);g12=zeros(N,1);
dChemPo_1=zeros(N,1);dChemPo_2=zeros(N,1);dChemPo_3=zeros(N,1);
dChemPo_1_dphi_1=zeros(N,1);dChemPo_1_dphi_2=zeros(N,1);dChemPo_2_dphi_1=zeros(N,1);dChemPo_2_dphi_2=zeros(N,1);
);
w1=zeros(N,1);w2=zeros(N,1);w3=zeros(N,1);w_tot=zeros(N,1);
D2sta=zeros(N,1);phi_2_new=zeros(N,1);D2=zeros(N,1);
fricoef23=zeros(N,1);fricoef13=zeros(N,1);E12=zeros(N,1);E22=zeros(N,1);E21=zeros(N,1);E11=zeros(N,1);E0=zeros(N,1);D
T1=zeros(N,1);DT2=zeros(N,1);
D11=zeros(N,1);D12=zeros(N,1);D22=zeros(N,1);a1=zeros(N,1);a2=zeros(N,1);lo_1g_i=zeros(N,1);lo_2g_i=zeros(N,1);
y_1g_i=zeros(N,1);y_2g_i=zeros(N,1);
Gr_1=zeros(N,1);Gr_2=zeros(N,1);Gr=zeros(N,1);y_g_i=zeros(N,1);y_air_lm=zeros(N,1);k1=zeros(N,1);k2=zeros(N,1);f=zeros(
N,1);

% variables depend on phi
u1(:)=phi_1(:)/(phi_1(:)+phi_2(:)); u2(:)=phi_2(:)/(phi_1(:)+phi_2(:));
g12(:)=0.5+0.04*u2(:)+0.8*u2(:).^2-1.2*u2(:).^3+0.8*u2(:).^4;
dChemPo_1(:)=Cons.R*Cons.T*(log(phi_1(:))+1-phi_1(:)-Cons.pmv1/Cons.pmv2*phi_2(:)-
Cons.pmv1/Cons.pmv3*phi_3(:)+(phi_2(:)*g12(:)+phi_3(:)*Cons.g13)*(phi_2(:)+phi_3(:))...
-Cons.pmv1/Cons.pmv2*phi_2(:)*phi_3(:)*Cons.g23-u1(:)*u2(:)*phi_2(:)*(0.04+2*0.8*u2(:)-
1.2*3*u2(:).^2+0.8*4*u2(:).^3));
dChemPo_2(:)=Cons.R*Cons.T*(log(phi_2(:))+1-phi_2(:)-Cons.pmv2/Cons.pmv1*phi_1(:)-
Cons.pmv2/Cons.pmv3*phi_3(:)+(Cons.pmv2/Cons.pmv1*phi_1(:)*g12(:)+phi_3(:)*Cons.g23)*(phi_1(:)+phi_3(:))...
-Cons.pmv2/Cons.pmv1*phi_1(:)*phi_3(:)*Cons.g13+Cons.pmv2/Cons.pmv1*u1(:)*u2(:)*phi_1(:)*(0.04+2*0.8*u2(:)-
1.2*3*u2(:).^2+0.8*4*u2(:).^3));
dChemPo_3(:)=Cons.R*Cons.T*(log(phi_3(:))+1-phi_3(:)-Cons.pmv3/Cons.pmv1*phi_1(:)-
Cons.pmv3/Cons.pmv2*phi_2(:)+(Cons.pmv3/Cons.pmv1*phi_1(:)*Cons.g13+Cons.pmv3/Cons.pmv2*phi_2(:)*Cons.g23)*(ph
i_1(:)+phi_2(:))...
-Cons.pmv3/Cons.pmv1*phi_1(:)*phi_2(:)*g12(:));

dChemPo_1_dphi_1(:)=Cons.R*Cons.T*(1/phi_1(:)-1+Cons.pmv1/Cons.pmv3+phi_2(:)*(Cons.pmv1/Cons.pmv2*Cons.g23-
g12(:)-(phi_2(:)+2*phi_3(:))*Cons.g13...
+u1(:)-u2(:))*u2(:).^2*(0.04+2*0.8*u2(:)-1.2*3*u2(:).^2+0.8*4*u2(:).^3)...
+u1(:)*u2(:).^3*(2*0.8-1.2*3*2*u2(:)+0.8*4*3*u2(:).^2));
dChemPo_1_dphi_2(:)=Cons.R*Cons.T*(-Cons.pmv1/Cons.pmv2+Cons.pmv1/Cons.pmv3+(phi_2(:)+phi_3(:))*(g12(:)-
Cons.g13)+Cons.pmv1/Cons.pmv2*(phi_2(:)-phi_3(:))*Cons.g23...
+u1(:)*u2(:)*(u2(:)-u1(:)-1)*(0.04+2*0.8*u2(:)-1.2*3*u2(:).^2+0.8*4*u2(:).^3)...
-u1(:).^2*u2(:).^2*(2*0.8-1.2*3*2*u2(:)+0.8*4*3*u2(:).^2));

```

```

dChemPo_2_dphi_1(:)=Cons.R*Cons.T*(-
Cons.pmv2/Cons.pmv1+Cons.pmv2/Cons.pmv3+(phi_1(:)+phi_3(:))*(Cons.pmv2/Cons.pmv1*g12(:)-
Cons.g23)+Cons.pmv2/Cons.pmv1*(phi_1(:)-phi_3(:))*Cons.g13...
+Cons.pmv2/Cons.pmv1*u1(:).^2*(1+u2(:)-u1(:))*(0.04+2*0.8*u2(:)-1.2*3*u2(:).^2+0.8*4*u2(:).^3)...
-Cons.pmv2/Cons.pmv1*u1(:).^2*u2(:).^2*(2*0.8-1.2*3*2*u2(:)+0.8*4*3*u2(:).^2));
dChemPo_2_dphi_2(:)=Cons.R*Cons.T*(1./phi_2(:)-1+Cons.pmv2/Cons.pmv3+Cons.pmv2/Cons.pmv1*phi_1(:)*(Cons.g13-
g12(:)-(phi_1(:)+2*phi_3(:))*Cons.g23...
+Cons.pmv2/Cons.pmv1*u1(:).^2*(u1(:)-u2(:))*(0.04+2*0.8*u2(:)-1.2*3*u2(:).^2+0.8*4*u2(:).^3)...
+Cons.pmv2/Cons.pmv1*u1(:).^3*u2(:)*(2*0.8-1.2*3*2*u2(:)+0.8*4*3*u2(:).^2));
w_tot(:)=Cons.lo1*phi_1(:)+Cons.lo2*phi_2(:)+Cons.lo3*phi_3(:);
w1(:)=Cons.lo1*phi_1(:)/w_tot(:); w2(:)=Cons.lo2*phi_2(:)/w_tot(:); w3(:)=1-w1(:)-w2(:);

D2sta(:)=Cons.D20*exp(-
(w2(:)*Cons.V2sta+w3(:)*Cons.mw*Cons.V3sta)/(w2(:)*Cons.K22_div_gamma*(Cons.K32_min_Tg2+Cons.T)+w3(:)*Cons.K23
_div_gamma*(Cons.K33+Cons.T-Cons.Tg3)));
%if phi_2(:)>0.8146
% phi_2_new(:)=0.8146;
%else phi_2_new(:)=phi_2(:);
%end
D2(:)=D2sta(:).*(1-phi_2(:)).^2.*(1-2*Cons.g23*phi_2(:));

fricoef23(:)=Cons.pmv3*Cons.R*Cons.T./D2sta(:)/phi_3(:)/Cons.NA^2;
fricoef13(:)=0.5*(Cons.pmv1/Cons.pmv2)*fricoef23(:);

DT1(:)=Cons.R*Cons.T/Cons.NA^2./(phi_2(:)*Cons.fricoeff12/Cons.pmv2+phi_3(:)*fricoef13(:)/Cons.pmv3);
DT2(:)=Cons.R*Cons.T/Cons.NA^2./(phi_1(:)*Cons.fricoeff12/Cons.pmv1+phi_3(:)*fricoef23(:)/Cons.pmv3);
E12(:)=(1-phi_1(:))*Cons.fricoeff12/Cons.M2./phi_3(:)-(Cons.R*Cons.T*Cons.V2/Cons.NA^2)/DT1(:)/phi_3(:);
E22(:)=Cons.V2*phi_1(:)*Cons.fricoeff12/Cons.pmv1./phi_3(:)-(Cons.R*Cons.T*Cons.V2)*(1-
phi_1(:))/(Cons.NA^2)/DT2(:)/phi_2(:)/phi_3(:);
E21(:)=(1-phi_2(:))*Cons.fricoeff12/Cons.M1./phi_3(:)-(Cons.R*Cons.T*Cons.V1/Cons.NA^2)/DT2(:)/phi_3(:);
E11(:)=Cons.V1*phi_2(:)*Cons.fricoeff12/Cons.pmv2./phi_3(:)-(Cons.R*Cons.T*Cons.V1)*(1-
phi_2(:))/(Cons.NA^2)/DT1(:)/phi_1(:)/phi_3(:);
E0(:)=
(Cons.fricoeff12^2/Cons.M1/Cons.M2)/phi_3(:)+(Cons.R^2*Cons.T^2*Cons.V1*Cons.V2/Cons.NA^4)/DT1(:)/DT2(:)/phi_1(
)/phi_2(:)/phi_3(:);
D11(:)=-Cons.V1/Cons.NA^2./E0(:)*(E22(:)*dChemPo_1_dphi_1(:)-E12(:)*dChemPo_2_dphi_1(:));
D12(:)=-Cons.V2/Cons.NA^2./E0(:)*(E22(:)*dChemPo_1_dphi_2(:)-E12(:)*dChemPo_2_dphi_2(:));
D22(:)=-Cons.V2/Cons.NA^2./E0(:)*(E11(:)*dChemPo_2_dphi_2(:)-E21(:)*dChemPo_1_dphi_2(:));

a1(:)=exp(dChemPo_1(:)/Cons.R/Cons.T); a2(:)=exp(dChemPo_2(:)/Cons.R/Cons.T);
lo_1g_inf=4.73*10^-6*5/2; lo_1g_i(:)=a1(:)*Cons.P10/Cons.V1g/Cons.Pt; %%% Change humidity here
lo_2g_inf=10^-20; lo_2g_i(:)=a2(:)*Cons.P20/Cons.V2g/Cons.Pt;
y_1g_inf=lo_1g_inf/Cons.M1/(Cons.lo_g/28.8); y_1g_i(:)=lo_1g_i(:)/Cons.M1/(Cons.lo_g/28.8);
y_2g_inf=lo_2g_inf/Cons.M2/(Cons.lo_g/28.8); y_2g_i(:)=lo_2g_i(:)/Cons.M2/(Cons.lo_g/28.8);

Gr_1(:)=(2*Cons.Lc)^3*Cons.lo_g^2*980*abs(Cons.tau1)*abs(y_1g_i(:)-y_1g_inf)/Cons.mug^2;
Gr_2(:)=(2*Cons.Lc)^3*Cons.lo_g^2*980*abs(Cons.tau2)*abs(y_2g_i(:)-y_2g_inf)/Cons.mug^2;
%Gr(:)=Gr_1(:)+Gr_2(:);
y_g_i(:)=1-y_1g_i(:)-y_2g_i(:); y_g_inf=1-y_1g_inf-y_2g_inf;
y_air_lm(:)=(y_g_i(:)-y_g_inf)/log(y_g_i(:)/y_g_inf);
k1(:)=0.53*(Gr_1(:)*Cons.Sc_1).^0.25./(2*Cons.Lc)/y_air_lm(:)*Cons.D1g;
k2(:)=0.53*(Gr_2(:)*Cons.Sc_2).^0.25./(2*Cons.Lc)/y_air_lm(:)*Cons.D2g;

% Begin of finite difference
f(1,1)=1/L^2*(D11(1)*(phi_1(2)-2*phi_1(1)+phi_1(2))/(dx^2)+D12(1)*Cons.V1/Cons.V2*(phi_2(2)-
2*phi_2(1)+phi_2(2))/(dx^2));
phi_1_tmp=phi_1(end-1)+(2*dx)*(-k1(end)*L*Cons.V1*(lo_1g_i(end)-lo_1g_inf)/D11(end)...
+k2(end)*L*Cons.V1*(lo_2g_i(end)-lo_2g_inf)*D12(end)/D11(end)/D2(end));
phi_2_tmp=phi_2(end-1)-k2(end)*L*Cons.V2*(lo_2g_i(end)-lo_2g_inf)*2*dx/D2(end);

for i=2:length(x)-1
f(i)=x(i)/L*(L-L_pre)/Cons.dt*(phi_1(i+1)-phi_1(i-1))/(2*dx)...
+1./L^2*(D11(i)*(phi_1(i+1)-2*phi_1(i)+phi_1(i-1))/(dx^2)+D12(i)*Cons.V1/Cons.V2*(phi_2(i+1)-2*phi_2(i)+phi_2(i-
1)))/(dx^2))...
+D11(i)/x(i)/L^2*(phi_1(i+1)-phi_1(i-1))/(2*dx)+D12(i)/x(i)/L^2*(phi_2(i+1)-phi_2(i-1))/(2*dx);
end

f(N,1)=x(N)/L*(L-L_pre)/Cons.dt*(phi_1_tmp-phi_1(N-1))/(2*dx)...

```

```

+1/L^2*(D11(N)*(phi_1_tmp-2*phi_1(N)+phi_1(N-1))/(dx^2)+D12(N)*Cons.V1/Cons.V2*(phi_2_tmp-
2*phi_2(N)+phi_2(N-1))/(dx^2))...
+D11(N)./x(N)./L^2.*(phi_1_tmp-phi_1(N-1))/(2*dx)+D12(N)./x(N)./L^2.*(phi_2_tmp-phi_2(N-1))/(2*dx);

```

```

f(N+1,1)=1/L^2*D2(1)*(phi_2(2)-2*phi_2(1)+phi_2(2))/(dx^2);

```

```

for i=2:length(x)-1
f(N+2:2*N-1)=x(i)/L*(L-L_pre)/Cons.dt*(phi_2(i+1)-phi_2(i-1))/(2*dx)+...
1/L^2*D2(i).*(phi_2(i+1)-2*phi_2(i)+phi_2(i-1))/(dx^2)...
+D2(i)./x(i)./L^2.*(phi_2(i+1)-phi_2(i-1))/(2*dx);
end

```

```

f(2*N,1)=x(N)/L*(L-L_pre)/Cons.dt*(phi_2_tmp-phi_2(N-1))/(2*dx)+...
1/L^2*D2(N)*(phi_2_tmp-2*phi_2(N)+phi_2(N-1))/(dx^2)...
+D2(N)./x(N)./L^2.*(phi_2_tmp-phi_2(N-1))/(2*dx);

```

```

return;

```

## Appendix IV: Matlab Codes for the Calculation of Orientation and Curvature Distribution of Nonwoven Fabrics Using Image Analysis

```

% orientation: Dimitrios Tzeranis, December 2007,
% curvature: J. van de Weijer, L.J. van Vliet, P.W. Verbeek, M. van Ginkel, 2001
% combined and modified by Chia-Ling, April 2011.

clc, close all, clear all

tic;
%% %% algorithm parameters
LPBlockSize = 1; sigma_g = 23; sigma_a = 23; pixsize=256;

% read image
RawFrame = imread('10fa-ran1-2-left.tif');
% RawFrame = rgb2gray(RawFrame); % if the image is X*X*3 unit 8.
subplot(3,3,1),imshow(RawFrame); title('Check origin image','FontSize',10)

RawFrame = imresize(RawFrame,[512,512]); RawFrame = RawFrame(:,:,);
RawFrame = imresize(RawFrame,[pixsize,pixsize]);
RawFrame = imadjust(RawFrame); RawFrame = double(RawFrame);

PhotonC = double(RawFrame)/double(max(max(RawFrame)));
PhotonC2 = reshape(PhotonC,1,pixsize^2);
subplot(3,3,2); imshow(PhotonC);
title('New image - PhotonC','FontSize',10)

%% %% ==> local orientation analysis
Hx = [3,0,-3;10,0,-10;3,0,-3]/32;
Ax = imfilter(RawFrame,Hx,'replicate'); Ay = imfilter(RawFrame,Hx,'replicate');
Axx = Ax.*Ax; Ayy = Ay.*Ay; Axy = Ax.*Ay;
Jxx = imfilter(Axx,fspecial('average',LPBlockSize),'replicate');
Jyy = imfilter(Ayy,fspecial('average',LPBlockSize),'replicate');
Jxy = imfilter(Axy,fspecial('average',LPBlockSize),'replicate');

c = sqrt((Jyy - Jxx).^2 + 4*Jxy.^2)/(Jxx + Jyy); % confidence function
c2 = reshape(c,1,pixsize^2); % value falls within 0 to 1
chist = hist(c2,linspace(0,1,20));
subplot(3,3,3),bar(linspace(0,1,20),chist); xlim([0,1]);
title('Cohesion (Goal->1)','FontSize',10)

%% %% -----
%% %% ==> Modified by IEEE PAMI 2001 in order to capture the local curvature

% initialize the filter
break_of_sigma = 3; filtersize = break_of_sigma*sigma_g;
% compute the Gaussian and first Gaussian derivatives at scale sigma_g for orientation
% compute the Gaussian and first Gaussian derivatives at scale sigma_g
[y x] = ndgrid(-filtersize:filtersize,-filtersize:filtersize);
Gg = 1/(2 * pi * sigma_g^2) * exp(-(x.^2 + y.^2)/(-2 * sigma_g * sigma_g));
Gg_x = 1/(sigma_g^2) * x * Gg; Gg_y = 1/(sigma_g^2) * y * Gg;

% Compute the (moment generating) filters at scale sigma_a
filtersize = break_of_sigma*sigma_a;
[y x] = ndgrid(-filtersize:filtersize,-filtersize:filtersize);
Ga = 1/(2 * pi * sigma_a^2) * exp(-(x.^2 + y.^2)/(-2 * sigma_a * sigma_a));
Ga_x = x * Ga; Ga_y = y * Ga;
Ga_xy = x * Ga_y; Ga_xx = x * Ga_x; Ga_yy = y * Ga_y;

% orientation_imation Estimation
Fx = imfilter(RawFrame, Gg_x,'replicate'); Fy = imfilter(RawFrame, Gg_y,'replicate');
Fxx = Fx.*Fx; Fxy = Fx.*Fy; Fyy = Fy.*Fy;

% theta values from J (gradient angle)
orientation_im = 1/2 * atan2(2 * imfilter(Fxy, Ga,'replicate'), imfilter((Fxx - Fyy),Ga,'replicate'));
orientation_im2 = reshape(orientation_im,1,pixsize^2);

```

```

% theta values from DT (gradient angle)
theta = atan2(2*[xy,-jyy+jxx ]/2); % I change the sign of jyy and jxx from DT, it means gradient now!!!
theta2 = reshape(theta,1,pixsize^2);

% magnitude of orientation vector
BandNum = 61;
mag = sqrt(double((2*[xy).^2) + double((jyy-jxx).^2)));
mag2 = reshape(mag,1,pixsize^2); MaxMag = max(mag2);
mag2 = mag2/MaxMag; % the value falls within 0 to 1
maghist = hist(mag2,linspace(1/BandNum/2,1-1/BandNum/2,BandNum));
subplot(3,3,4),bar(linspace(1/BandNum/2,1-1/BandNum/2,BandNum),maghist)
ylim([0, 2000]);
title('orientation vector magnitude','FontSize',10)

HsvImage = ones(pixsize,pixsize,3);
HsvImage(:,,1) = (theta + pi/2)/pi;
HsvImage(:,,3) = double(PhotonC)/double(max(max(PhotonC)))*mag/max(max(mag));
RgbImage = hsv2rgb(HsvImage);
subplot(3,3,5),imshow(RgbImage); title('theta by DT','FontSize',10)
HsvImage(:,,1) = (orientation_im + pi/2)/pi;
subplot(3,3,6),imshow(RgbImage); title('theta by J','FontSize',10)

Mask1 = PhotonC2>0.1; Mask2 = mag2>0.1;
Mask3 = PhotonC>0.1; Mask4 = mag>0.1;
theta2(~(Mask1&Mask2)) = [];
orientation_im2(~(Mask1&Mask2)) = [];
orientation_im = Mask3.*orientation_im; orientation_im = Mask4.*orientation_im;
thetahist = hist(theta2,linspace(-pi/2+pi/BandNum/2,pi/2-pi/BandNum/2,BandNum));
orientation_im_hist = hist(orientation_im2,linspace(-pi/2+pi/BandNum/2,pi/2-pi/BandNum/2,BandNum));
subplot(3,3,7),bar(linspace(-pi/2,pi/2,BandNum)/pi*180,thetahist);
title('theta by DT','FontSize',10)
subplot(3,3,8),bar(linspace(-pi/2,pi/2,BandNum)/pi*180,orientation_im_hist);
title('theta by J','FontSize',10)

%%*****Circle*****

% Curvature Estimation
CosPhi = cos(orientation_im);
SinPhi = sin(orientation_im);
% CosPhi = cos(theta);
% SinPhi = sin(theta);

% see equation 27
A = imfilter(Fxx, Ga_xx,'replicate') + 2*imfilter(Fxy, Ga_xy,'replicate') + imfilter(Fyy, Ga_yy,'replicate');
B = -(imfilter(Fxx, Ga_x,'replicate') + imfilter(Fxy, Ga_y,'replicate')).*CosPhi - (imfilter(Fxy, Ga_x,'replicate') + imfilter(Fyy, Ga_y,'replicate')).*SinPhi;
C = imfilter(Fxx, Ga,'replicate').*CosPhi.*CosPhi + 2*imfilter(Fxy, Ga,'replicate').*CosPhi.*SinPhi + imfilter(Fyy, Ga,'replicate').*SinPhi.*SinPhi;
D = ones(size(C))*2*sigma_a*sigma_a;
E = imfilter(Fyy, Ga_xx,'replicate') - 2*imfilter(Fxy, Ga_xy,'replicate') + imfilter(Fxx, Ga_yy,'replicate');
F = (imfilter(Fxy, Ga_y,'replicate') - imfilter(Fyy, Ga_x,'replicate')).*CosPhi + (imfilter(Fxy, Ga_x,'replicate') - imfilter(Fxx, Ga_y,'replicate')).*SinPhi;
G = imfilter(Fyy, Ga,'replicate').*CosPhi.*CosPhi - 2*imfilter(Fxy, Ga,'replicate').*CosPhi.*SinPhi + imfilter(Fxx, Ga,'replicate').*SinPhi.*SinPhi;

% Compute Curvature (eq.25) and Confidence (eq.28))

curvature_im = double(E - G.*D - sqrt(4 * F.*F.*D + power(-E + G.*D, 2)))...
./(2*F.*D);
curvature_im = abs(curvature_im);
curvature_im2 = reshape(curvature_im,1,pixsize^2);

curvature_im2(~(Mask1&Mask2)) = [];
curvature_im = Mask3.*curvature_im;
curvature_im = Mask4.*curvature_im;

```

```

avg_curvature=sum(curvature_im2)/length(curvature_im2),
stdev=std(curvature_im2(:)),
avg_radius=1/avg_curvature,

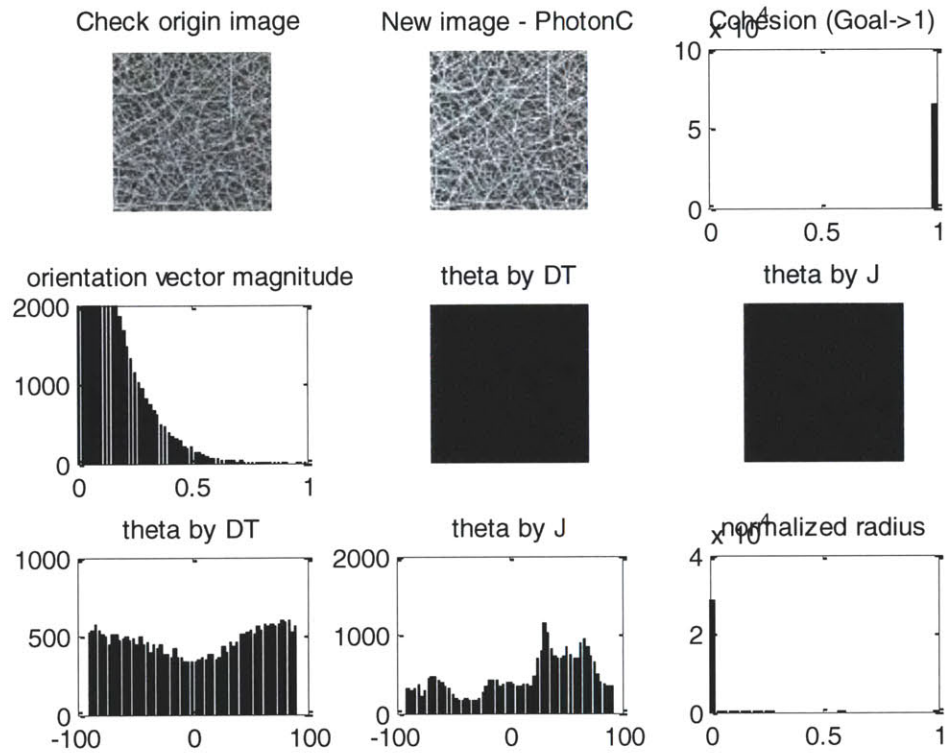
Radius=1./curvature_im2;

MaxRadius = max(Radius),
Radius = Radius/MaxRadius; % the value falls within 0 to 1
Radiushist = hist(Radius,linspace(0,1,20));
subplot(3,3,9),bar(linspace(0,1,20),Radiushist)
title('normalized radius',FontSize,10), xlim([0,1]);

toc;

```

## Results:



avg\_curvature = 0.0114

stdev = 0.0081

avg\_radius = 88.0662 (unit: pixel)

MaxRadius = 5.6739e+005

Elapsed time is 8.714549 seconds.



## Appendix V: Determination of Diffusion and Mass Transfer Coefficients

The diffusion coefficients,  $D_2$  [1-4],  $D_{11}$ , and  $D_{12}$  [5-6], were estimated based on the following equations and are functions of  $\varphi$ .

$$D_2^* = D_{20} e^{-E/RT} \exp\left(-\frac{w_2 V_2^* + w_3 \zeta V_3^*}{w_2 (K_{22}/\gamma)(K_{32} - T_{g2} + T) + w_3 (K_{23}/\gamma)(K_{33} - T_{g3} + T)}\right) \quad (I-1)$$

$$D_2 = D_2^* (1 - \varphi_2)^2 (1 - 2g_{23}\varphi_2) \quad (I-2)$$

$$D_{11} = -\frac{V_1}{N_A^2 E_0} \left( E_{22} \frac{\partial \mu_1}{\partial \varphi_1} - E_{12} \frac{\partial \mu_2}{\partial \varphi_1} \right) \quad (I-3)$$

$$D_{12} = -\frac{V_2}{N_A^2 E_0} \left( E_{22} \frac{\partial \mu_1}{\partial \varphi_2} - E_{12} \frac{\partial \mu_2}{\partial \varphi_2} \right) \quad (I-4)$$

$$E_{12} = \frac{(1 - \varphi_1)\zeta_{12}}{M_2 \varphi_3} - \frac{RTV_2}{N_A^2 D_{T1} \varphi_3} \quad (I-5)$$

$$E_{22} = \frac{V_2 \varphi_1 \zeta_{12}}{v_1 \varphi_3} - \frac{RTV_2(1 - \varphi_1)}{N_A^2 D_{T2} \varphi_2 \varphi_3} \quad (I-6)$$

$$E_0 = -\frac{\zeta_{12}^2}{M_1 M_2 \varphi_3} + \frac{R^2 T^2 V_1 V_2}{N_A^4 D_{T1} D_{T2} \varphi_1 \varphi_2 \varphi_3} \quad (I-7)$$

$$D_{T1} = \frac{RT}{N_A^2 (\varphi_2 \zeta_{12}/v_2 + \varphi_3 \zeta_{13}/v_3)} \quad (I-8)$$

$$D_{T2} = \frac{RT}{N_A^2 (\varphi_1 \zeta_{12}/v_1 + \varphi_3 \zeta_{23}/v_3)} \quad (I-9)$$

$$\zeta_{12} = \frac{v_1 RT}{N_A^2 D^{12}(\varphi_1 = 1)} \quad (I-10)$$

$$\zeta_{23} = \frac{v_3 RT}{N_A^2 D_2^* \varphi_3} \quad (I-11)$$

$$\zeta_{13} = 0.5(v_1/v_2)\zeta_{23} \quad (I-12)$$

where  $D_2^*$  is the self-diffusion coefficient of the solvent.  $D_{20}$  is the pre-exponential factor of the solvent [4].  $E$  is the energy per mole for a molecule to overcome attractive forces from its neighbors, and was assumed to be zero here [4].  $V_i^*$  is the specific critical hole free volume required for a jump for component I [4,7].  $w_i$  is the

weight fraction of component  $i$ .  $\xi$  is the ratio of molar volumes for the solvent and polymer jumping units [4].  $K_{22}$ ,  $K_{32}$ ,  $K_{23}$ ,  $K_{33}$  are free-volume parameters [4].  $\gamma$  is the overlap factor [4].  $T_{gi}$  is the glass transition temperature of component  $i$  [4].  $N_A$  is Avogadro's number.  $M_i$  is the molecular weight of component  $i$ .  $\zeta_{12}$ ,  $\zeta_{23}$ , and  $\zeta_{13}$  are the friction parameters [8].  $D^{12}$  is the mutual diffusion coefficient in solvent-nonsolvent system [6].

The gas-side mass transfer coefficient  $k_i$  for single horizontal cylinders under free convection is [9]:

$$k_i = \frac{0.53(Gr_i Sc_i)^{0.25} D_{ig}}{D_c y_{air}^{lm}} \quad (I-13)$$

$$Gr_i = \frac{D_c^3 \rho_g^2 g}{\mu_g^2} |\tau_i (y_{ig}^i - y_{ig}^{inf})| \quad (I-14)$$

$$Sc_i = \frac{\mu_g}{\rho_g D_{ig}} \quad (I-15)$$

where  $D_c$  is the characteristic diameter of the fiber.  $y_{air}^{lm}$  is the logarithm mean mole fraction difference of air.  $D_{ig}$  [10-11],  $\rho_g$  [12], and  $\mu_g$  [12] are the mutual diffusion coefficient of component  $i$  in the gas phase, total mass density of the gas phase, and viscosity of the gas, respectively.  $y_{ig}$  are the mole fraction of component  $i$ .  $g$  is the gravity constant.  $\tau_i$  is calculated from  $-1/\rho_g (\partial\rho_g / \partial y_{ig})_{P,T}$ .

$\rho_{ig}^i$  was calculated by:

$$\rho_{ig}^i = a_i P_i^0 / (V_{ig} P_t) \quad (I-16)$$

$$a_i = \exp(\Delta\mu_i / RT) \quad (I-17)$$

where  $a_i$  is the activity of component  $i$ .  $P_t$  and  $P_i^0$  [10,13] are the total pressure and the saturated vapor pressure for pure component  $i$ .  $V_{ig}$  is the partial specific volume of component  $i$  in the gas phase. The detailed derivation for mass transfer equations is presented in reference [5,14-15].

## References

- [1] Vrentas JS, Duda JL. "Molecular-diffusion in polymer-solutions", *AIChE J.* 1979; 25: 1-24.
- [2] Vrentas JS, Duda JL, Ling HC. "Self-diffusion in polymer-solvent-solvent systems", *J. Polym. Sci. Polym. Phys. Ed.* 1984; 22: 459-469.
- [3] Duda JL, Ni YC, Vrentas JS. "Equation relating self-diffusion and mutual diffusion-coefficients in polymer-solvent systems", *Macromolecules* 1979; 12: 459-462.
- [4] Zielinski JM, Duda JL. "Predicting polymer solvent diffusion-coefficients using free-volume theory", *AIChE J.* 1992; 38: 405-415.
- [5] Tsay CS, McHugh AJ. "Mass-transfer modeling of asymmetric membrane formation by phase inversion", *Journal of Polymer Science: Part B: Polymer Physics* 1990; 28: 1327-1365.
- [6] Wilke CR, Chang P. "Correlation of diffusion coefficients in dilute solutions", *AIChE J.* 1955; 1: 264-270.
- [7] Sugden, S. "Molecular volumes at absolute zero: II. Zero volumes and chemical composition", *J Chem Soc* 1927: 1786-1798.
- [8] Vrentas JS, Duda JL, Ling HC. "Enhancement of impurity removal from polymer-films", *J Appl Polym Sci* 1985; 30: 4499-4516.
- [9] McAdams WH. *Heat Transmission*, 3rd ed.; McGraw-Hill: New York, 1954: 177.
- [10] The Society of Chemical Engineers of Japan Ed. *Handbook of Chemical Engineering (in Japanese)*, 5th ed.; Maruzen: Tokyo, 1988.
- [11] Bird RB, Stewart WE, Lightfoot EN. *Transport Phenomena*, John Wiley & Sons: New York, 1960.
- [12] Lide DR. *Handbook of Chemistry and Physics*, 71th ed.; CRC press: Boca Raton, FL, 1990.
- [13] The Chemical Society of Japan Ed., *Handbook of Chemistry (in Japanese)*, 4th ed.; Maruzen: Tokyo, 1993.
- [14] Matsuyama H, Teramoto M, Nakatani R, Maki T. "Membrane formation via phase separation induced by penetration of nonsolvent from vapor phase. I. Phase diagram and mass transfer process", *J. Appl. Polym. Sci.* 1999; 74: 159-170.

- [15] Yip Y, McHugh AJ. "Modeling and simulation of nonsolvent vapor-induced phase separation", *J. Membrane Sci.* 2006, 271, 163-176.